THERMAL STRESS ANALYSIS OF LCA-BASED SOLID OXIDE FUEL CELLS

A Thesis
Presented to
The Academic Faculty

By

Jason LeMasters

In Partial Fulfillment
Of the Requirements for the Degree
Master of Science in Mechanical Engineering

Georgia Institute of Technology
April 2004

THERMAL STRESS ANALYSIS OF LCA-BASED SOLID OXIDE FUEL CELLS

Approved by:

_____
Dr. David L. McDowell, Chairman

_____
Dr. Joe K. Cochran, Jr.

_____
Dr. Richard W. Neu

Date Approved__April 1, 2004_____

ACKNOWLEDGEMENTS

My time at Georgia Tech has been short, filled with classes, projects, research and writing. Much of this research involved lone hours of programming and modeling, but I would not have completed my work without the guidance of my advisor, Dr. McDowell, and the support of my research group.

Many aspects of this work were related to previous and ongoing research by Ben Dempsey. I would thank him and Scott Eisele for their contributions in areas both peripheral and integral to this work.

TABLE OF CONTENTS

ACKNOWLEDGEMENTS iii

TABLE OF CONTENTS iv

LIST OF TABLES vi

LIST OF FIGURES vii

CHAPTER I. BACKGROUND 1
I.1. The basics of solid oxide fuel cells 1
I.2. Current monolithic SOFC technology 2
I.3. Thermo-mechanical stress during the operation of hybrid LCA SOFCs 7
I.3.1. Fabrication 9
I.3.2. Stresses occurring during operation 11
I.4. Failure in the hybrid SOFC 12
I.4.1. Thermally-induced stress within a homogeneous material 12
I.4.2. Thermal Shock 13
I.4.3. Thermal stresses arising from the CTE mismatch between components 13
I.5. Failure criterion 14
I.6. SOFC thermal-stress analysis on planar models 15
I.7. Temperature field calculation 17
I.8. Motivation 18

CHAPTER II. FINITE DIFFERENCE-BASED THERMAL ANALYSIS OF SOFC'S 19
II.1. Introduction 19
II.2. Model setup and boundary conditions 21
II.3. Discretization of geometry in the finite difference code 22
II.4. Governing Equations 27
II.4.1. Steady state problem 27
II.4.2. Transient problem 28
II.5. Approximation of material properties 29
II.5.1. Fluid properties and curve-fitting 29
II.5.2. Metal and Ceramic Properties 31
II.5.3. Heat generation approximations 33
II.6. Solution Techniques 39
II.6.1. Matrix form of governing equations 39
II.6.2. Programming flowchart 40
II.6.3. Iterative technique 43
II.7. Convergence of solution techniques 43
II.7.1. Convergence of the iterative method used in the solver 43
II.7.2. Convergence of the heat generation loop 47

II.7.2.1. Convergence of heat generation loop assuming constant current 47
II.7.2.2. Convergence of heat generation loop assuming constant operating voltage 49
II.7.3. Convergence of the transient solution to the steady state 50
II.8. Parameterization capability of the finite difference code in modeling hybrid SOFCs 54
II.8.1. Acceptable solid geometries 54
II.8.2. Acceptable fluid conditions 56
II.8.3. Considerations in parameterization of hybrid SOFC design 56
II.9. Validation of finite difference results 59
II.9.1. Validation of solution techniques 59
II.9.2. Validation of finite difference formulation 61
II.9.2.1. No generation case 62

CHAPTER III. THERMAL STRESS ANALYSIS 70
III.1. Isothermal stress solutions to model residual stress 71
III.1.1. Purpose of model 71
III.1.2. Simple laminate structures 72
III.1.3. Isothermal honeycomb model 76
III.1.3.1. Modeling using reduced-integration elements 76
III.1.3.2. Modeling using full integration elements 79
III.2. Stress analysis during operation 89
III.2.1. Using ABAQUS to distribute FD solution 89
III.2.2. Stress analysis according to results of ABAQUS thermal analysis 94
III.2.2.1. Boundary conditions 94
III.2.2.2. Material properties 95
III.2.2.3. Step definitions in transient analysis 96
III.3. Using the thermal-stress analysis tools to analyze performance and integrity 97
III.3.1. Model Setup 97
III.3.2. Finite difference transient temperature field 97
III.3.3. Contour plots of stresses 100
III.3.4. Line graphs of stresses 101
III.4. Example with no CTE mismatch 103
III.5. Thermal shock considerations 104

CHAPTER IV. CONCLUSIONS 107
IV.1. Summary of model 107
IV.2. Related research 109
IV.3. Future consideration of heat transfer by radiation 109
IV.4. Parametric modeling of the hybrid SOFC 112

REFERENCES 113

LIST OF TABLES

Table I.1: Modulus of rupture data for 8% mol YSZ (Du et al., 2003) 15

Table II.1: YSZ property data. 31

Table II.2: Fe39Ni8Cr property data. 32

Table II.3: Inputs used for test cases performed by FLUENT and finite difference. 66

Table II.4: FLUENT results for comparison with finite difference approximations. 67

Table II.5: An energy balance approach for comparing FLUENT and finite difference heat generation with the convective heat dissipation signified by a change in fluid temperatures. 68

Table II.6: Variations in inputs to test the influence of flow rates on results. 69

Table II.7: An energy balance approach for comparing FLUENT and finite difference heat generation with the convective heat dissipation signified by a change in fluid temperatures. 69

Table III.1: Stress-plastic strain data for $Fe_{39}Ni_8Cr$ does not include elastic strain. 96

Table III.2: The resistance to thermal shock was calculated by Equation 8 for YSZ and compared to reported formula results for a number of ceramics in Lee and Rainforth (1994). 105

LIST OF FIGURES

Figure I.1: In the electrochemical reaction of SOFCs, oxygen and hydrogen react to produce water and electricity (Singhal, 2000). 2

Figure I.2: Monolithic SOFC design (Minh and Takahashi, 1995) 4

Figure I.3: Co-extrusion fabrication process beginning with oxide powders and ending with the finished linear cellular alloy (LCA). 5

Figure I.4: The hybrid LCA SOFC has a honeycomb structure(top). The thin anode and cathode are applied to the inside of the channels after the honeycomb is fabricated (bottom). The electrode thickness is exaggerated for clarity. 6

Figure I.5: The hybrid SOFC is subjected to a variety of stress from manufacturing through steady state operation. 8

Figure I.6: Calculated cooling residual stress due to thermal expansion mismatch between various Zirconium oxides and Alumina (Cai et al., 1997). 10

Figure I.7: Gradual flow increase of a cool jet stream, directed at the center of a 50 mm square specimen, resulted in fracture due to the induced temperature gradient (Hagos and Travis, 2003)..... 12

Figure I.8: Planar SOFC design showing PEN structure, interconnect and manifolding technique (Yakabe, 2001). 15

Figure II.1: The hybrid SOFC design has alternating layers of metal and ceramic components acting as the interconnect and electrolyte respectively, and air and fuel are in counterflow. 21

Figure II.2: Heat generation in the FD code is applied directly to the indicated regions within the electrolyte..... 21

Figure II.3: Discretization of honeycomb structure into finite elements. 23

Figure II.4: Mesh geometries resulting from discretization of the honeycomb structure. 23

Figure II.5: The local numbering scheme for the finite difference elements is comprised of a center node (#6) surrounded by eight in-plane and two out-of-plane nodes. 24

Figure II.6: The global coordinate numbering scheme (shown for a 4x4 cell geometry) begins with node 1 in the upper left corner and numbers sequentially in the positive x, y and z directions..... 26

Figure II.7: Fluid Convection Coefficients for Air and Hydrogen. 30

Figure II.8: The heat generation varies with temperature, as shown for a 4 x 4 array of square cells, 10 cm long with inlet fluid temperatures of 475K and an air flow rate of 7.24e-4 kg/s. 37

Figure II.9: The same case as Figure II.8, when solved by the finite difference code, shows the transient variation in heat generation. 38

Figure II.10: The input temperatures for a prior time step initiate a series of loops to converge on the temperature solutions for the next time step. The looping procedure is based on prior work by Dempsey (Dempsey, 2002). 42

Figure II.11: The SOR method is shown to diverge for the counter-flow steady state temperature solution of a 4x4 unit cell, 0.86x0.86x10cm with 7.24e-4kg/s air flow (m=94). 45

Figure II.12: Gauss Seidel iteration of SOFC shown to converge for the counter-flow steady state temperature solution of a 4x4 unit cell, 0.86x0.86x10cm with 7.24e-4kg/s air flow (m=94). 46

Figure II.13: Convergence of the heat generation loop for constant current. Cases with flows of 7.24e-4 (bottom) and 7.24e-6 (top) are shown for a 4x4 SOFC, with dimensions 0.86x0.86x10cm, inlet fluid temperatures of 475K and initial wall temperature guess of 1000K. A low temperature cutoff for the fuel cell reaction was not applied in these examples (making possible heat generation below 900K)..... 48

Figure II.14: Convergence of the heat generation loop for variable current assuming constant operating voltage. The Cases shown has inlet air flow of 7.24e-5, with dimensions 0.86x0.86x10cm, inlet air temperature of 980K, inlet fuel temperature of 475K, and initial wall temperature guess of 1000K. A low temperature cutoff of 910K was used to simulate the onset of the chemical reaction..... 49

Figure II.15: Using ω=0.4 and the same setup as Figure II.14, different initial guesses were tested to insure convergence. 50

Figure II.16: An example of the effect of time step size on average fuel cell temperature for a 4x4 (0.86cm x 0.86cm x 3cm) YSZ-$Fe_{39}Ni_8Cr$ fuel cell with 300K inlet fuel and air, 2e-7kg/sec air flow and 2.784e-8kg/sec fuel flow. The time steps were linear above 10 sec and exponentially weighted below (constant current is used). 51

Figure II.17: For the worst case scenario of Figure II-12, the adjusting time steps converged better and with less iteration when brought to steady state. Both converged on the steady state solution..... 53

Figure II.18: The FD code can solve for the transient temperature distribution in a large range of rectangular celled geometries. Not shown is the ability to model unit cells stacked vertically. 55

Figure II.19: The length of the fuel cell was varied from 3cm to 10cm. As expected, the steady state temperature increases in the electrolyte with longer fuel cells, but also, the gradient becomes more severe from front to back. 57

Figure II.20: Transient results show the 3cm SOFC heats up much faster than the longer fuel cells by convection, but the heat generation starting at 25 seconds is less. Eventually, the longer fuel cells become hotter. 58

Figure II.21: The FD code has similar results for a range of element depths. The model displayed is for a steady state, 4x4 (.86x.86cm), 10cm long, 7.24e-4kg/s air, with fuel/air inlet temperature of 475K. Note that the convergence of the selected nodes was indicative of entire structure. 61

Figure II.22: A 10cm long heat exchanger problem with no heat generation, 1000K inlet fuel at low flow rate and 300K inlet air at high flow rate was evaluated with a) FLUENT (fluid and wall temperatures shown), b) FLUENT (only wall temperatures), and c) the FD code. 64

Figure II.23: a) Finite difference and b) FLUENT temperature profiles for Case 10 at steady state. 68

Figure III.1: Stress due to CTE mismatch in a laminate of YSZ and $Fe_{39}Ni_8Cr$ after temperature is reduced from 1273K to RT modeled a) elastically and b) plasticallly. Each laminate component is 0.2 cm x 0.012 cm x 3 cm. 73

Figure III.2: Stress due to CTE mismatch in a bilaminate of YSZ and $Fe_{39}Ni_8Cr$ after temperature is reduced from 1273K to RT, modeled plasticallly. The ceramic component is 0.2 cm x 0.012 cm x .3 cm while the each metal component is half as tall (0.1 cm x 0.012 cm x .3 cm). 74

Figure III.3: Shear (left) and peeling (right) stresses for a metal/ceramic laminate, normalized to the yield stress of the plastic material (Lambropoulos and Wan, 1989). 75

Figure III.4: a) Elastic and b) plastic models of von Mises stress for a 4x4 unit cell, YSZ-Inconel hybrid, isothermal cool-down from 1000°C to RT. 76

Figure III.5: Increasing mesh density of the input file resolves the stresses at the edge of the ceramic, altering the location and intensity of maximum principle stress (MPa). 77

Figure III.6: Increasing mesh density in ABAQUS CAE resolves the stresses at the edge of the ceramic (MPa). 78

Figure III.7: Reduced integration linear mesh (left) when compared with reduced integration quadratic mesh (right) does not result in the same maximum von Mises stress on the surface or the appropriate peak stress at the edge of the joint. 79

Figure III.8: The fine reduced integration quadratic mesh (left) has very similar stress results as the coarse mesh (right). 80

Figure III.9: Paths used to study mesh convergence in Figure III.10. 81

Figure III.10: Mesh convergence of linear and quadratic reduced order elements along two paths. 82

Figure III.11: Mesh convergence, comparing full integration to reduced integration elements. 83

Figure III.12: The full integration linear elements produce roughly the same result at integration points regardless of mesh density. 84

Figure III.13: Quadratic full integration elements give similar results to the reduced integration elements of Figure III.8. 85

Figure III.14: The maximum principal (bottom) and von Mises stress (top) of a 4 x 4 square celled honeycomb hybrid structure cooled from relaxation temperature (1000K) to RT (293K) is greatest at the joint of the ceramic and metal (0.86 x 0.86 x 3cm, 120μm thick walls). Both the reduced and full integration results are plotted. 86

Figure III.15: Residual stress increases as the structure is cooled. Only, the corner node at the joint is plotted for the finest linear reduced integration mesh. MOR data for fully dense YSZ is also plotted. 87

Figure III.16: Failure observed after manufacturing of hybrid structure (Eisele, 2004). Cracks formed and grew as the structure was cooled from sintering temperature to room temperature. 88

Figure III.17: The finite difference mesh (left) is much coarser than the ABAQUS mesh (right). 90

Figure III.18: The number of elements in a vertical wall, horizontal wall, thickness in the y direction and thickness in the x-direction must be specified to create the input file. 91

Figure III.19: Sample ABAQUS solution at steady state for a fuel cell stack of 3, 4x4 units has symmetry only in the x-direction since the cells generally get hotter proceeding down the stack. 93

Figure III.20: General ABAQUS thermal solution for a graded fuel cell design has no plane of symmetry..... 93

Figure III.21: Physical constraints are placed at specified nodes to anchor the structure. 95

Figure III.22: The temperature of the bottom electrolyte, near the fuel inlet, represents heating in the electrolyte during startup..... 98

Figure III.23: The temperature distribution at start-up is interpolated from the results of the finite difference code. Moving left to right and top to bottom: 1) The fuel cell begins at RT. 2-3) Hot inlet air heats the structure. 4) The chemical reaction begins to heat the electrolyte. 5-6) The air temperature is now below the operating temperature, resulting in convective cooling. 99

Figure III.24: During cool down, the maximum stress component is the peeling stress (tensile), and it occurs at two spots in the ceramic at around 400K. 100

Figure III.25: At steady state operating temperature, the ceramic is put in compression due to the plastic deformation of the metal..... 101

Figure III.26: Stress results during operation of hybrid SOFC at the joint of the ceramic and metal, evaluated at the integration point (0.0577mm from joint). 102

Figure III.27: Stress in the joint at the air inlet occur even if the metal and ceramic have the same CTE (using reduced integration elements). 103

Figure IV.1: Radiation emitted from one wall continues on a random vector until it is intercepted by an opposing wall (Yakabe et al., 2001)..... 110

SUMMARY

This research characterizes the thermal stress resulting from temperature gradients in hybrid solid oxide fuel cells that are processed using a novel oxide powder slurry technology developed at Georgia Tech. The hybrid solid oxide fuel cell is composed of metallic interconnect and ceramic electrolyte constituents with integral mechanical bonds formed during high temperature processing steps. A combined thermo-mechanical analysis approach must be implemented to evaluate a range of designs for power output and structural integrity. As an alternative to costly CFD analysis, approximate finite difference techniques that are more useful in preliminary design are developed to analyze the temperature distributions resulting from a range of fuel cell geometries and materials. The corresponding thermal stresses are then calculated from the temperature fields using ABAQUS. This model analyzes the manufacturing, start-up, and steady state operating conditions of the hybrid solid oxide fuel cell.

CHAPTER I

BACKGROUND

I.1. The basics of solid oxide fuel cells

As the applications for fuel cell technology grow, the need for compact, high power density designs has drawn researchers to Solid Oxide Fuel Cells. By utilizing an ion-conducting, ceramic electrolyte, SOFC's have the potential for broad applications for which proton exchange membrane fuel cells or other liquid electrolyte fuel cells may not be easily adapted.

Fuel cells generate power through the chemical reaction of oxygen and hydrogen. The chemical reaction is made possible by the function of the PEN (positive-electrolyte negative), a component composed of an anode, electrolyte and cathode. The electrolyte is basically an ion-conducting (oxygen ion) membrane that separates the air and hydrogen, allowing the conduction of oxygen but not allowing much conduction of free electrons. When hydrogen reacts with oxygen at the anode, two electrons associated with the oxygen atom are replaced with hydrogen, producing water and electricity. These electrons are freely conducted through an external circuit back to the cathode where they dissociate the incoming supply of O_2 molecules, thus sustaining the reaction. Electricity is produced as the electrons move through the external circuit. A basic schematic for the fuel cell reaction is shown in Figure I.1.

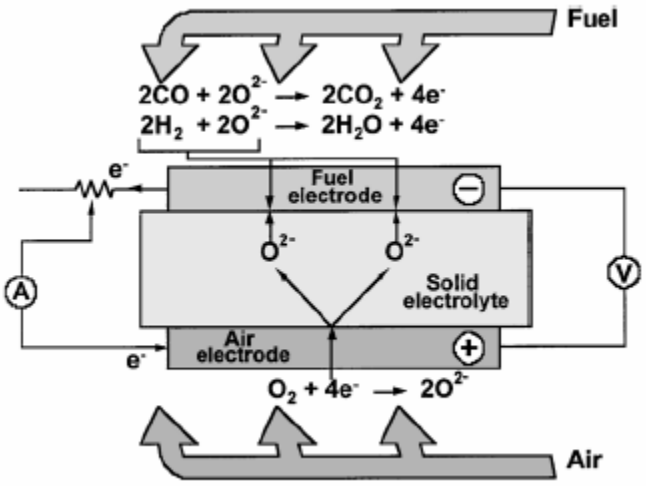

Figure I.1: In the electrochemical reaction of SOFC's, oxygen and hydrogen react to produce water and electricity (Singhal, 2000).

Note that the materials are tailored for SOFC operation. Yttria-stabilized Zirconia (YSZ) is essential for the fuel cell reaction. For this reaction to occur the temperature of the structure must be above an activation temperature, usually at least 600°C. Conventional SOFC's operate in the range of 1000°C for higher efficiency (Singhal, 2000). However, a new demand has developed for efficient, low operating temperature fuel cells (600-700°C).

I.2. Current monolithic SOFC technology

Optimal design and fabrication of SOFC's is contingent upon satisfying electrical performance, mechanical integrity and manifolding requirements (Minh and Takahashi, 1995). The voltage collected from an SOFC is less than the theoretical potential because of polarization (losses). The overall polarization of an SOFC, which determines voltage efficiency, has four key constituents: activation, diffusion, reaction and ohmic polarization (Minh and Takahashi, 1995). Activation polarization or overpotential is the

amount of energy necessary to initiate the reaction. Diffusion polarization is due to the limitations of mass transport of the reactants. Diffusion polarization is only a factor when reactant utilization approaches 100% (Minh and Takahashi, 1995). Similarly, the reaction polarization is caused by the inadequate supply or removal of reactants (Minh and Takahashi, 1995). Finally, the ohmic polarization is the resistance of the material medium to electron or ion flow. The influence of each constituent on the total polarization must be determined to estimate power output for a given SOFC model. Mechanical integrity is also a key design factor. Mechanical integrity issues may include cracking, delamination, or component separation. The culprit in many cases is the stress created by dissimilarities in the coefficient of thermal expansion for the ceramic and metal fuel cell components. Finally, the fuel cell design must be easily manifolded to be practical.

Several SOFC designs seek to satisfy these design requirements. Three common designs are the sealless tubular, planar, and monolithic designs (Singhal, 2000). The tubular design is based on a hollow cylinder with an electrolyte wall. Air flows through the center of the cylinder and fuel passes over the outside. Measured progress has been made in the development of power generating tubular SOFC's. The planar design consists of alternating flat PEN plates and interconnecting (electron conducting) ribs. The planar design has a high power density and can be stacked for optimal power production. However, the flat layers must be sealed at the edges to prevent gas from escaping. The high-temperature seals must also withstand the stresses developed by the expansion of the interconnect and electrolyte. Seal design has significantly slowed the progress of planar SOFC design (Singhal, 2000). The last design is the monolithic

SOFC. As with the planar design, the monolithic has a flat PEN component. However, the electrolyte layer is corrugated to increase efficiency. Figure I.2 shows a generic monolithic SOFC design.

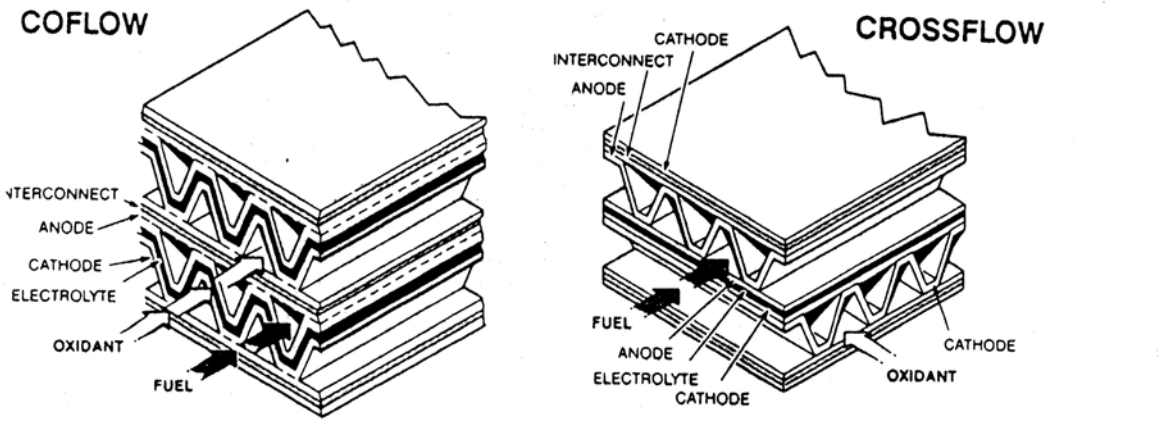

Figure I.2: Monolithic SOFC design (Minh and Takahashi, 1995)

The monolithic design has the highest power density, resulting from the close proximity of the interconnect layers (Minh and Takahashi, 1995). A short path reduces losses due to the high electrical resistance of the ion conducting membrane. Secondly, the resistance of this electrolyte layer is proportional to the cross-sectional area. Thus, the thin walls, inherent to this structure, also function to reduce ohmic losses. The principal disadvantage of the monolithic design is fabrication of the corrugated structure (Minh and Takahashi, 1995).

Tape casting or calendaring is the current method for manufacturing monolithic SOFC's. Ceramics are commonly made through a sintering process. Before sintering, the ceramic is a pliable oxide easily shaped into the ribbed structure shown in Figure I.2. The ceramic layer plus binder are then rolled together with the electrode material to form the layered PEN structure. The PEN is cofired and layered with the metal interconnect.

Tape casting must be carefully controlled and does not offer much design flexibility. In fact, the fabrication is so problematic that it is not being pursued further (Singhal, 2000).

The light weight structures group at Georgia Tech has pioneered a technique to co-extrude and co-sinter the ceramic and metallic layers. By co-extruding the layers, the ceramic, electrolyte and binder are naturally pressed together during fabrication. For the metal alloy and ceramic to be extruded at low temperatures, they must both be in an oxide powder form. The metal and ceramic powders are each mixed with a binder and other additives to form slurries. The material is then pressed through a die. The resulting alloy structure is thus composed of an array of cells with a constant cross-section due to extrusion. For this reason, parts made by this technique are called linear cellular alloys (LCA's). A schematic of the manufacturing process is shown in Figure I.3.

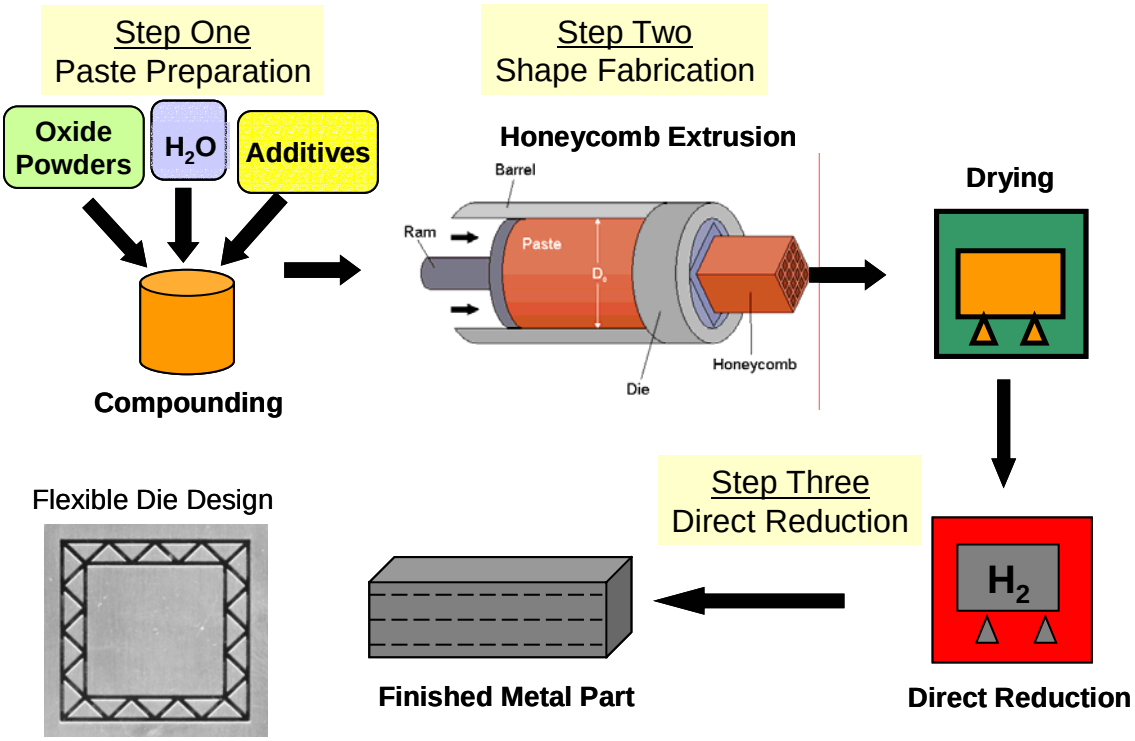

Figure I.3: Co-extrusion fabrication process beginning with oxide powders and ending with the finished linear cellular alloy (LCA).

In addition to sintering, the metal must under go reduction in a hydrogen atmosphere to remove oxygen present in the oxide powder slurry. A distinct advantage of co-extrusion is the range of designs possible. The ceramic walls can vary in thickness and shape simply by modifying the die used in extrusion. As a result, the co-extrusion process has the potential to manufacture SOFC's on a large scale with minimal cost. Figure I.4 shows a hybrid LCA SOFC.

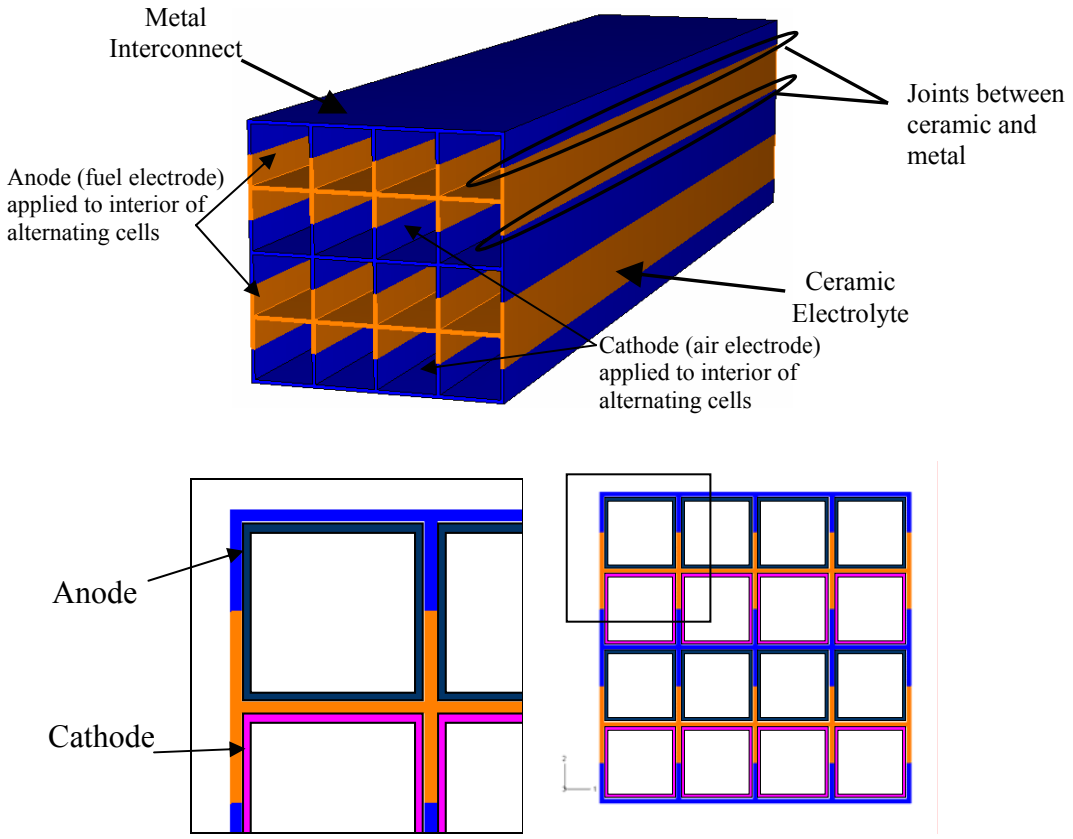

Figure I.4: The hybrid LCA SOFC has a honeycomb structure (top). The thin anode and cathode are applied to the inside of the channels after the honeycomb is fabricated (bottom). The electrode thickness is exaggerated for clarity.

However, the advantage of the Georgia Tech design is also a fundamental problem: the metal and ceramic must be co-sintered. The drastic difference in volume reduction as the

structure is cooled from sintering temperature to room temperature potentially creates a great deal of internal stress.

I.3. Thermo-mechanical stress during the operation of hybrid LCA SOFC's

Stresses induced by the difference in the coefficient of thermal expansion (CTE) of the ceramic and metal components, may cause serious problems in the fabrication and durable operation of the SOFC. The CTE of the two materials may be tailored by slight changes in the metal alloy, but even with custom material properties, the mismatch exists. Figure I.5 shows an exaggerated view of the strain caused by the mismatch.

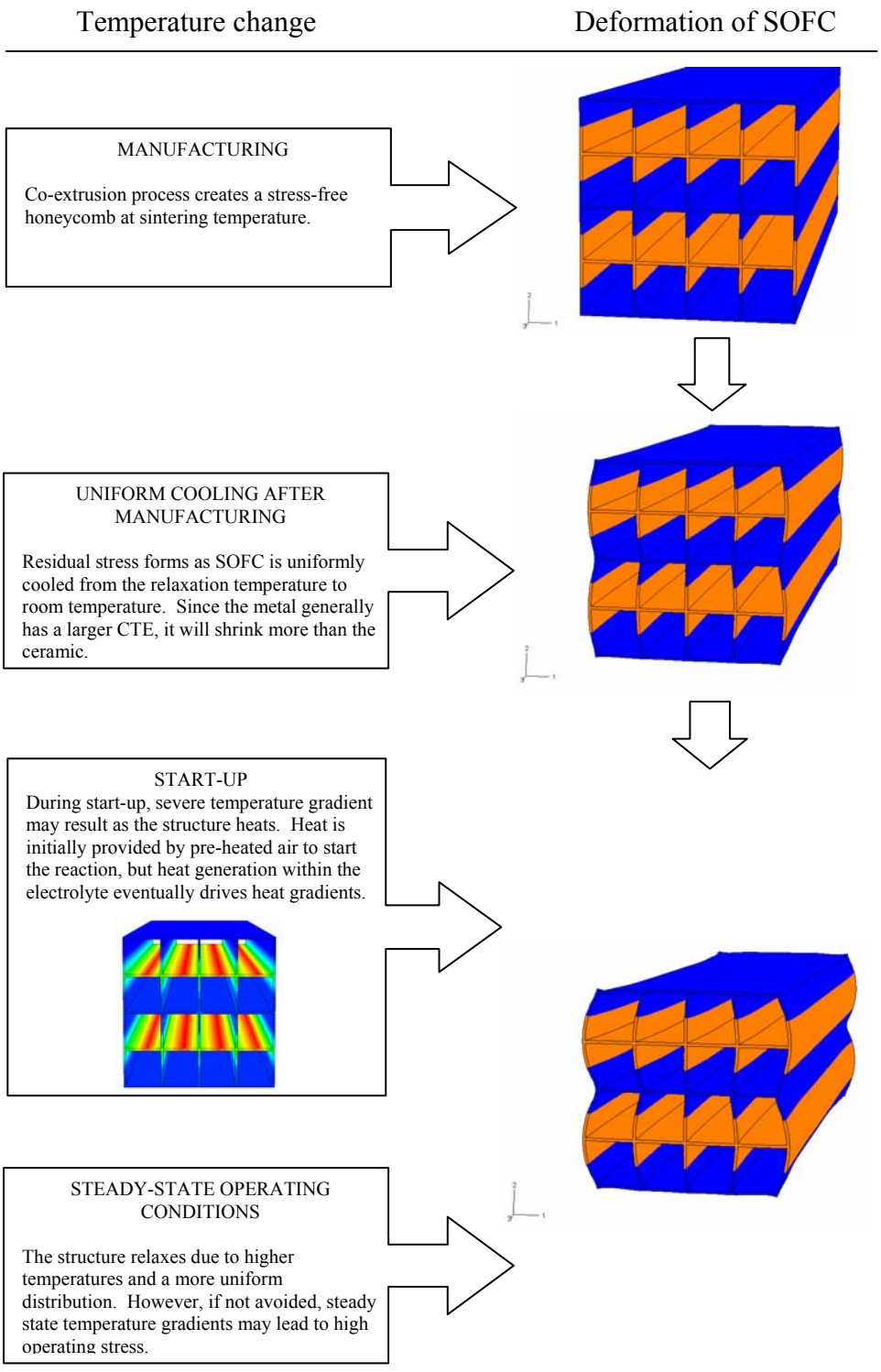

Figure I.5: The hybrid SOFC is subjected to a variety of stress from manufacturing through steady state operation.

I.3.1. Fabrication

At room temperature, the hybrid SOFC is not stress-free. After fabrication, as the hybrid structure is cooled from a high sintering temperature (i.e., stress-free temperature) to room temperature, residual stress builds. In this work, residual stresses are calculated in ABAQUS by thermo-elastic and thermo-plastic modeling of stress-strain behavior using non-linear property data obtained from testing of the material constituents. The results are intended to support comparison of geometry and material options for the reduction of residual stress, as a design-support tool. Thermo-elastic modeling has often been used to determine residual stress in modeling of typical planar SOFC's. Residual stress in planar models is relatively low because the electrolyte is only constrained by the thin layers of anode and cathode. However, in the hybrid SOFC, with the intimate connection between ceramic and metal, high stresses induce plastic deformation in the metallic phase, necessitating an elastic-plastic model. Experimentation has recorded very large residual stresses in ceramic-ceramic laminates as shown in Figure I.6 (Cai et al., 1997b). Tape-cast Alumina (Al_2O_3) and Zirconia (ZrO_2) were laminated at 90°C and 48 MPa; baked at 450°C to burn out the binder; and sintered at 1530°C. After sintering they were cooled slowly to enable the material to equilibrate (Cai et al., 1997a).

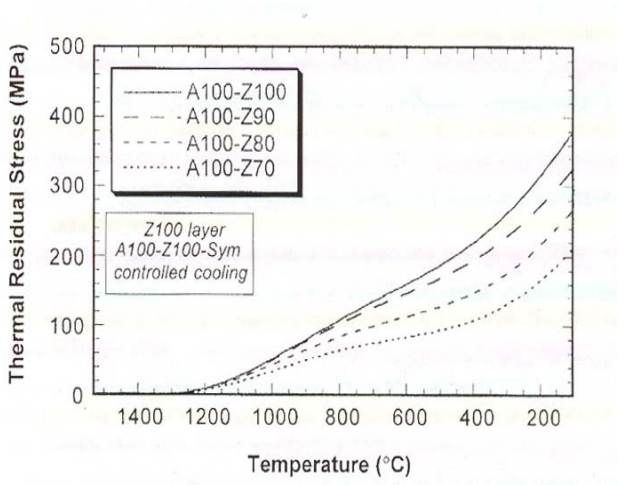

Figure I.6: Calculated cooling residual stress due to thermal expansion mismatch between various Zirconium oxides and Alumina (Cai et al., 1997b).

To fully model stress during fabrication, the mechanisms of sintering and reduction should be considered as the structure is heated from room temperature to sintering temperature. The transformation from powder-binder slurry to metal or ceramic involves a large reduction in volume. During this process, significant cracking is possible under the wrong manufacturing conditions. To the extent that cracking does not reduce stresses, residual stresses will also develop due to the volume reduction inherent in sintering. Both of these effects are outside of the scope of this thesis. Eisele (Eisele, 2004) is developing a full model of sintering and reduction stresses to optimize variables such as isothermal hold time, sintering temperature and material properties. A commonly held assumption, validated by experiments, is that the elastic mismatch stress due to sintering and reduction is almost fully relaxed due to viscous behavior at temperatures above a relaxation temperature (Cai et al., 1997b). Therefore, for the purposes of characterizing residual stress at room temperature, the thermo-plastic behavior from a

stress-free relaxation temperature to room temperature is a reasonable assumption until more detailed studies can be performed.

I.3.2. Stresses occurring during operation

As planar SOFC design reaches the stage of implementation, much research has focused on mechanical integrity during operation. Although the planar design has a few key differences from the hybrid, both have the same basic components and, thus, similar stress issues. Contributors to stress during SOFC operation include: residual stress level, creep at high working temperatures, thermally-induced stress, thermal shock, mechanically applied stress, fatigue, and stress concentrations such as edge effects. Failure potential will be evaluated not just on catastrophic failure, but also on cracking potential and compromise of hermetic joints, both leading to unacceptable losses in efficiency. Also, creep will be neglected. The onset of creep in YSZ is around 1250°C, depending on material properties (Cai et al., 1997b). Also, creep tests on the metal interconnect, $Fe_{39}Ni_8Cr$, show the onset of creep to be between 700°C and 900°C (Eisele, 2004). Since the hybrid SOFC is designed for low operating temperatures (600°C-700°C), creep does not represent a substantial risk for failure. At elevated operating temperatures, $Fe_{39}Ni_8Cr$ may experience limited creep, but the material is continually being altered. Judging from the relatively low elasticity and high porosity of the tested samples (Eisele, 2004), creep figures to be less of a risk in the final material. As the interconnect material is further developed, more substantial testing would make possible the use of a creep material model in ABAQUS if necessary. Also, mechanically applied stress is not a significant factor in hybrid SOFC design either. The hybrid designs do not

include any external forces with the exception of stack weight (the weight of the material above a stress point). Stresses due to weight are negligible compared to the strength of the structure but are none-the-less factored into the ABAQUS model.

I.4. Failure in the hybrid SOFC

I.4.1. Thermally-induced stress within a homogeneous material

Thermally-induced stresses exist due to steady state thermal gradients in a metal or ceramic. Figure I.7 shows the significance of thermal stress gradients on YSZ ceramic.

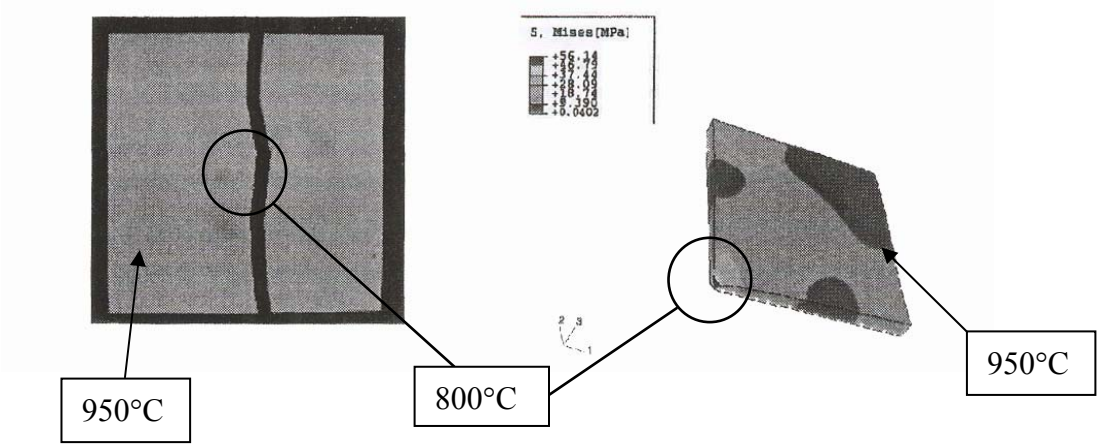

Figure I.7: Gradual flow increase of a cool jet stream, directed at the center of a 50 mm square specimen, resulted in fracture due to the induced temperature gradient (Hagos and Travis, 2003).

Essentially, a temperature gradient causes an expansion differential within a homogeneous material. Since the elevated exterior of the plate is expanding and the interior is shrinking, a state of tension is created within the material. Tensile forces open

cracks, resulting in the failure shown in Figure I.7. Design sensitive to thermally-induced stress focuses on minimizing temperature gradients to sub-critical levels.

I.4.2. Thermal Shock

Thermal shock shares many characteristics with thermally-induced stress, except that its behavior is time dependent as well as spatially dependent. The experimentation, shown in Figure I.7, was designed to isolate thermally-induced stress and avoid thermal shock by slowly increasing the cool jet stream velocity (Hagos and Travis, 2003). If a surface is cooled or heated rapidly, the temperature distribution is not at equilibrium. Classic approximate values for thermal shock will be employed to determine the shock resistance of the material and the approximate critical limit of the surface cooling rate (Hasselman, 1970).

I.4.3. Thermal stresses arising from the CTE mismatch between components

The main focus of modeling in this research will be on stress resulting from the CTE mismatch of the materials. The intimate connection between the interconnect and the electrolyte constrains the two components. Extremely large stresses may arise from this constraint. Further stress will be contributed by the anode and cathode. However, in this work, the stress contributions of the anode and cathode will not be considered for several reasons. The electrodes are very thin. Testing of screen printed anodes (NiO/YSZ) on a plate of YSZ showed the residual stress in the anode was a low 11 MPa (Selcuk et al., 2001). The low stresses in the anode resulted from stress relieved by channel cracking of the anode material. The residual stress due to the anode caused little change in the strength of the electrolyte. The cathode ($La_{0.75}Sr_{0.2}MnO_{3-\delta}$), also applied to

a YSZ plate by screen printing, caused a slightly larger residual stress of 39 MPa (Selcuk et al., 2001). The effects of this residual stress should have been minimal given the low strength of the cathode, but the application of the cathode was found to significantly reduce the strength of the YSZ plate from 374 to 182 MPa (Selcuk et al., 2001). Selcuk suggested impurities or damage during processing of the cathode/electrolyte laminate must have weekend the electrolyte (2001). Assuming the strength of the electrodes in the hybrid SOFC case are on the order of the planar SOFC, the electrodes should fail before having a significant effect on the overall structure. Electrolyte damage or cracking may be exacerbated by the presence of electrodes, but flaws and defects are not modeled in this work. Moreover, the anode and cathode are still experimental at this stage of hybrid SOFC development. As such, very little is known about the mechanical properties of the final deposit. Therefore, the main thrust will focus on the first-order residual stresses arising from the direct joining of ceramic and metal components.

I.5. Failure criterion

Metal failure will be defined as the point when von Mises equivalent stress in the material reaches the ultimate tensile strength. The metal will have significant plastic hardening upon cooling to room temperature. Fracture in the ceramic will occur when the maximum principal stress exceeds the modulus of rupture or ultimate tensile strength of the ceramic. Temperature dependent strength must be considered. The ceramic significantly weakens at high temperatures. The failure limits will therefore be temperature dependent. Values of the modulus of rupture (MOR) for 8% mol YSZ and are given in Table I.1.

Table I.1: Modulus of rupture data for 8% mol YSZ (Du et al., 2003)

Temperature	20C	600C	800C	1000C
MOR	325 MPa	230 MPa	240 MPa	247 MPa

I.6. SOFC thermal stress analysis on planar models

The hybrid honeycomb structure is a new SOFC design, conceived at Georgia Tech, aimed at producing high power density at a much lower cost. Among the traditional designs, the planar structure most closely resembles the hybrid SOFC. The most notable change is the shape of the electrolyte. In the planar design, the electrolyte is a flat plate, fabricated by tape casting. The anode and cathode are applied to either side of the electrolyte creating a PEN structure. A ribbed interconnect layer is located above and below the PEN structure to extract current. The outer edges of the electrolyte-interconnect intersection are plugged with glass seals to prevent leaking of gasses. One such planar SOFC design is given in Figure I.8.

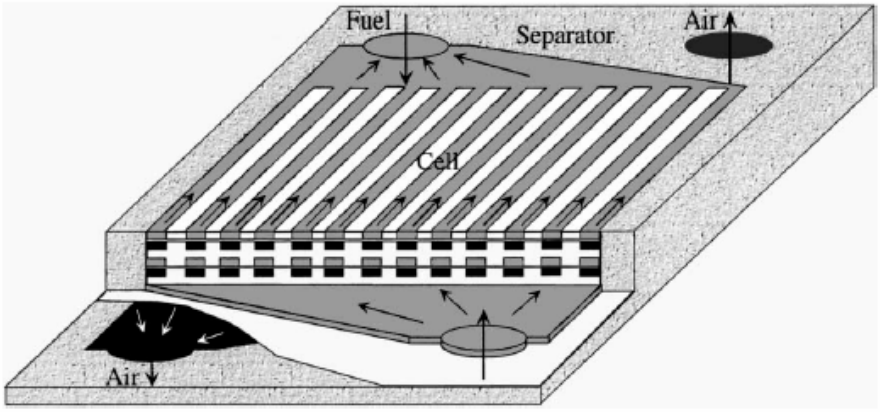

Figure I.8: Planar SOFC design showing PEN structure, interconnect and manifolding technique (Yakabe, 2001).

The SOFC integrates the ion conducting properties of ceramics with the electron-conducting properties of a metal to produce and extract power. The PEN structure must be assembled into stacks and sealed at the edges to become operational. The hybrid structure, by virtue of co-extrusion, needs no seals and little assembly since the metal and interconnect are in intimate contact. Unfortunately, ceramics and metals have very different thermal expansion coefficients. Since the structure operates over such a large temperature range, the temperature change can cause stress by a variety of different mechanisms. These mechanisms include: residual stress, thermally-induced stresses, thermal shock, CTE mismatch, material creep, and fatigue through thermal cycling (Yakabe et al., 2001; Hagos and Travis, 2003). Failure can occur at the joint of the metal and the ceramic, in the ceramic, in the metal, or at the interface of the electrolyte, anode or cathode. The planar SOFC structure has been modeled through the use of math models and finite element analysis (Yakabe et al., 2001; Keegan et al., 2002). Yakabe developed a mathematical model for fuel cell electrochemistry. This model was implemented into a thermo-fluids model created in STAR-CD, a CFD program. The results of the CFD code were then inserted into ABAQUS for stress analysis. Yakabe (2001) compared the results with and without the inclusion of radiation heat transfer. However, the analysis was steady state only. Furthermore, the cell components could deform freely. The stresses on the unrestricted components are expected to be much less than in the hybrid SOFC case. The metal-ceramic bond will significantly increase the stress within each component. The work by Keegan (2002) analyzing an automotive application of an SOFC was unique in that it considered transient conditions. The electrochemistry model was based on a performance program called Aspen. Aspen is a

custom code that references tabulated performance results. Additionally, calculations were made for polarization effects present in the model. The results from Aspen were fed into STAR-CD for thermo-fluid analysis. In turn, the temperature fields from STAR-CD were used in ANSYS to model transient stress distributions. Both models are "multi-tool" approaches to SOFC analysis. They make efforts to link electrochemistry, thermo-fluid and thermo-elastic stress analysis as a basis for a complete SOFC analysis. The work, herein, is different for two reasons. First, the structure of the hybrid SOFC differs slightly from the planar, but with large ramifications. Secondly, finite difference techniques should significantly reduce the time necessary to complete the multi-tool analysis. The tools developed will be automated to a large degree, dependent on only a limited number of inputs from the user. None-the-less, the models by Yakabe and Khaleel, due to their similarity to this work, help substantiate the techniques used for modeling hybrid SOFC performance.

I.7. Temperature field calculation

To characterize the operating stress state, two separate computational models must be used to calculate the temperature field and thermal stress. The design consideration is broad due to the versatile and inexpensive method of fabrication. Thus, a good model is one that is quick and versatile. For the thermal model, finite difference techniques are developed to compute the temperature distribution. The finite difference model runs in a fraction of the time necessary to run a commercial CFD code such as FLUENT, and is therefore of considerable value in preliminary design of stacks to mitigate against stress.

I.8. Motivation

Design in the field of planar SOFC's has, for the large part, focused on electrochemical performance. As an end, obtaining high efficiency has motivated development of SOFC technology. However, with continued maturation of SOFC technology, practical implementation is shifting to focus on solving stress issues inherent in fuel cell design. This work combines the two considerations by developing a "multi-tool" approach to fuel cell design.

CHAPTER 2

FINITE DIFFERENCE-BASED THERMAL ANALYSIS OF SOFC'S

II.1. Introduction

Evaluating the stress in SOFC components is critically important in both the manufacturing and operation of reliable fuel cells for several reasons. Fatigue and large scale fracture are certainly concerns in fuel cell design, but even minor cracking along the joint between the metal and ceramic components could compromise the hermetic seal. The relative intolerance of the fuel cell design to fracture and fatigue motivates optimization of design based on a combination of electrical efficiency and mechanical integrity. Since no fully operational prototype yet exists, the best option is to simulate an array of fuel cell designs. Several commercially available FEM programs exist capable of thermal and structural modeling. Two such programs, ABAQUS and STAR-CD, have been used in combination to analyze thermo-mechanical stress in planar SOFC's (Yakabe et al., 2001; Keegan et al., 2002). However, FEM software is limited by computational time and design flexibility due to mesh generation. For a limited number of design variations, the computational time required is acceptable; for many designs, however, optimization would require that the computational time be reduced. Alternatively, the thermal analysis may be performed by a finite difference (FD) technique. The formulae solved with the finite difference method may be based on simplifying assumptions for specified conditions in order to reduce computational time. As with any modeling, the assumptions of the FD technique need to be corroborated by experimentation or by more complex models to ensure accuracy. The thermal analysis may be completed by an FD

code, separately from the mechanical analysis that is performed by ABAQUS. In other words, the two may be one-way coupled; in this case, mechanical deformation does not affect the thermal problem, but the temperature field affects mechanical properties and thermal strain.

The FD method has been used successfully at Georgia Tech to design honeycomb shaped heat sinks (Dempsey, 2002). A FORTRAN code was written by Dempsey to assemble and solve the finite difference equations under steady state conditions. The heat sink FORTRAN code provided an excellent starting point for thermal analysis in fuel cells. However, the code needed to be significantly expanded to address transient analyses, as well as the added effects of cross-flow, hybrid material structure, and internal power generation.

The finite difference formulae may be obtained by either a PDE replacement method or an energy balance method. The PDE governing heat conduction is (Croft and Lilley, 1977)

$$\nabla \cdot \left(k \nabla \underline{T} \right) + H = \rho C_p \frac{\partial T}{\partial t} \tag{II.1}$$

Using the heat PDE for conduction, the second order derivative must be evaluated by finite difference to solve for temperature. Evaluating the second derivative by finite difference becomes more complicated for variable mesh sizes, convective boundary conditions and odd mesh shapes (Croft and Lilley, 1977). Alternatively, the energy method is a first order equation based on the conservation of energy for a control volume (Incropera and Dewitt, 1996). Since the energy equation is simpler to apply, it will be used as a basis for the FD analysis.

II.2. Model setup and boundary conditions

The thermal problem involves fluid flow through rectangular ducts, conduction through the ceramic and metal walls, and heat generation within the ceramic. The problem setup is depicted in Figures II.1 and II.2.

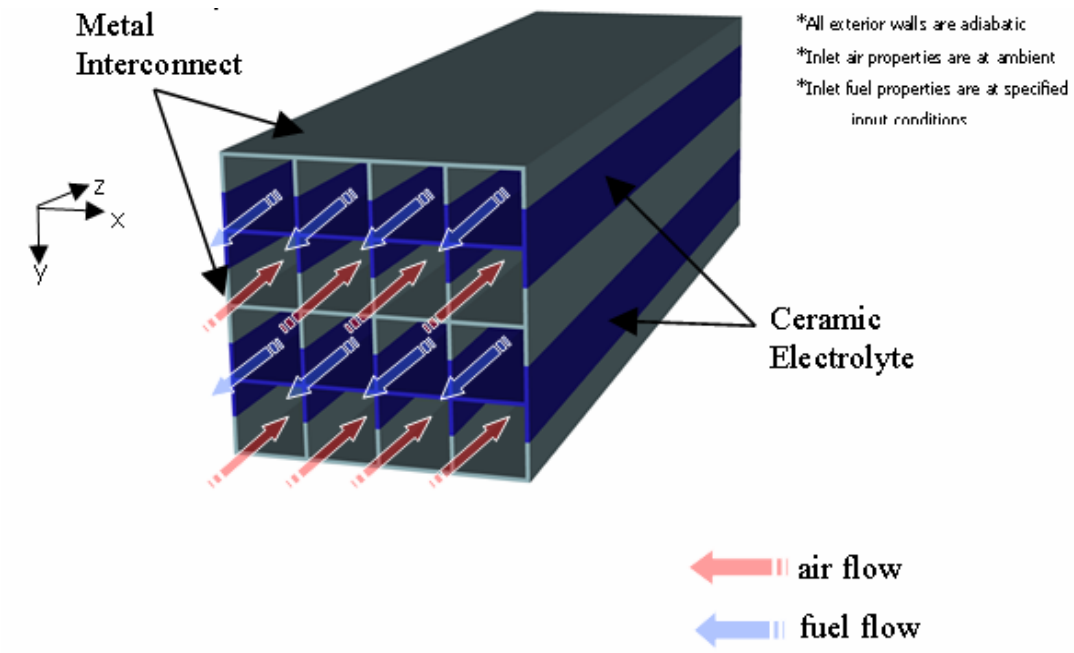

Figure II.1: The hybrid SOFC design has alternating layers of metal and ceramic components acting as the interconnect and electrolyte respectively, and air and fuel are in counterflow.

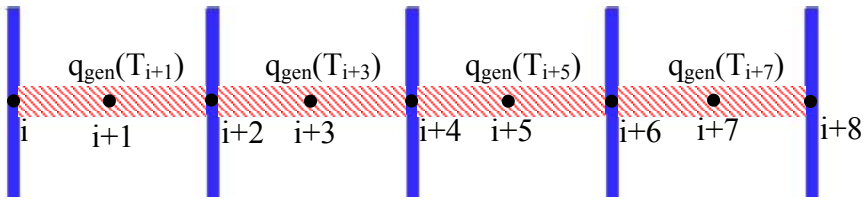

Figure II.2: Heat generation in the FD code is applied directly to the indicated regions within the electrolyte.

Beginning first with the fluid, air and hydrogen alternate with each row and move in a counterflow pattern. The inlet temperature and mass flow rate of the air and hydrogen are sufficient to characterize the fluid properties throughout the channels. The solid structure is assumed adiabatic on all sides. The exposed faces are assumed adiabatic as well. The honeycomb has a hybrid structure as shown in Figure II.1 with the darker being a ceramic electrolyte and the lighter, a metal interconnect. For each metal, the conductivity, specific heat, as well as all relevant geometric dimensions must be supplied. Finally, Figure II.2 shows the regions at which heat generation occurs. Heat generation in the SOFC has several contributors. Electrical current resulting from the fuel cell reaction passes through the anode and cathode. The electrical resistance of these materials and the entropy change of the chemical reaction result in heat generation (Minh and Takahashi, 1995). Specifically, the reaction site is at three-phase boundaries, the intersection of gas, electrode, and electrolyte (Minh and Takahashi, 1995). Due to the coarse mesh of the FD code, the heat generation was simply applied to the sections of electrolyte indicated in Figure II.2.

II.3. Discretization of geometry in the finite difference code

In order to use the energy method, the fuel cell geometry must be partitioned into small, but finite control volumes, called "elements." A node is at the center of each element. An energy balance is applied over each element to determine the temperature of the center node. When the energy equations for all of the center nodes in the model are assembled, the temperature field can be calculated. The mesh assumed in this study is shown in Figure II.3. In view of temperature gradients along and through walls, this

mesh is relatively coarse in order to enhance solution efficiency for purposes of preliminary design.

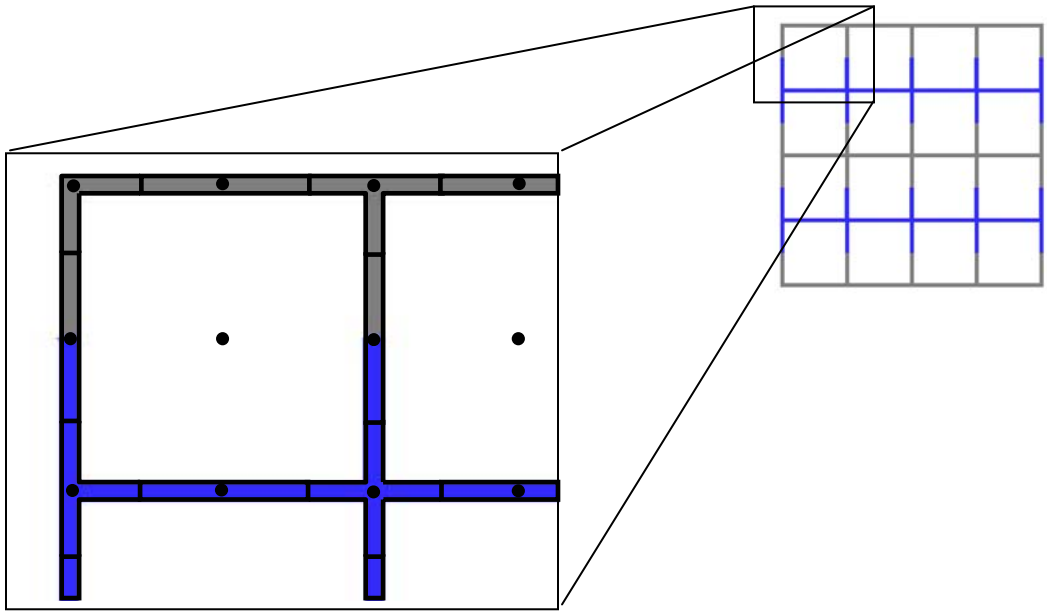

Figure II.3: Discretization of honeycomb structure into finite elements.

The honeycomb structure has square cells that can be divided to create a repeating mesh. The four basic shapes used are shown in Figure II.4.

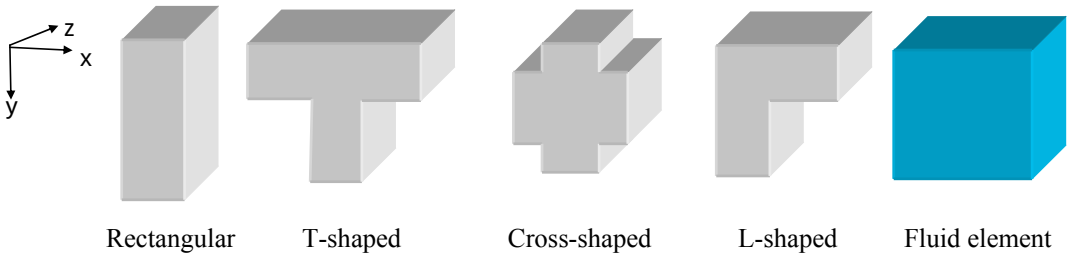

Figure II.4: Mesh geometries resulting from discretization of the honeycomb structure.

Since the fuel cell is fabricated by extrusion, the geometry is projected in the z-direction. Thus, the honeycomb can be divided into x-y planes along the length, having the same mesh in each plane. A major advantage of the energy balance method is the ease at which oddly shaped geometry can be discretized. By considering each element as a distinct control volume, the center node represents the entire region (Croft and Lilley, 1977). No matter how complex or distorted the geometry of the control volume, the overall temperature of the element is only affected by the net energy through the boundaries of the control volume. In general, with smaller elements, the temperature of the center node better approximates the temperature of the element in terms of temperature gradients between the element and the surrounding fluid or solid element.

When assembled, each of the elements in Figure II.4 has a center node and ten surrounding nodes. The set of 11 nodes, including the center node, form a local coordinate system. The local coordinates are consistent for each element, with a numbering scheme based on direction. Figure II.5 shows the local numbering scheme.

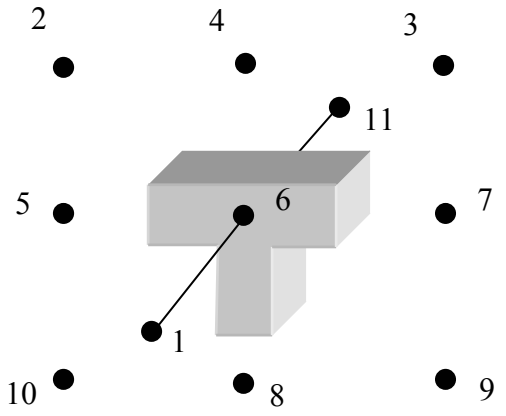

Figure II.5: The local numbering scheme for the finite difference elements is comprised of a center node (#6) surrounded by eight in-plane and two out-of-plane nodes.

With this configuration, each element has eleven potential contributors to heat transfer. For example, consider a solid element like the one shown in Figure II.5. Directions 2, 3, 9 and 10 are always convection (if they exist), and 1 and 11 are always conduction. The mode of heat transfer for the other directions varies on the location of the element. With certain repeating or regularly alternating characteristics, the energy balance for each of the five cells shown in Figure II.4 can be assembled.

Convection is solely responsible for removing heat from the fuel cell. Modeling of heat and mass transport through the fluid is centered on the mean temperature of the fluid. The mean temperature determines the rate of energy transported by the fluid. Also, Newton's law of cooling, the formula for convection, can be referenced to the mean temperature (Incropera and Dewitt, 1996). If, in each cross section of elements, the entire fluid rectangle is considered one element, then the temperature of the center node is the mean temperature. The fluid element has the same local numbering as solid elements. The direction of the flow is determined by whether the local node number 1 or 11 is used for the inlet fluid flow temperature.

The elemental equations must be assembled into a global numbering scheme to link the interdependent element temperatures. Element number 1 is on the front face in the top left corner. Elements are numbered from left to right, top to bottom and front to back sequentially, as shown in Figure II.6.

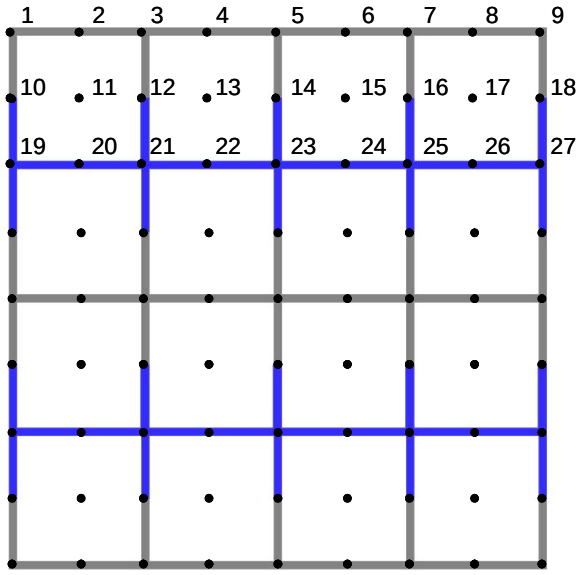

Figure II.6: The global coordinate numbering scheme (shown for a 4x4 cell geometry) begins with node 1 in the upper left corner and numbers sequentially in the positive x, y and z directions.

II.4. Governing Equations

II.4.1. Steady state problem

The conservation of energy for any element can be represented by (Incropera and Dewitt, 1996)

$$\dot{E}_{in} + \dot{E}_{gen} = \dot{E}_{out} + \dot{E}_{storage} \tag{II.2}$$

The energy generated term in this model refers to heat generation because of the electro-chemical reaction. The energy transfer in and out of the cell can either be by conduction or convection. Although other models show the effects of radiation may be significant, they are not implemented in the FD code. Considering first a steady state formulation, the energy storage is zero. Therefore, the energy balance reduces to

$$\dot{E}_{in} + \dot{E}_{gen} = \dot{E}_{out} \tag{II.3}$$

The energy transfer for solid elements due to conduction can be calculated through Fourier's Law (Equation (II.4)); convection is described by Newton's Law of Cooling (Equation (II.5)) (Incropera and Dewitt, 1996), i.e.,

$$q_{conduction} = kA\left(\Delta T\right), \text{ and} \tag{II.4}$$

$$q_{convection} = hA\left(T_s - T_m\right), \tag{II.5}$$

where k is the thermal conductivity, h is the overall convection coefficient, A is the area normal to the heat transfer direction, and ΔT is the difference in temperature over which the heat transfer takes place. Also, T_m is the mean fluid temperature, and T_s is the wall surface temperature. Equation (II.5) is altered slightly in the finite difference code. The

wall surface temperature, T_s, is replaced by the center temperature for the wall element. The substitution is reasonable since the walls are extremely thin and will not maintain much of a temperature gradient in reality.

The energy balance for fluid cells is slightly different. Conduction between fluid elements is neglected so that the only mode of heat transfer for a fluid element is convection from the walls of the channel and mass transport through the cell. The heat transfer rate due to mass transport is given as (Incropera and Dewitt, 1996)

$$q = \dot{m} c_p \left(\Delta T \right), \tag{II.6}$$

where c_p is the fluid capacitance, $\dot{m}$ is the mass flow rate, and ΔT is the difference in temperature between the control volume and the neighboring fluid cell upstream. The last term in the energy balance is the heat generation term. The heat generation is volumetric (W/m^3) and depends on the mean temperature of the volume it is characterizing. The magnitude of the heat generated over a range of temperatures will be discussed in the material properties section of this chapter.

II.4.2. Transient problem

In the transient case, the $E_{storage}$ term in Equation (II.2) must be calculated. The storage term is a function of time and can be phrased in finite difference terms as (Croft and Lilley, 1977)

$$\dot{E}_{storage} = \left(\rho c_p \frac{\Delta T}{\Delta t} \right) V \tag{II.7}$$

Here, V is the volume of the element. The implicit approximation of the time derivative is used, i.e. $\frac{dT}{dt} \approx \frac{\Delta T}{\Delta t}$. The implicit approximation evaluates the temperature of a center node, at time S+1, based on the surrounding nodes, at time S+1, and the center node, at time S (Incropera and Dewitt, 1996).

II.5. Approximation of material properties

II.5.1. Fluid properties and curve-fitting

The assumptions for the fluid properties of air used to calculate the average convection coefficient are adapted from the preceding work of Dempsey (Dempsey, 2002). In the range of Reynold's numbers considered for this SOFC, the flow is always laminar. Therefore, the Nusselt number is constant for the aspect ratio of the square fluid cell. Incropera and Dewitt provided conductivity data for hydrogen and air which was curve fitted over the operating region. Through the relationship in Equation (II.8), the convection coefficient can be calculated (Incropera and Dewitt, 1996) as

$$h = \frac{Nuk_f}{d} \tag{II.8}$$

where Nu is the Nusselt number, k_f is the fluid conductivity, and d is hydraulic diameter. The hydraulic diameter for a rectangular cross section is (Incropera and Dewitt, 1996):

$$d = \frac{4A}{P} \tag{II.9}$$

where A is the cross sectional area, and P is the perimeter. For rectangular ducts and fully developed laminar flow the Nusselt number tabulated data from Incropera and Dewitt has been curve fit by Dempsey (Incropera and Dewitt, 1996; Dempsey, 2002) as

$$Nu = \frac{6.163}{1 + e^{\frac{1.329 - \frac{b}{h}}{2.889}}} \tag{II.10}$$

where b is the base of the channel and h is the height, and the base is greater than the height. The calculated convection coefficients are shown in Figure II.7.

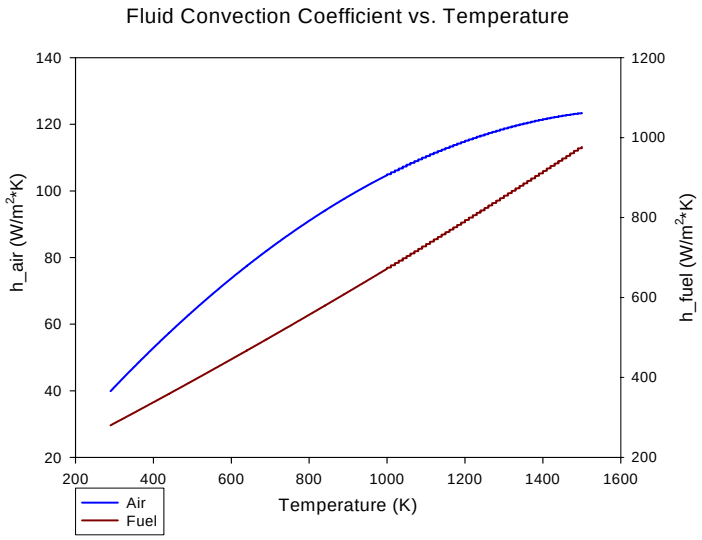

Figure II.7: Fluid Convection Coefficients for Air and Hydrogen.

The finite difference code re-evaluates properties at each fluid cell element. Alternatively, the average temperature of the fluid could have been used to calculate the convection coefficient. The error in assuming constant properties based on average temperature is small (Dempsey, 2002). However, in this case, the extra computational and programming time was minimal. Thermal entrance length was also investigated. With thermally developing flow, the Nusselt number would vary from the constant value along the entry length x^*. For the range relevant to this work, the entry length was much smaller than the depth of the first element plane. As a result, entrance effects were negligent.

II.5.2. Metal and Ceramic Properties

Several metals and ceramics were considered to minimize the CTE mismatch or increase material toughness. The initial materials investigated were INCONEL 617 and YSZ. Later the nickel and iron content of the metal were changed in an attempt to match the CTE of YSZ. Since both the metal and ceramic were formed through sintering and reduction, the final properties are greatly dependent on manufacturing conditions (Lee and Rainforth, 1994). Therefore, the mechanical and thermal models in this work had to utilize a collage of Georgia Tech test data, commercial values and test data from recent journal articles. Table II.1 and II.2 show the material properties used.

Table II.1: YSZ property data.

Temperature K	Elastic Mod. GPa	CTE µm/mK	Poisson's Ratio	MOR MPa
298	190	6.65	0.308	325
373	187	6.65	0.3085	
573	178	8.48	0.3098	
773	170	9.12	0.3111	
873	166	9.36	0.3117	230
973	161	9.57	0.3124	
1073	157	9.76	0.313	240
1273	148	10.10	0.3143	247
1400	143	10.10	0.3151	

Table II.2: Fe39Ni8Cr property data.

Temperature K	Elastic Mod. GPa	CTE µm/mK	Poisson's Ratio	Strain Hardening % Strain	Stress (Mpa)
298	160	5.40	0.25	0.309	57.682
373		5.40		0.509	66.469
473		6.70		1.03	81.526
573		9.20		1.51	92.386
673		11.00		2.02	101.96
773		12.00		2.53	110.144
873		13.10		3	117.56
973		13.20		4	132.52
1073	128	14.30	0.25	5	143.589
1173		14.70		6.02	153.84
1273		15.10		10	189.467
1373		15.10		15	219.896
1446		15.10		18.8	236
1473		15.00			

The CTE data for both YSZ and $Fe_{39}Ni_8Cr$ were collected through testing at Georgia Tech (Eisele, 2004). For $Fe_{39}Ni_8Cr$, the thermal conductivity and specific heat of INCONEL alloy 617, 13.2W/mK and 0.419J/gK respectively, were used assuming similarity of the thermal properties of $Fe_{39}Ni_8Cr$ and INCONEL. Also, the Young's modulus and Poisson's ratio data were collected from related testing (Eisele, 2004) using a sonic tester at room temperature. The data were adjusted by Eisele to reflect temperature and porosity effects in the final material (Eisele, 2004). The strain hardening data was measured through uniaxial tension testing by Eisele (Eisele, 2004). For YSZ, elastic modulus and Poisson's ratio data were extrapolated from measurements by Atkinson and Selcuk (Atkinson and Selcuk, 2000). Also, the Modulus of Rupture is referenced from published testing (Du et al., 2003). The thermal conductivity of YSZ is a constant 2W/mK taken from the literature (Minh and Takahashi, 1995). Finally, the specific heat of YSZ was approximated as 0.4536J/gK from room temperature measurements made by Tojo (Tojo et al., 1999).

II.5.3. Heat generation approximations

Ohmic losses in an SOFC result in Joule heating. Joule heating is the heat generation due to the resistance of the material to electric or ionic current. Specifically, the electrodes and interconnect conduct electricity, and the electrolyte and electrodes conduct oxygen ions (oxygen and two electrons). In both circumstances, interfacial resistance between the electrodes and interconnect or electrolyte would add to ohmic losses. Calculations for electrical flow through similar materials using approximate values for electrical resistance show that the interface and electrical resistances are negligible in comparison to the ionic resistance for the hybrid SOFC conditions (Dempsey, pers. com., 2004). In addition to Joule heating, the entropy change also correlates to heat production. Therefore, the total heat generation, including the change in entropy, can be approximated by Equation (II.11) (Dempsey, pers. com., 2004).

$$q_{total} = q_{joule,e} + q_{ent} \tag{II.11}$$

where q_{total} is the total rate of heat generation (W), $q_{joule,e}$ (W) represents the joule heating in the electrolyte and q_{ent} (W) is the heat produced by the change in entropy. The joule heating is described by (Dempsey, pers. com., 2004)

$$q_{joule,e} = \rho_e I^2 + \eta I \tag{II.12}$$

and the entropy change by (Minh and Takahashi, 1995)

$$q_{ent} = -\frac{I}{2F}\Delta H_{H_2O} - E_r I \tag{II.13}$$

where ρ_e is the ionic resistance of the electrolyte, I (A) is the current, η (V) is the activation overpotential, F (C/mol) is the Faraday constant, ΔH_{H_2O} (J/mol) is the enthalpy of formation for water, and E_r (V) is the Nernst potential. Note that the electrical current through the metal and the ionic current through the ceramic are the same since they are in

series. The ionic resistivity and conductivity are linked according to (Dempsey, pers. com., 2004)

$$\rho_e = \frac{t_e}{A_e \sigma} \quad , \tag{II.14}$$

where t_e and A_e are, respectively, the thickness and area of the electrolyte. The ionic conductivity is represented by σ and the resistivity by ρ_e. The Nernst potential is related to the partial pressure of the reactants by (Minh and Takahashi, 1995)

$$E_r = \frac{RT}{4F} \ln\left(\frac{p_{O_2,(c)}}{p_{O_2,(a)}}\right) \tag{II.15}$$

where R $\left(\frac{\text{J}}{\text{mol}\cdot\text{K}}\right)$ is the universal gas constant, $p_{O_2,(c)}$ is the partial pressure of oxygen at the cathode, $p_{O_2,(a)}$ is the partial pressure of oxygen at the anode, and T (K) is the temperature of the electrolyte. Note that the partial pressures are constants recommended by Dempsey for this fuel cell design (Dempsey, pers. com., 2004). The ionic conductivity (and, in turn, resistivity) of the electrolyte, Nernst potential, activation overpotential and current are dependent on temperature. Experimental data for Scandium-stabilized Zirconia (ScSZ) were collected by Dr. Liu's group at Georgia Tech (Dempsey, pers. com., 2004) to determine ionic conductivity, activation overpotential, and current density as a function of temperature. Until similar data is available for YSZ, ScSZ must be used. Dempsey (Dempsey, pers. com., 2004) was able to fit a series of exponential and linear functions to experimental data. The functions, based on experimentation, for activation overpotential and resistivity are given respectively as

$$\eta(T,J) = 0.001 \cdot e^{(-0.0109 \cdot T + 0.0006 \cdot J + 15.026)}, \text{ and} \tag{II.16}$$

$$\rho_e = \frac{t_{electrolyte}}{A_{electrolyte}} \cdot T \cdot 10^{\left(\frac{2769.7}{T} - 4.1806\right)} \quad . \tag{II.17}$$

Here, to be consistent with the curve fit, J must be in mA/cm^2. The total heat generation can be determined by substituting Equations (II.16) and Equation (II.17) into Equation (II.13) and then into Equation (II.12) to give

$$\begin{aligned} q_{total} = & \left(\frac{t_{electrolyte}}{A_{electrolyte}} \cdot T \cdot 10^{\left(\frac{2769.7}{T} - 4.1806\right)} \right) I^2 \\ & + 0.001\left(e^{(-0.0109 \cdot T + 0.0006 \cdot J + 15.026)}\right) I - \frac{I}{2F} \Delta H_{H_2O} - \left(\frac{RT}{4F} \ln\left(\frac{p_{O_2,(c)}}{p_{O_2,(a)}} \right) \right) I \end{aligned} \tag{II.18}$$

The result of Equation (II.18) is divided by the applied cell volume to obtain the volumetric heat generation. With the model developed by Dempsey, either the current or the voltage must be considered constant to solve the heat generation equation. The initial model by Dempsey maintained a constant current. With constant current, the electro-chemical equation yields heat generation for any supplied temperature and geometry. To provide an ample amount of power, the estimated current density at full operation is about 400mA/cm^2 (Dempsey, pers. com., 2004). However, the true current distribution at temperatures away from ideal operating temperature can not be estimated with this result. Instead, if the voltage is assumed constant over a cell face, the current can be calculated by the potential balance (Minh and Takahashi, 1995)

$$I = \frac{E_r - E_{op} - \eta(I)}{R} \tag{II.19}$$

Formula (II.19) provides a current distribution across the electrolyte, where E_{op} is the operating voltage and R is the cell resistance (assumed here to be the resistivity, ρ_e). An operating voltage of 0.7V is recommended for the SOFC design (Dempsey, pers. com.,

2004). Similar operating voltages of 0.75V to 0.7V have been used in planar SOFC designs (Minh and Takahashi, 1995; Yakabe et al., 2001; Sudaprasert et al., 2003). Since Equation (II.19) has current inside and outside of the exponential, an explicit solution for current, I, is not easy to obtain. Several simplifications have been made in other models. Sudaprasert neglects the activation overpotential at operating temperature, using the simplified Ohm's law instead (Sudaprasert et al., 2003). Also, Yakabe approximates the overpotential by assuming a constant 50mV at steady state conditions (Yakabe et al., 2001). In this analysis, since the finite difference analysis is transient, Equation (II.19) should be solved with the current dependent effect of overpotential. A root finding algorithm based on the Newton-Raphson approach is used in the finite difference code to solve for current under any specific conditions. The Newton-Raphson method follows Equation (II.20) for a function f(x)=0 (Faires and Burden, 1998).

$$p_{n+1} = p_n - \frac{f(p_n)}{f'(p_n)} \tag{II.20}$$

where p_n and p_{n+1} are the first and second approximations of the root and $f(p_n)$ and $f'(p_n)$ are the function and its derivative evaluated at p_n. Below the activation temperature (the point current begins to flow, 910K) of the fuel cell reaction, any values of heat generation are ignored. An example of heat generation for a 10 cm fuel cell is shown in Figure II.8 for both constant current and voltage.

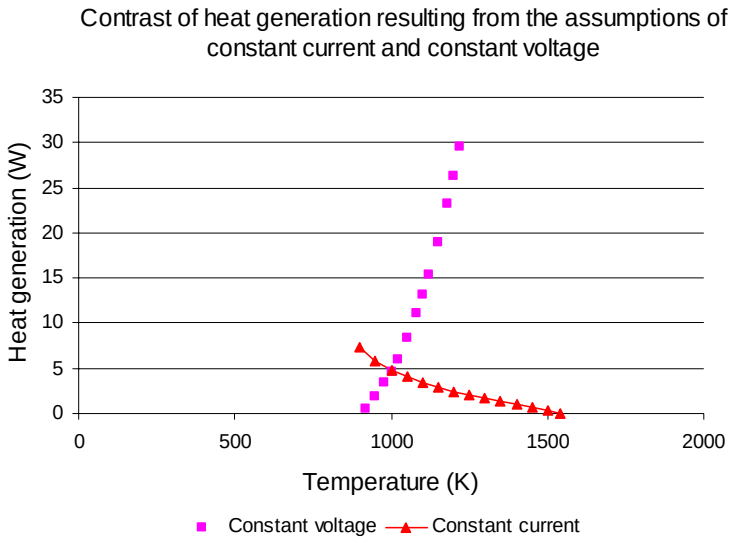

Figure II.8: The heat generation varies with temperature, as shown for a 4 x 4 array of square cells, 10 cm long with inlet fluid temperatures of 475K and an air flow rate of 7.24e-4 kg/s.

The constant voltage is a more realistic approximation than constant current because it reflects an initial heat generation of zero and an increasing heat generation as the current increases with increasing temperature. When the data for the conditions of Figure II.8 are inserted into the transient model, the affect of the two assumptions is more obvious. Figure II.9 shows the heat generation under transient conditions as determined by the finite difference code.

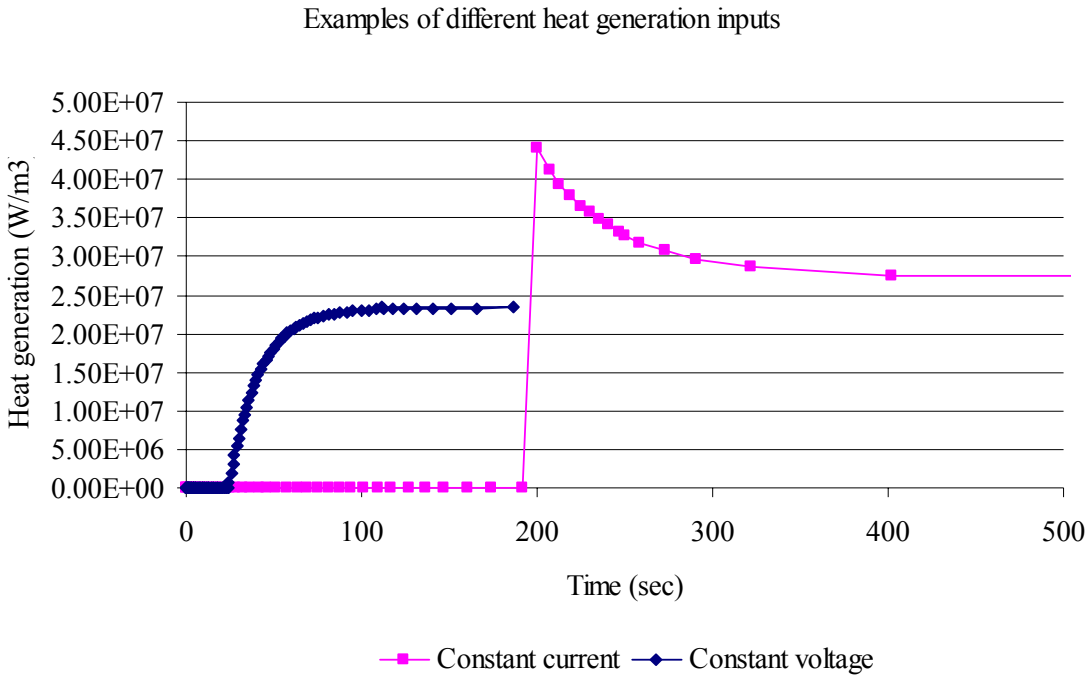

Figure II.9: The same case as Figure II.8, when solved by the finite difference code, shows the transient variation in heat generation.

Note that since the activation overpotential is dependent on current, the constant current calculations will have a different activation temperature. This requires the use of different input air or fuel temperatures, and in turn, reduces or increases the time shown in Figure II.9. Therefore, the salient conclusion of Figure II.9 is the lack of discontinuity in the heat generation when constant voltage is assumed.

II.6. Solution Techniques

II.6.1. Matrix form of governing equations

The governing equations can be expressed in the matrix form:

$$[A]\{x\} = \{b\} \tag{II.21}$$

The temperatures solutions of the nodes 1 through n fill the vector x. The vector b contains source terms. Some temperatures are set due to boundary conditions i.e. inlet air flow. The coefficients of these temperatures are grouped in the source column. Finally, the coefficients of each unknown temperature variable in the assembled governing equations fill the corresponding slots in matrix A. The equation for any element fills a row of matrix A. As a result of the connectivity of the elements, only the values for the center node and the 10 nodes in direct proximity to it may be non-zero. Thus, the assembled matrix, A, is sparsely populated, leading to wasted computer storage space for the zero entries. The matrix, A, can be decomposed into a non-zero coefficient matrix and a global node number matrix (Dempsey, 2002).

With transient analysis, the governing equations, representing one row of matrix A, are assembled for a general solid element in Equation (II.22) (similar to the one shown in Figure II.5).

$$\begin{aligned}
&-\left(\frac{A_8K_8}{|y_6-y_8|}\right)T_8^{s+1}-\left(\frac{A_5K_5}{|x_6-x_5|}\right)T_5^{s+1}-\left(\frac{A_7K_7}{|x_6-x_7|}\right)T_7^{s+1}-\left(\frac{A_{11}K_{11}}{|z_6-z_{11}|}\right)T_{11}^{s+1}-\left(\frac{A_1K_1}{|z_6-z_1|}\right)T_1^{s+1}\\
&-h(T_6^{s+1})A_{10}T_{10}^{s+1}-h(T_6^{s+1})A_9T_9^{s+1}+\sum_{\substack{i=1,5,7\\,8,11}}\left(\frac{A_iK_i}{|y_6-y_i|}\right)\cdot T_6^{s+1}+\sum_{i=9,10}h(T_6^{s+1})A_iT_6^{s+1}\\
&=Q(T_6^{s+1})V_6+\left(\rho c_p\frac{T_6^s}{\Delta t}\right)V_6
\end{aligned} \tag{II.22}$$

The subscripts in Equation (II.22) imply direction. For example, A_9 is the convection surface area in the direction of local coordinate 9. For a model with n nodes, the coefficients of the temperature terms of the equation above are stored in an n x 11 matrix. The global node number corresponding to T_1 through T_{11} is recorded in a second n x 11 matrix. When assembled, the equations can be solved iteratively. However, the coefficients of Equation (II.22) are temperature dependent; so, first, a programming scheme must be established to update the coefficients.

II.6.2. Programming flowchart

When applied to heat exchangers, only the exit temperature is used as a convergence parameter (Dempsey, 2002). The initial guess of exit temperature, based off of analytical heat exchanger solutions, is close enough to warrant only a few convergence loops for fluid properties. In contrast, the SOFC FD model has heat generation based on each individual electrolyte temperature. Since the heat generation function is highly non-linear, the code must be looped repeatedly until each element temperature converges. Initially, a guess is submitted for the exit fluid temperatures and the electrolyte temperature for the first iteration to calculate the initial values for the fluid convection coefficient and the heat generation. If the solution is steady state, the guess temperature for the exit fluid flows is the average of the inlet air and fuel flow temperatures. The guess temperature to calculate heat generation is 1000K (based on design goals of SOFC). For transient, the initial guess temperature of the electrolyte is room temperature because the structure should be reasonably close to room temperature at the end of the first time step. The guess for the fluid outlets is simply the same as the inlet, assuming minimal heat transfer in the first time step. The set of equations is then solved. The

resulting temperature solutions are used to recalculate fluid properties until the solution converges. The converged fluid properties solution is then used to recalculate the heat generation. The heat generation loop is then repeated until it converges. The fluid property loop and heat generation loop were performed sequentially because of the highly non-linear nature of the heat generation equation. Finally, this process is repeated for each time step, starting from room temperature. The transient model uses an explicit marching technique (Incropera and Dewitt, 1996). Figure II.10 illustrates the finite difference model solution technique.

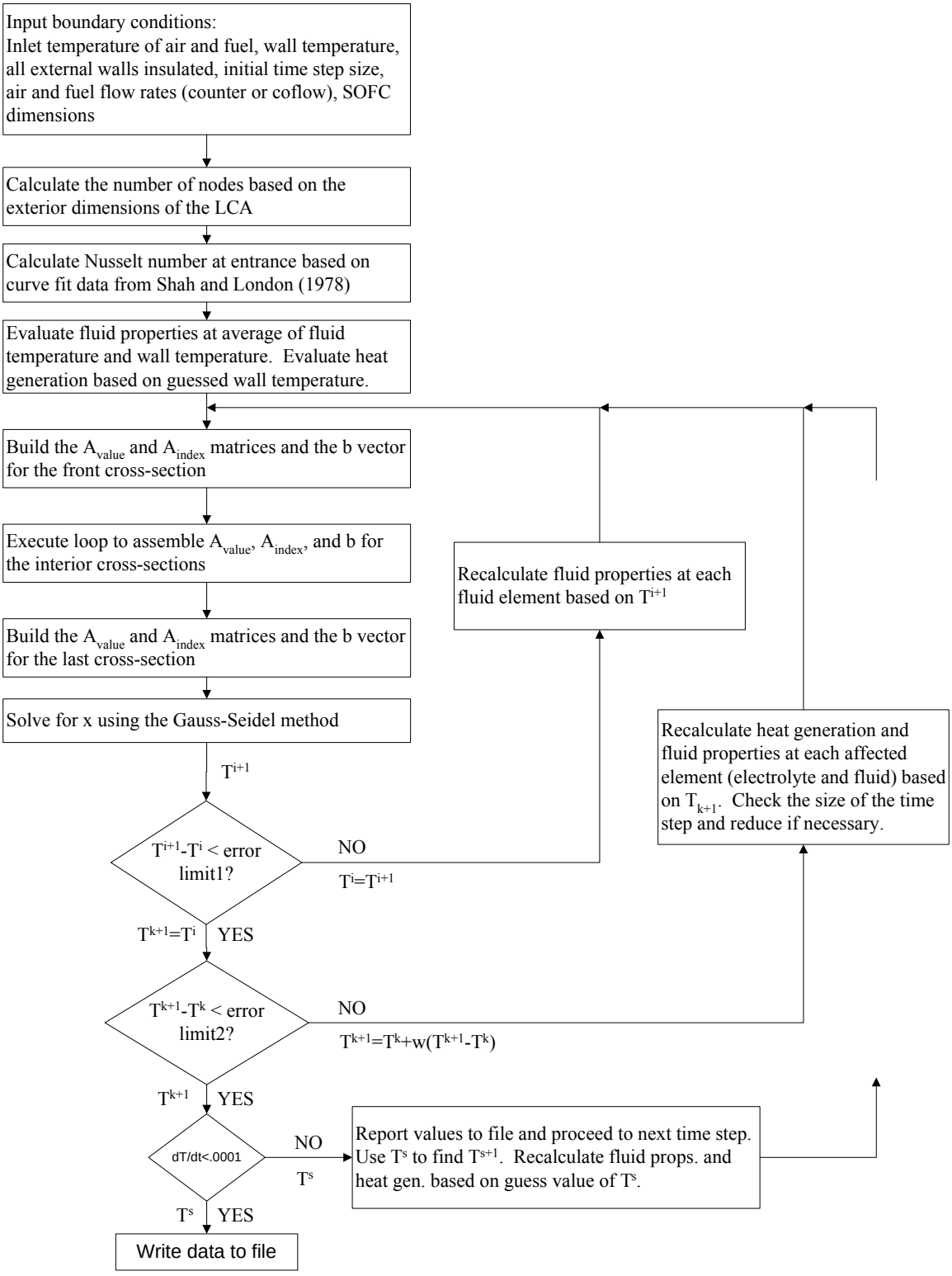

Figure II.10: The input temperatures for a prior time step initiate a series of loops to converge on the temperature solutions for the next time step. The looping procedure is based on prior work by Dempsey (Dempsey, 2002).

II.6.3. Iterative technique

An iterative approach is used to solve the set of equations, since the alternative decomposition methods do not apply to the modified storage matrix. In addition, iterative methods have a significant computational time advantage over LU decomposition approach (Dempsey, 2002). Originally, an SOR (successive over-relaxation) method was used. However, in testing the loops for convergence, over-relaxing the solution was found to diverge with the implementation of counterflow.

II.7. Convergence of solution techniques

II.7.1. Convergence of the iterative method used in the solver

The SOR method used by Dempsey had to be revised to analyze counterflow. For all conditions tested, steady state or transient, the counter-flow solution requires many more iterations than concurrent-flow. The problem is the directional bias of the Gauss-Seidel/SOR method. Unlike the Jacobi, the Gauss-Seidel and SOR update variables as they solve. In general, updating the matrix greatly increases the convergence speed (Faires and Burden, 1998). As the solver progresses forward, each equation solved is based on more updated data. If the nodes are numbered in the order of the geometry, the solution will have a directional bias (Meurant, 1999). The SOR method follows the basic form (Faires and Burden, 1998)

$$T(i)_{n+1}{}' = T(i)_n + \omega\left(T(i)_{n+1} - T(i)_n\right) \tag{II.23}$$

The parameter ω is a weighting value which increases the rate of convergence. For $1<\omega<2$, the residual, $T(i)_{n+1} - T(i)_n$, is increased. For this method to converge faster, the

iteration must already be moving toward the solution. However, in counterflow, the directional bias of the iterative technique is moving counter to the flow (mass transport) of one of the fluids. Without extremely close guesses for temperatures down the entire length of the opposing fluid channel, the first m iterations will likely diverge from the true solution. The SOR method amplifies this divergence. Figures II.11 and II.12 show the spike in temperature values in both the SOR and Gauss Seidel iterative procedures for a steady state example.

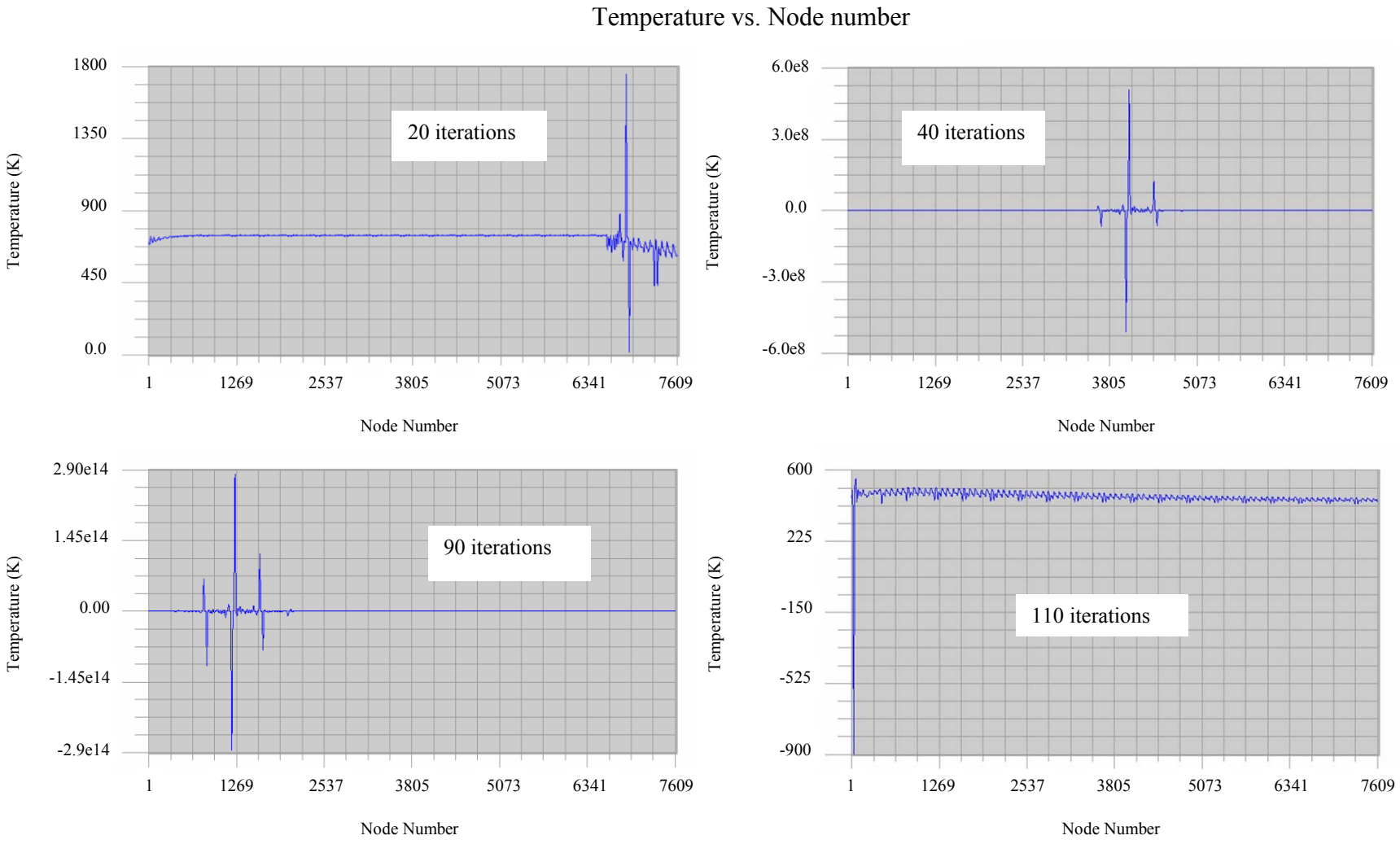

Figure II.11: The SOR method is shown to diverge for the counter-flow steady state temperature solution of a 4x4 unit cell, 0.86x0.86x10cm with 7.24e-4kg/s air flow (m=94).

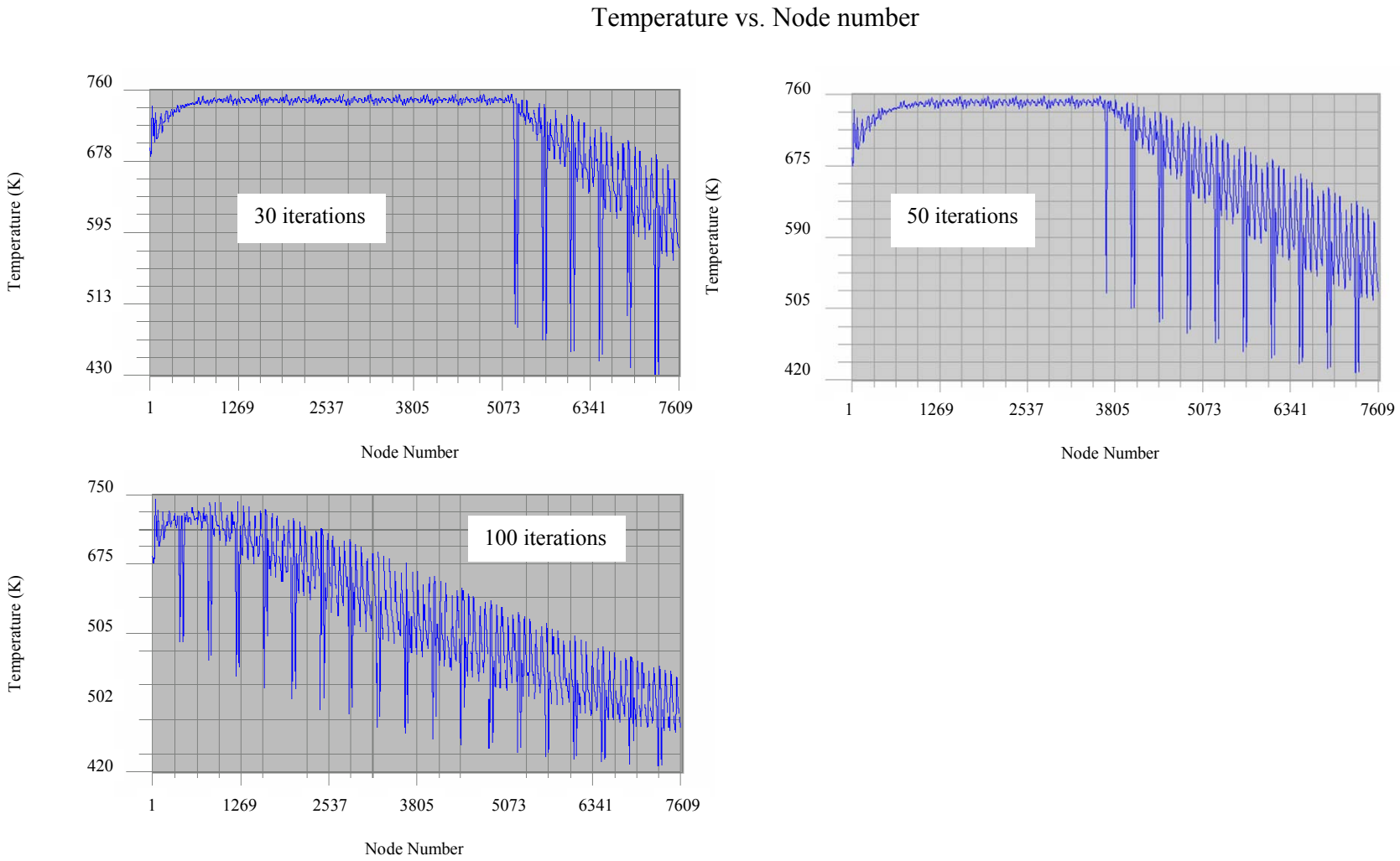

Figure II.12: Gauss Seidel iteration of SOFC shown to converge for the counter-flow steady state temperature solution of a 4x4 unit cell, 0.86x0.86x10cm with 7.24e-4kg/s air flow (m=94).

II.7.2. Convergence of the heat generation loop

The convergence of the solver does not guarantee convergence of all iterative loops. They must be evaluated individually. The convection coefficient loop inserts the newly calculated convection coefficient back into the solver. The heat generation could not be iterated in this way. The heat generation formula is exponential. Recall that Figure 2.8 showed that heat generation assuming constant current trended downward with increasing temperature while assuming constant operating voltage resulted in an upward trend. To insure the best convergence, the two heat generation terms are analyzed separately.

II.7.2.1. Convergence of heat generation loop assuming constant current

In the case of constant current, the only way to keep the solution from diverging is to under-relax the change in temperature between iterations. The equation used is the same as Equation (II.23), except, $0 < \omega < 1$. Under-relaxation is often used as an alternative to straight Gauss-Seidel iteration when the solution will not converge (Chapra and Canale, 1998). Oscillations or divergent trends can be damped out by use of under-relaxation. The oscillating effect of the exponential heat generation is present regardless of geometry or input conditions because it depends on the heat generation function itself. The easiest way to show the affect of under-relaxation is by empirical results. Figure II.13 shows the convergence of the heat generation loop for different values of ω and two different flow rates.

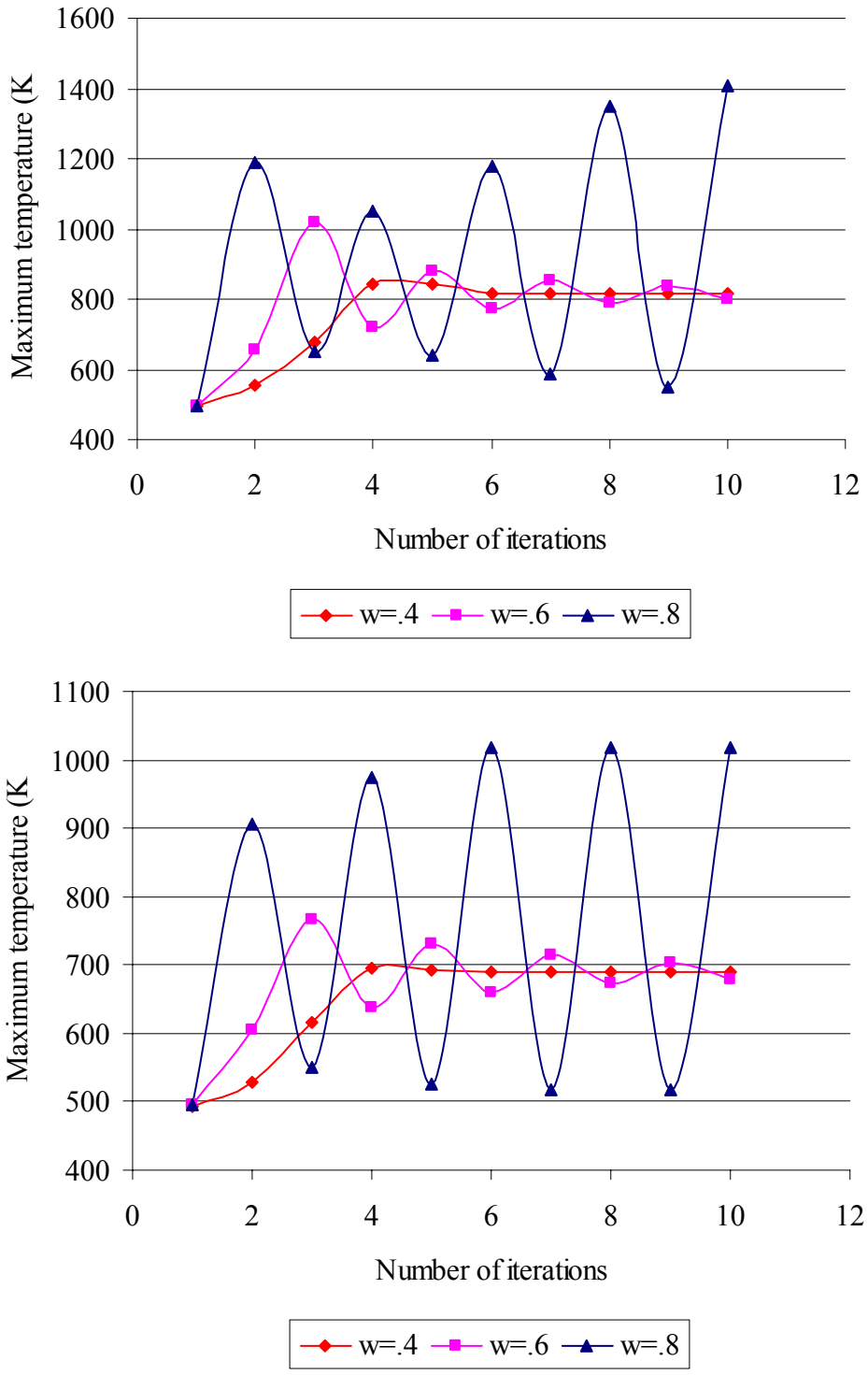

Figure II.13: Convergence of the heat generation loop for constant current. Cases with flows of 7.24e-4 (bottom) and 7.24e-6 (top) are shown for a 4x4 SOFC, with dimensions 0.86x0.86x10cm, inlet fluid temperatures of 475K and initial wall temperature guess of 1000K. A low temperature cutoff for the fuel cell reaction was not applied in these examples (making possible heat generation below 900K).

The convergence of the maximum temperature indicates overall convergence for the cases tested. Values near 0.8 caused divergence. The solution converges fastest with a value for ω near 0.4. The results of Figure II.13 were validated by many more cases, including cases with a lower temperature bound for the onset of the chemical reaction. The best weighting parameter was always 0.4.

II.7.2.2. Convergence of heat generation loop assuming constant operating voltage

The convergence of the FD code was also tested after the heat generation formula was altered to reflect changes in current assuming a specified operating voltage. The results, illustrated in Figure II.14, were the opposite of the constant current case.

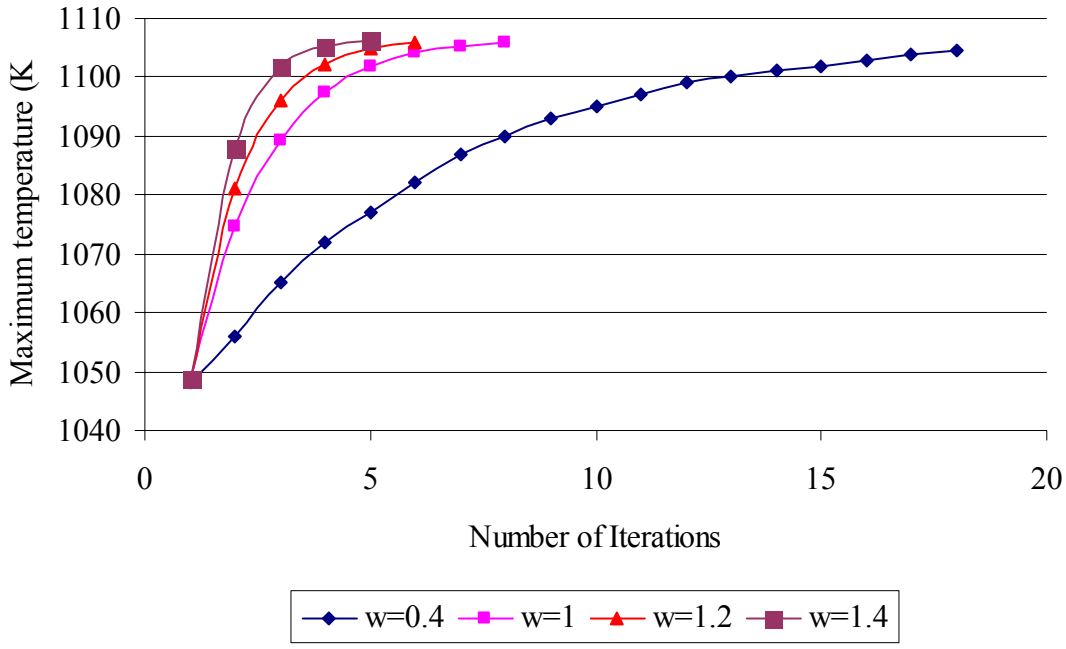

Figure II.14: Convergence of the heat generation loop for variable current assuming constant operating voltage. The Cases shown has inlet air flow of 7.24e-5, with dimensions 0.86x0.86x10cm, inlet air temperature of 980K, inlet fuel temperature of 475K, and initial wall temperature guess of 1000K. A low temperature cutoff of 910K was used to simulate the onset of the chemical reaction.

For the variable current models, a weighting parameter of 1.4 was used to encourage convergence towards the true solution. The relatively high weighting parameter could possibly lead to oscillation if the initial wall temperature guess is poor. The model was solved for a range of guesses for the same case as Figure II.14 to ensure stability. The iteration converged for all cases tested with no signs of oscillation.

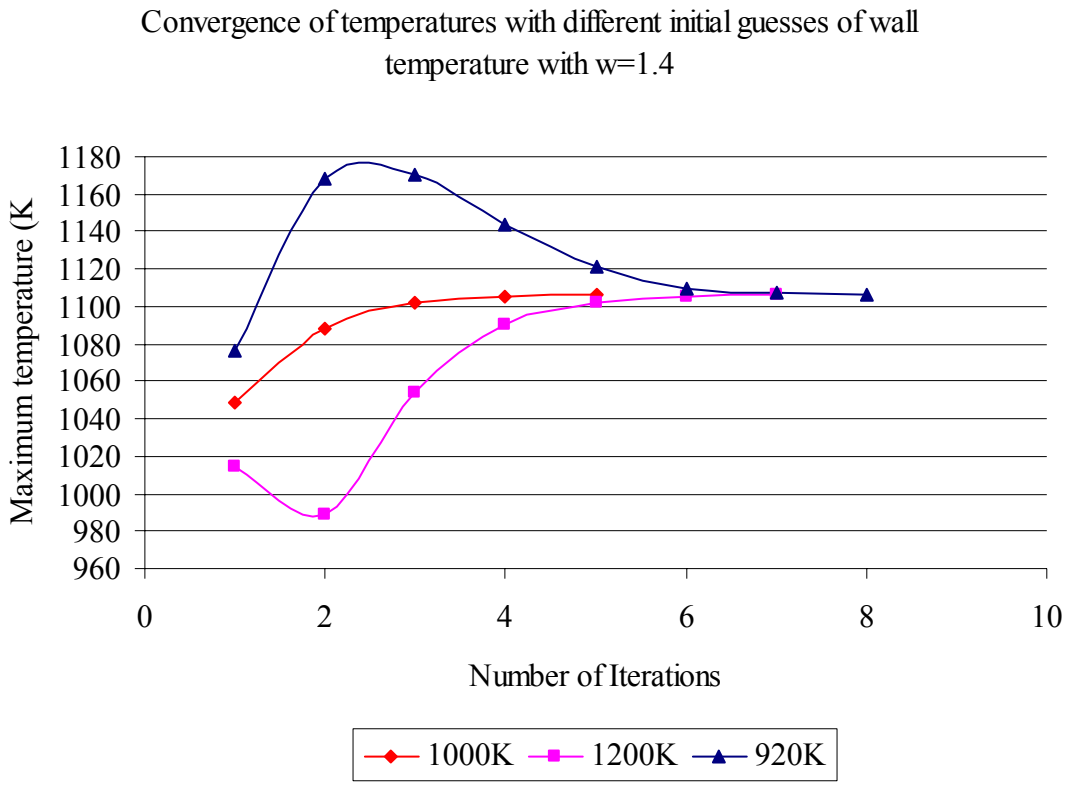

Figure II.15: Using ω=0.4 and the same setup as Figure II.14, different initial guesses were tested to insure convergence.

II.7.3. Convergence of the transient solution to the steady state

The last loop added to the program was the time loop. Since an implicit scheme was already established to solve for the steady state temperatures, a simple marching technique was used to solve the set of equations at each time t + Δt. The implicit method with the marching solution is usually unconditionally stable (Incropera and Dewitt,

1996). However, the non-linearity of the heat generation in the finite difference code causes instability if the time segment is too large. The easiest way to prove that the solution is accurate is to do a convergence study with several different time increments. Figure II.16 shows the results of a time study on a 4x4, 3cm long fuel cell.

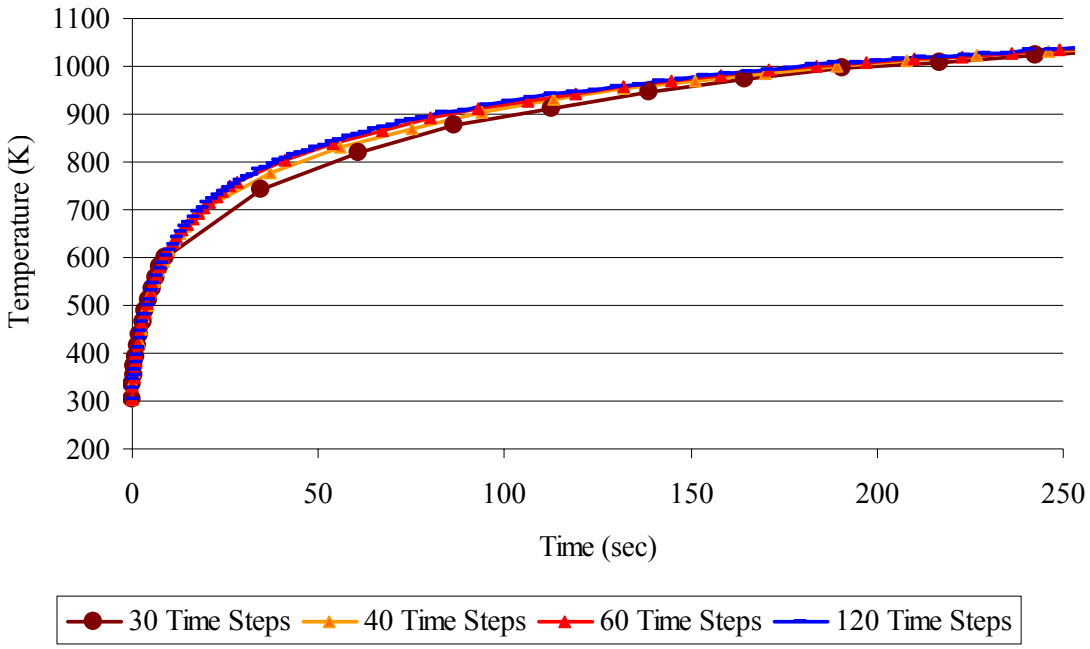

Figure II.16: An example of the effect of time step size on average fuel cell temperature for a 4x4 (0.86cm x 0.86cm x 3cm) YSZ-$Fe_{39}Ni_8Cr$ fuel cell with 300K inlet fuel and air, 2e-7kg/sec air flow and 2.784e-8kg/sec fuel flow. The time steps were linear above 10 sec and exponentially weighted below (constant current is used).

The rate of temperature change during startup depends on many factors including inlet fluid temperature, flow rate, geometry, stacking etc… Also, the heat generation equation is constantly evolving. Figure 2.16 assumed heat generation at room temperature at a rate consistent with constant current assumption, resulting in a worst case scenario with unreasonably rapid startup. When the heat generation equation was

changed to constant operating voltage, the change was dramatic. To be robust, the time step size must adjust independent of these factors.

Assuming a very small initial time step ($5x10^{-5}$ sec), the size of the subsequent time steps can be iterated based off of an assigned upper and lower limit of temperature change for a given time step. With a guessed value of Δt, provided by the previous step, the time loop is solved once, producing a rough value of the rate of temperature increase. The rate of temperature increase can be used to linearly estimate the time step size necessary to result in an acceptable temperature change. Several different models varying in length from 3cm to 10cm and air flow from 7.24e-4 kg/s air to 2e-7 kg/s (two large factors in heat generation) were tested for convergence. Figure II.17 compares the convergence of the self-adjusting time steps and the exponential time steps like the ones used in Figure II.16.

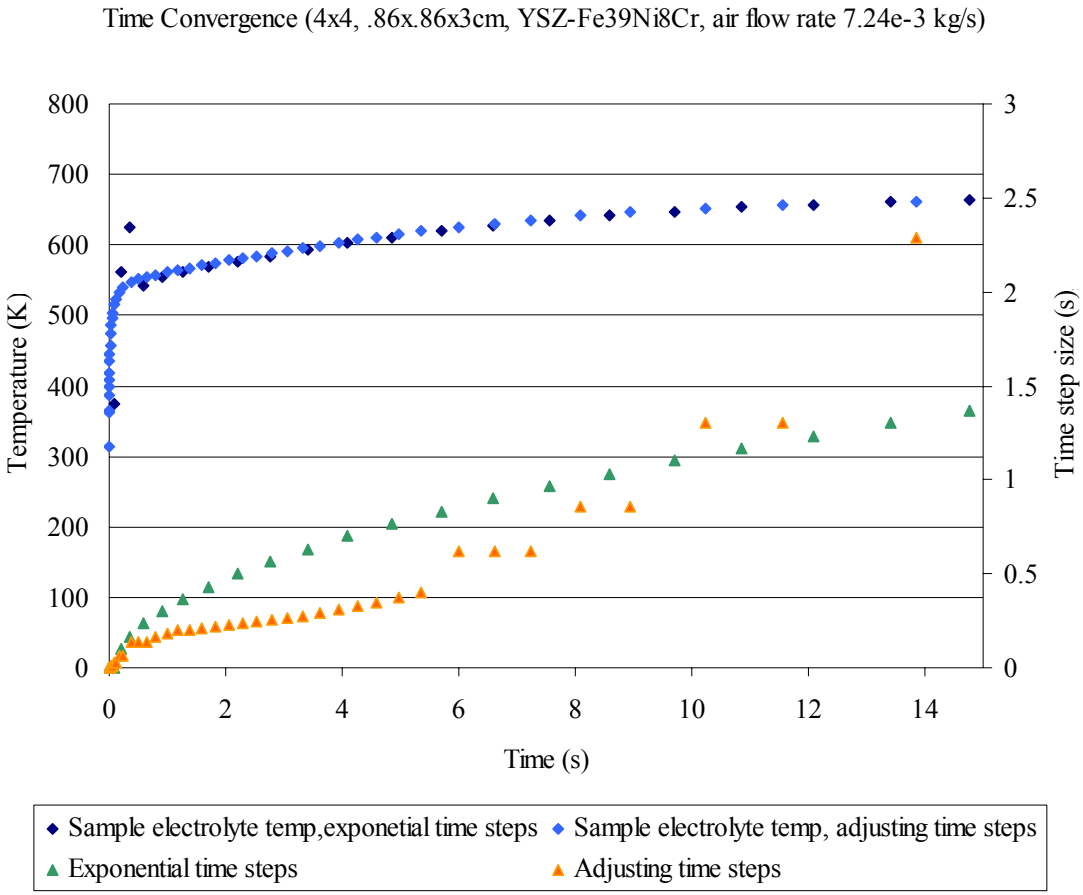

Figure II.17: For the worst case scenario of Figure II-12, the adjusting time steps converged better and with less iteration when brought to steady state. Both converged on the steady state solution.

Note that for the case described by Figure II.17, the exponentially distributed time steps did not converge properly for the electrolyte at 0.5 seconds. Although the rapid increase in temperature in this example was useful to test time step convergence, such an increase would most likely correspond to unacceptable levels of thermal shock.

II.8. Parameterization capability of the finite difference code in modeling hybrid SOFC's

II.8.1. Acceptable solid geometries

Since the motivation of this study is to efficiently perform preliminary hybrid SOFC design, the capability of the code to simulate different geometries must be demonstrated. User geometry inputs of the code include: wall thickness in x and y, channel width and height, overall width and height of structure, and length. Wall thicknesses and channel dimensions can be graded in size along the x or y direction, but the channels must still align vertically and horizontally. In other words, all the channels in a column must have the same width, and all the channels in a row must have the same height etc… Figure II.18 gives several examples of variations in geometry which can be simulated by the FD code.

In addition, thermal conductivity and heat capacitance for the specific materials must be supplied. Only hybrid geometry is acceptable as shown in Figure I.4. The materials must alternate, beginning and ending with an interconnect layer. The division of the material must also occur at the midpoint of the vertical channel walls.

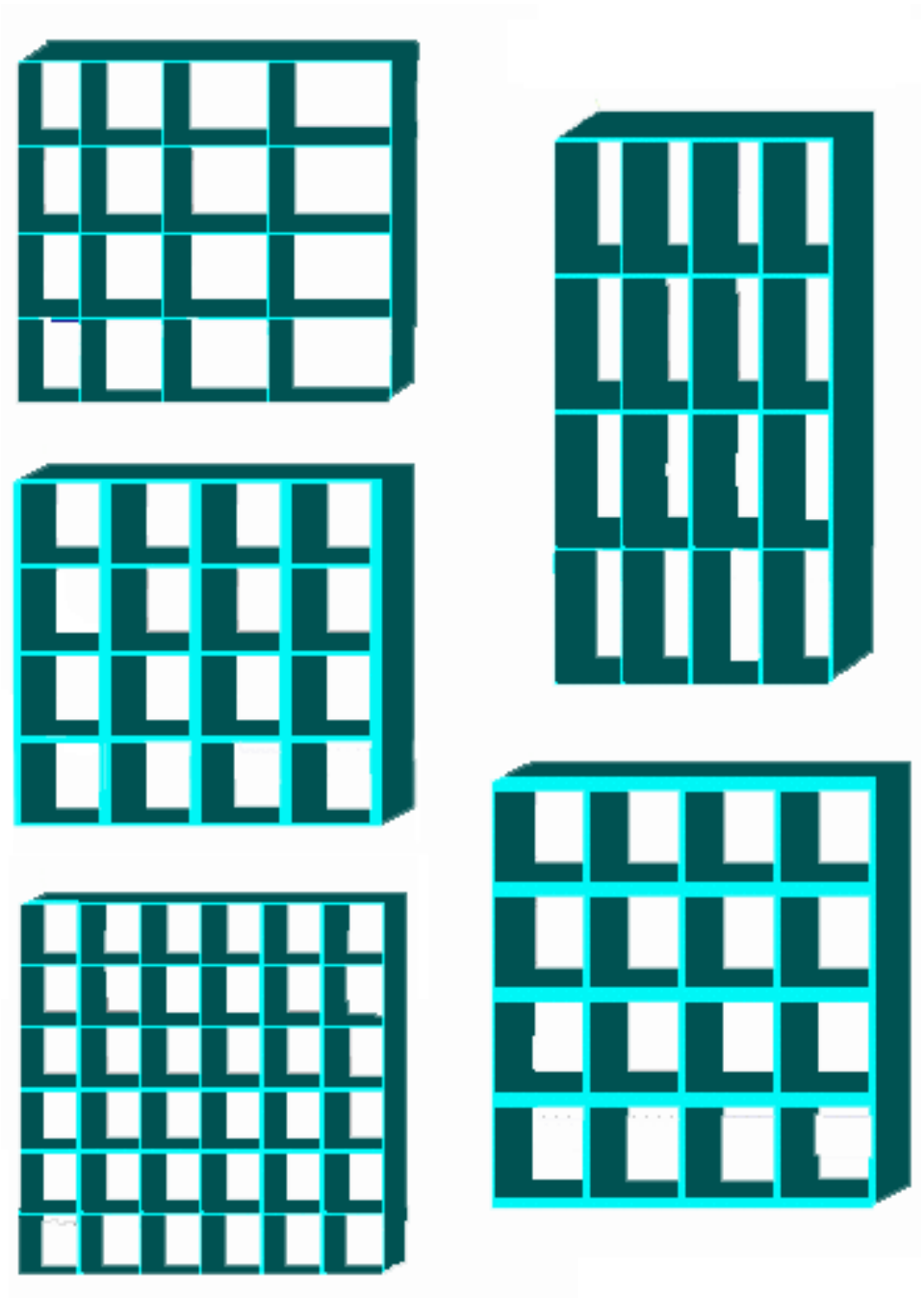

Figure II.18: The FD code can solve for the transient temperature distribution in a large range of rectangular celled geometries. Not shown is the ability to model unit cells stacked vertically.

II.8.2. Acceptable fluid conditions

For the FD code to be valid, the flow must be fully developed, laminar flow. Outside of this restriction, the flow rate of hydrogen and air, as well as the inlet temperatures, may be altered independently of one another. The start-up schedule may also be altered as needed since the convergence of the transient solution adjusts depending on the current heating rate. Furthermore, the convergence of the transient code is very stable for a range of heat generation considerations as demonstrated by the convergence of both constant current and constant voltage heat generation. Therefore, any future refinement of the heat generation formula would require only changing the heat generation subroutine without regard to the convergence of the transient solution.

II.8.3. Considerations in parameterization of hybrid SOFC design

In the future, the finite difference code may be used to aid in the optimization of fuel cell design. However, hybrid SOFC design is complex due to the interdependence of electro-chemistry, thermodynamics, and mechanics. Any one of these broad consideration can not be changed without altering the others. To demonstrate the capability of the FD code, several hybrid SOFC temperature distributions will be calculated for different SOFC lengths. However, by varying one dimension, the heat generation, total convection, total conduction and power generation will all be altered although the fluid flow remains the same for all lengths. Four different lengths were chosen, 3cm, 6cm, 9cm and 10cm. The inlet air temperature was 980K and the inlet fuel was 300K. Air flow was 6.24×10^{-5} kg/s and fuel flow was 2.784×10^{-8} kg/s. The cross-sectional dimensions were 0.86x0.86 cm with a 4x4 array of cells (making the walls 120μm thick). The results are given in Figure II.19 and Figure II.20.

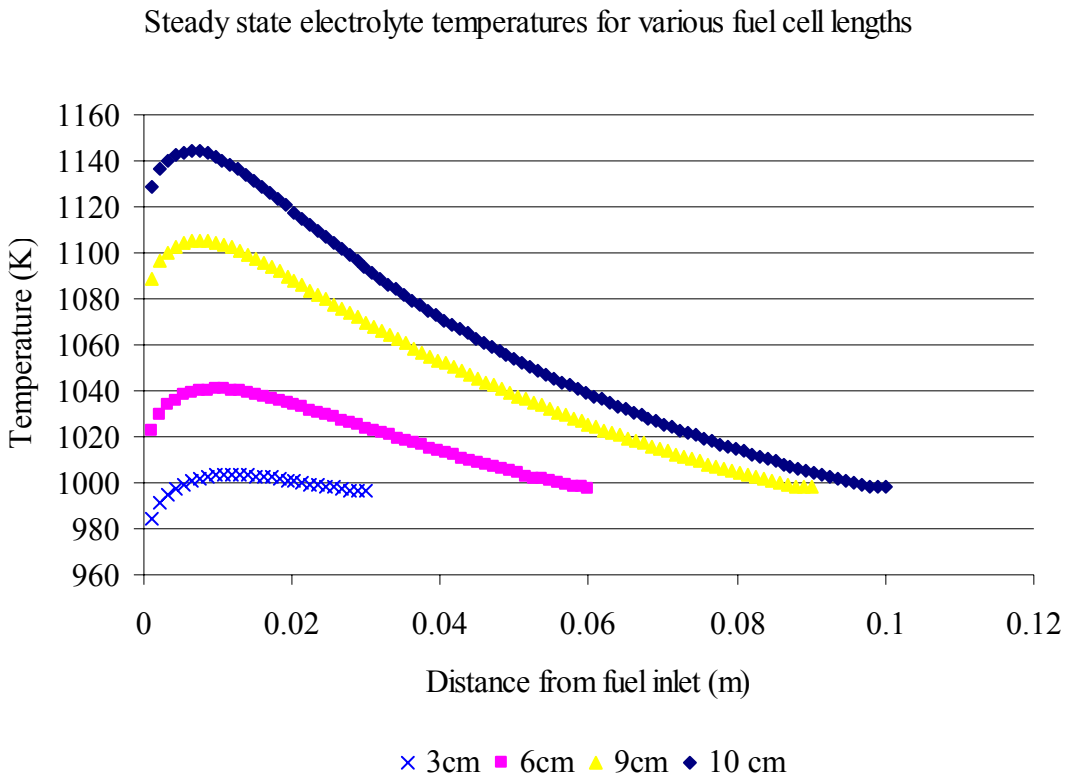

Figure II.19: The length of the fuel cell was varied from 3cm to 10cm. As expected, the steady state temperature increases in the electrolyte with longer fuel cells, but also, the gradient becomes more severe from front to back.

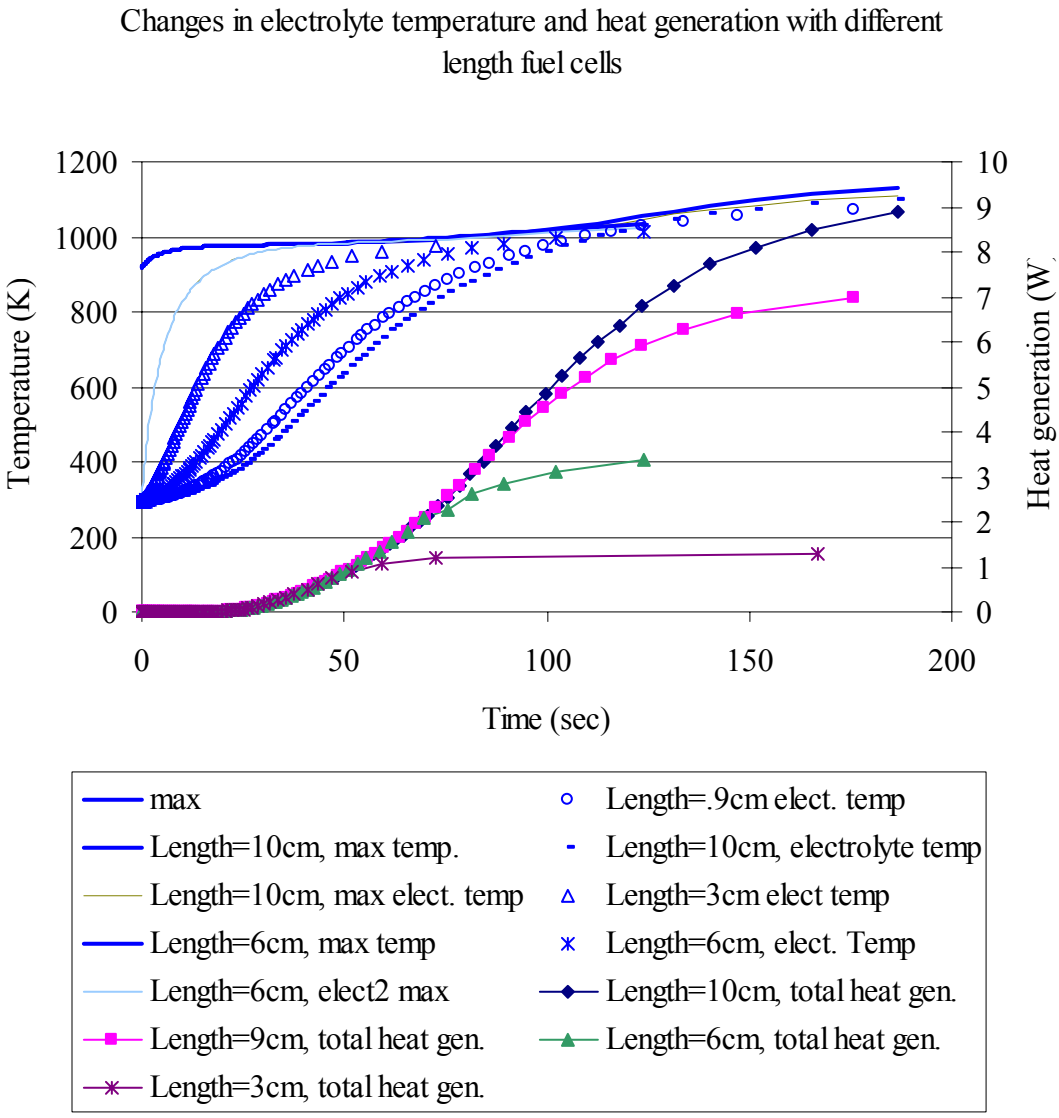

Figure II.20: Transient results show the 3cm SOFC heats up much faster than the longer fuel cells by convection, but the heat generation starting at 25 seconds is less. Eventually, the longer fuel cells become hotter.

In addition, under the assumption of a slow fuel flow rate and fast air flow, the temperature follows a certain pattern, demonstrated by example in Figure II.20, because of the counterflow conditions.

II.9. Validation of finite difference results

Two main sources of error can affect the accuracy of the finite difference results. First, the numerical method used in solving the set of equations may be improperly applied or not fully converged. Secondly, the assumptions made in formulating the finite difference method may not be accurate. The accuracy and convergence of the Gauss-Seidel method, as well as the loops built around it, may be validated by a series of convergence analyses and an exact solution provided by decomposition. To validate the assumptions and formulation of the finite difference equations, results for a number of representative cases will be compared with FLUENT simulations. Although neither model is validated by experimentation or operation of a prototype fuel cell, the accuracy of the integration techniques, refined meshing capability, and detail of the equations used in FLUENT make it a reliable source for comparison.

II.9.1. Validation of solution techniques

The iterative procedure, Figure II.10, used to solve the set of equations (Ax=b) is fundamentally a Gauss-Seidel iteration. The exact solution is obtainable through LU decomposition. A program was written in FORTRAN as a subroutine to recombine the location matrix and coefficient matrix into the standard form Ax=b and solve by LU decomposition. Decomposition, forward and backward substitution to solve for x were

programmed following referenced equations (Faires and Burden, 1998). When implemented, decomposition required much more memory and time than iterative techniques, similar to the findings of Dempsey (2002). Therefore, the whole program could not be executed using the decomposition method. Each loop or property variation would require a new decomposition solution. The best approach was to run the FD program using iterative techniques and evaluate the final set of equations by decomposition. The decomposition results can then be compared to the iterative solution. Several 4 x 4 simulations were checked by decomposition. The results were regularly within 0.02% of the exact solution when the error in the iterative solver was set to 0.0013K. Any higher of a value resulted in appreciable error.

The possibility of error also exists in loop error and FD mesh size. Since the time solution is explicit, the time step size will be used to verify transient convergence. The DO loops for the heat generation term and the fluid properties are a part of the implicit solution. They have a conditional statement that ends the loop when the maximum error in temperature between loops is below a specified value. The error specified in these two loops adds directly to the error in the solver loop. In general, the error in the heat generation loop is kept below 5K and the error in the convection loop is below 1K. The error value is computed as the maximum degrees K difference between loops for any node. The extra time needed to converge the maximum temperature the remaining few degrees K in the heat generation loop was much greater than the benefit from a slightly more accurate solution.

Finally, the mesh size may be a source of error. Unfortunately, the mesh in the x-y plane may not be changed without altering the fundamental element shapes of the FD

code. However, the depth of the elements is easily changed. Figure II.21 demonstrates that the SOFC temperature distribution is not very sensitive to the number of elements along the length of the fuel cell.

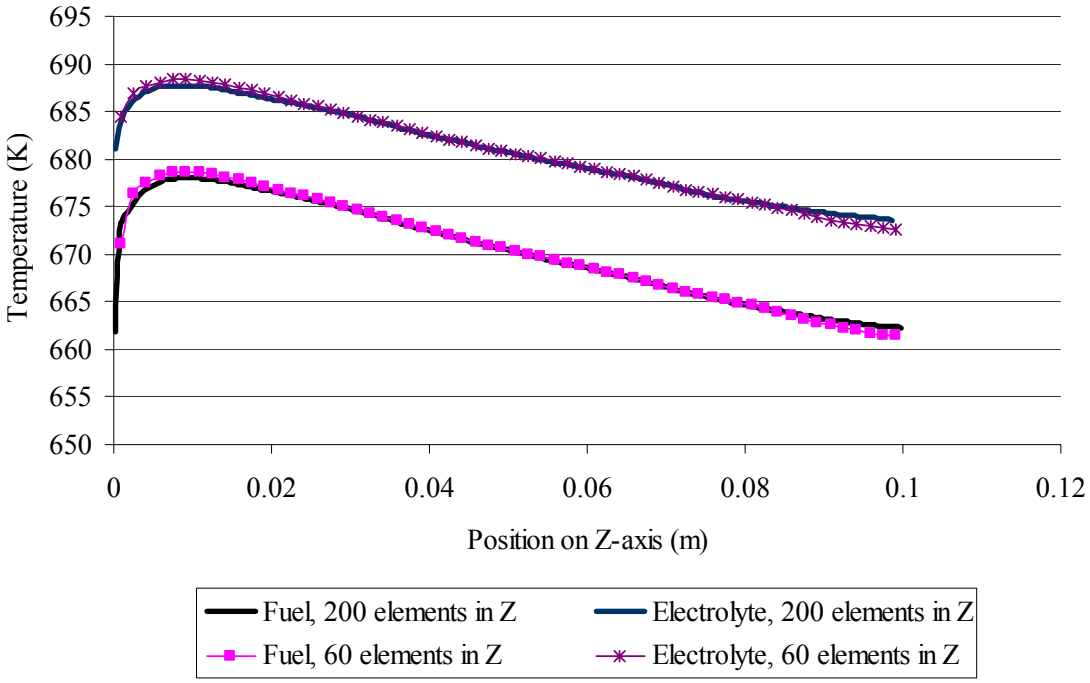

Figure II.21: The FD code has similar results for a range of element depths. The model displayed is for a steady state, 4x4 (.86x.86cm), 10cm long, 7.24e-4kg/s air, with fuel/air inlet temperature of 475K. Note that the convergence of the selected nodes was indicative of entire structure.

II.9.2. Validation of finite difference formulation

Since a functioning prototype has not yet been manufactured, the validation of the finite difference code ultimately relied on FEM software. Two general cases were analyzed. First, a heat exchanger case was examined with all heat generation terms set to zero and the air and fuel channels at different inlet temperatures. This scenario tests the convection and conduction between the fluid and solid. In prior work by Dempsey, the

heat source was a constant temperature located on the top surface (2002). Therefore, heat gradients were primarily in the x-y plane. In this case, heat gradients occur in the x, y, and z directions. Once the heat exchanger model was tested, the heat generation of the fuel cell problem was added. A fuel cell model was also created in FLUENT by Dempsey (Dempsey, pers. com., 2004). All models were checked by the second law of thermodynamics by performing an energy balance on the fluid inlets and outlets.

II.9.2.1. No generation case

Validating the simpler case of no generation in the electrolyte is important because it separates errors due to conduction and convection from errors that may be caused later when including very large heat generation. The inlet conditions were fuel at 1000K and air at 300K. The air flow rate was significantly faster than the fuel (7.24×10^{-4} kg/s air and 2.784×10^{-9} kg/s fuel). Both the finite difference code and FLUENT were used to evaluate the no generation case. FLUENT incorporated two main assumptions. All fluid element properties in FLUENT, regardless of elemental temperature, were evaluated at room temperature, and velocity variations in the channel were determined by density changes according to ideal gas behavior. The finite difference code was used to verify that neither of these approximations significantly altered the results as compared to the tabulated pressure or temperature dependent fluid properties normally assumed in the finite difference code. The finite difference results were relatively insensitive to variations in fluid properties and the ideal gas behavior matched the tabulated density values. A symmetry assumption was also made to minimize run time. A 4x1 column was modeled instead of the entire 4x4 structure. Since the left and right walls are adiabatic,

symmetry does exist. Ideally, the 4x4 structure would be quarter-symmetric, but the walls in the middle are the same thickness as the outer walls. Therefore, the first vertical plane of symmetry divides the middle wall in half. The resulting 4x2 model does not have another plane of symmetry. A truly quarter-symmetric honeycomb would have double thickness for the interior three walls. In the end, the slight asymmetry was ignored in the interest of increasing computational efficiency. Moreover, the asymmetry in the finite difference code (which assumes no symmetry) was constantly checked to make sure the error in assuming symmetry was minor. Figure II.22 compares the output of FLUENT and the finite difference code for the no generation case.

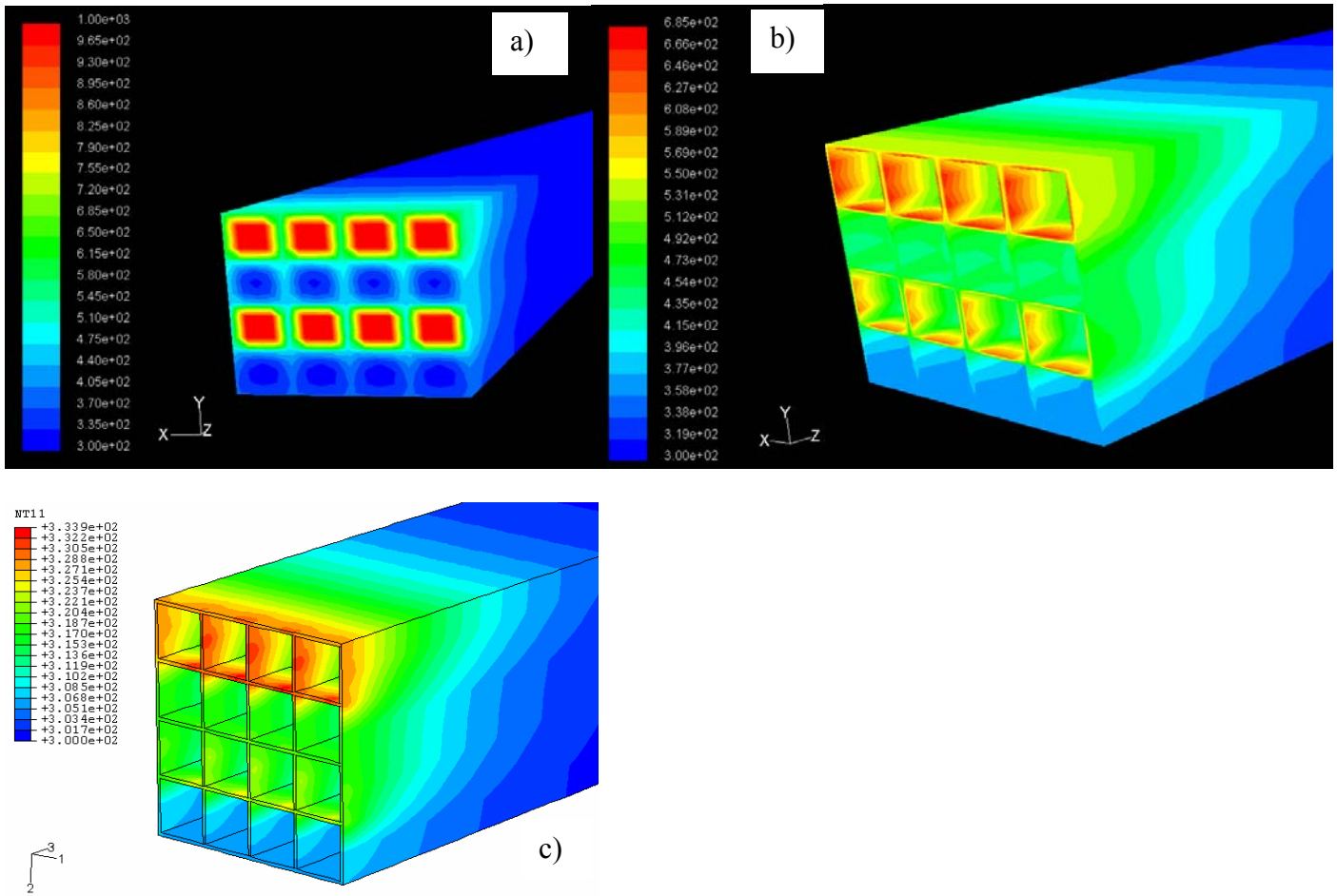

Figure II.22: A 10cm long heat exchanger problem with no heat generation, 1000K inlet fuel at low flow rate and 300K inlet air at high flow rate was evaluated with a) FLUENT (fluid and wall temperatures shown), b) FLUENT (only wall temperatures), and c) the FD code.

Figure II.22 demonstrates the difficulty in comparing FLUENT and the finite difference code. Although the temperatures shown in Figure II.22 c were linearly distributed to the whole model, they are still based off of average temperatures over an element in the finite difference mesh. On the other hand, the temperatures of FLUENT are evaluated over much smaller elements. Thus, fine gradients will show up, resulting in much higher peak temperatures in FLUENT. Specifically, the maximum temperature of the finite difference code is 51% lower than FLUENT, but only 44% lower than the corresponding average temperature in FLUENT. Also, from Figure II.22, although the magnitude is far off, the behavior of the heat transfer is identical. Both models show the wall temperature first deviating from 300K at exactly 2.3cm from the front face, and, obviously, the contours follow each other closely.

The mean fluid exit temperatures may be further corroborated by the use of the second law of thermodynamics. The heat transfer, in this case, from the fuel to the air is complete because the exit temperature of the fuel is the same as the inlet temperature of the air (Hodge and Taylor, 1999). The exit temperature of the air can be found by (Hodge and Taylor, 1999)

$$\dot{m}_{air} c_{p\,air} \left(T_{exita} - T_{inleta} \right) = \dot{m}_{fuel} c_{p\,fuel} \left(T_{exitf} - T_{inletf} \right) \tag{II.24}$$

where $\dot{m}_{air}$ and $\dot{m}_{fuel}$ are the mass flow rates of air and fuel, c_{pair} and c_{pfuel} are the heat capacity of the air and fuel, T_{exita} and T_{exitf} are the exit temperatures of the air and fuel, and T_{inleta} and T_{inletf} are the entrance temperatures of the air and fuel.

This equation is valid since all external walls are insulted, and the only heat transfer is occurring between the two fluids. According to Equation (II.24), the mean outlet air temperature is 303.85K. The corresponding mean outlet temperature of the

finite difference code is 303.84K while FLUENT yields a mean of 340K. The fuel was going to slow as to not measurably affect the total heat transferred. These results raise the possibility that FLUENT may overstate temperatures with low flow rates. Certainly, the finite difference code will not resolve temperature spikes if they occur in an extremely small area, such as the wall surface as shown in Figure II.22 b.

Finite difference code results vs. FLUENT analysis

FLUENT is utilized in work by Dempsey (pers. com., 2004) to judge the electronic performance of the hybrid fuel cell. Of the cases modeled by Dempsey, three were analyzed in depth. All cases had 0.2 cm square channels and 0.012 cm thick walls. They were modeled assuming constant current distribution. Fuel mass flow rate was fixed at 6.96e-9 kg/sec per column. All initial models, Case 1 through Case 16, were steady state solutions using a constant current assumption in evaluating heat generation. The distinguishing attributes of several cases, as well as the FLUENT results, are listed in Table II.3 and Table II.4.

Table II.3: Inputs used for test cases performed by FLUENT and finite difference.

Case	Cell array size	Length (cm)	Air inlet T (K)	Fuel inlet T (K)	Air mass flow rate per column (kg/s)
Case 1	4 x 4	3	475	475	5e-8
Case 6	8 x 4	10	300	300	5e-8
Case 10	4 x 4	10	475	300	1.81e-4

Table II.4: FLUENT results for comparison with finite difference approximations.

Case	Power (W)	Heat generated (W)	Avg air outlet Temp. (K)	Avg fuel outlet Temp. (K)	Avg electrolyte Temp. (K)
Case 1	0	2.92	729.10	876.55	850
Case 6	13.01	5.498	837.57	1167.62	1165.8
Case 10	0	48.55	530	615	656.5

The same three cases were evaluated using the finite difference code, with mixed results. The finite difference code was in excellent agreement for Case 10, but greatly differed for Case 1 and Case 6. For Case 10, the heat generation for the finite difference code was 44.21W, within 9% of FLUENT results. A 9% variation in heat generated only corresponds to a few degrees K, since the heat generation function changes greatly in this temperature range. The temperatures output of FLUENT and the FD code are shown in Figure II.23.

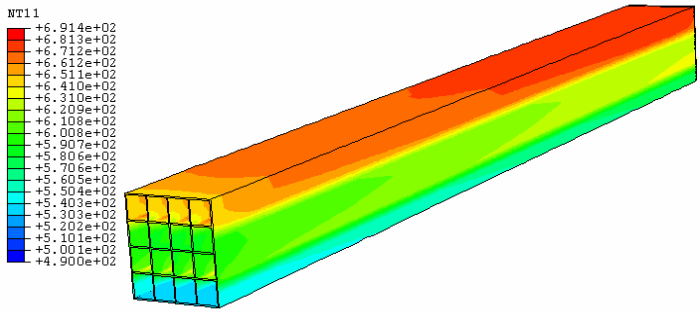

a)

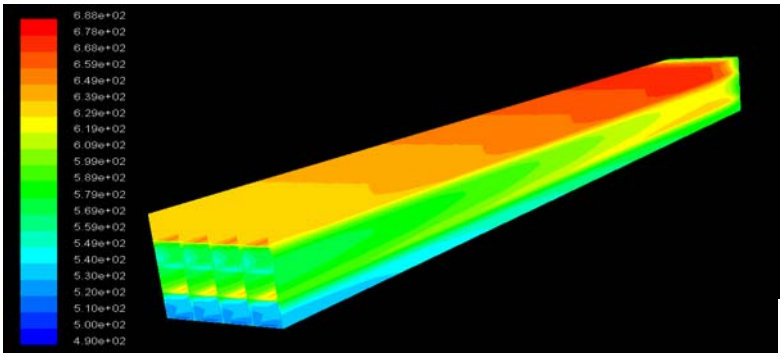

b)

Figure II.23: a) Finite difference and b) FLUENT temperature profiles for Case 10 at steady state.

The temperatures for the finite difference code match, very well for Case 10, the temperature field of FLUENT. However, Case 1 and Case 6 did not. Once again, Equation (II.24) can be used to check the heat generation total against the heat dissipation possible by energy conservation given the inlet and outlet gas temperatures and the gas flow rates.

Table II.5: An energy balance approach for comparing FLUENT and finite difference heat generation with the convective heat dissipation signified by a change in fluid temperatures.

Case	FLUENT			FD Code		
	Avg. Electr. Temp (K)	Heat generated (W)	Heat convected out (W)	Avg. Electr. Temp (K)	Heat generated (W)	Heat convected out (W)
Case 1	850	2.92	0.4	1246	0.61	0.61
Case 6	1165.8	5.498	0.7	1443	1.29	1.27
Case 10	656.5	48.55	42.3	667	44.31	43.8

The FLUENT model for Case 1 and Case 6 are not corroborated by the conservation of energy. Both models conform relatively well to the conservation of energy for Case 10. Note that the slight discrepancy in heat generated versus convected for the FD code is most likely due to the use of average heat capacity in calculating the value for heat convected out. The inputs from Table II.3 and the results from Table II.5 suggest that the FLUENT model may not be correct for low flow rates. The flow rates of the air and fuel for the original cases were reduced and compared to the FD code. Table II.6 and Table II.7 show these results.

Table II.6: Variations in inputs to test the influence of flow rates on results.

Case	Cell array size	Length (cm)	Air inlet T (K)	Fuel inlet T (K)	Air mass flow rate per column (kg/s)	Fuel mass flow rate per column (kg/s)
Case 6b	8 x 4	10	475	475	5e-6	6.96e-7
Case 6c	8 x 4	10	475	475	5e-7	6.96e-8

Table II.7: An energy balance approach for comparing FLUENT and finite difference heat generation with the convective heat dissipation signified by a change in fluid temperatures.

Case	FLUENT			FD Code		
	Avg. Electr. Temp (K)	Heat generated (W)	Heat convected out (W)	Avg. Electr. Temp (K)	Heat generated (W)	Heat convected out (W)
Case 6b	806.3	3.83	3.23	819	31.24	32.2
Case 6c	1067.2	0.95	0.68	1148	6.48	6.46

As the flow rate is decreased, the accuracy of the FLUENT model decreases. The finite difference code maintains a correct energy balance for all flow rates. When FLUENT can be validated by an energy balance, the results of FLUENT agree with the FD code.

CHAPTER III

THERMAL STRESS ANALYSIS

Several different thermal stress models were used in the process of modeling residual, steady state and transient stresses. The residual stresses were modeled by a uniformly cooled honeycomb structure. The temperature range was from relaxation temperature to room temperature. The steady state model superimposed the residual stress and the operating stresses as defined by the temperature solutions of the finite difference code. Finally, the transient stress model added intermediate temperatures at time steps leading up to the steady state operating temperature. The temperatures for these steps were provided by the transient finite difference model. The residual, steady state and transient models are in order of increasing complexity and computational run time. Since the residual stress model required much less time, it was used to define factors such as mesh density. The very fine meshes needed for comparison with more practical meshes would have taken too long to run with the full transient model. Also, since the residual stress model is isothermal, quarter symmetry may be used in some instances to reduce computational time. In the same manner, the steady state solution holds a time advantage over the transient. Although the transient model will eventually converge on the steady state solution, the steady state model can be solved in two steps without regard to the undetermined intermediate temperature steps. Of course, the validity of the steady state model requires that little plastic deformation take place during startup. Considering this qualifier, the transient solutions will be the most accurate but will also require the longest time to evaluate.

III.1. Isothermal stress solutions to model residual stress

III.1.1. Purpose of model

This research centers around a multi-tool approach for characterizing operating conditions in a honeycomb shaped LCA fuel cell. However, as a starting point, a more general analysis of cool down, post manufacturing, would determine a reasonable estimate of the initial stresses at room temperature. The thermal mismatch stress in the fuel cell must be referenced to an equilibrium state where by assumption there are no internal stresses. The stress-free point determined during manufacturing. Sintering takes place at very high temperatures for the ceramic. For slow cooling rates, viscoelastic creep has been shown to almost entirely eliminate mismatch stress in ceramic-metal laminates above 1200°C (Cai et al., 1997). As the structure is cooled below 1200°C, residual mismatch stress builds. Analysis performed by Eisele shows the equilibrium temperature is closer to 1000°C for the iron based metal used in this case (Eisele, 2004). At this point, 1000°C serves as a reasonable assumption for the stress-free temperature, but it is extremely dependent on the metal selected. A full analysis of the stresses resulting from sintering is outside of the scope of this work. Instead, from 1000°C to room temperature, both an elastic and plastic ABAQUS model will be used to determine residual mismatch stress. The residual stress is important not only as a starting point for the full model, but also as a comparison to observations made during manufacturing. Currently, manufacturing often results in fracture of the specimens. If the ABAQUS model can adequately predict this fracture, then a basis can be established for further failure predictions during operation.

The residual stress plays an important role in fuel cell design. Of course, the residual stress must be small enough to maintain the integrity of the fuel cell after manufacturing. But also, since no external forces are applied during operation, the residual stress may be on the same order as, if not higher than, most stresses occurring during operation. Therefore, the residual stress is an important design parameter in SOFC material selection.

III.1.2. Simple laminate structures

The model setup is fairly simple. The initial temperature condition is 1000°C, and the final state is at room temperature. The honeycomb is free to expand or contract in all directions; thus, only the rotation and translation of the honeycomb are constrained. Eight-node, linear brick elements with reduced integration are used to model the structure. Isotropic plastic strain hardening effects are included, using data collected from tensile testing (Eisele, 2004). Plastic data is only available for $Fe_{39}Ni_8Cr$.

The displacement of the ceramic and the metal is constrained at the joint of the two materials. Therefore, the stresses at the joint are of great interest to design of the SOFC. As the volume of the SOFC changes, two main sources of stress emerge. Consider a ceramic and a metal plate joined to form a laminate. If cooled, the laminate will have stress at the joint due to volumetric shrinkage. This mismatch stress is present in the SOFC, but in addition, the vertical laminates are bent due to the shrinkage of horizontal members. Insight may be gained from first modeling the residual stress in a simple laminate and bilaminate structure. Figure III.1 shows a laminate of YSZ and $Fe_{39}Ni_8Cr$ after cooling from 1275K to RT.

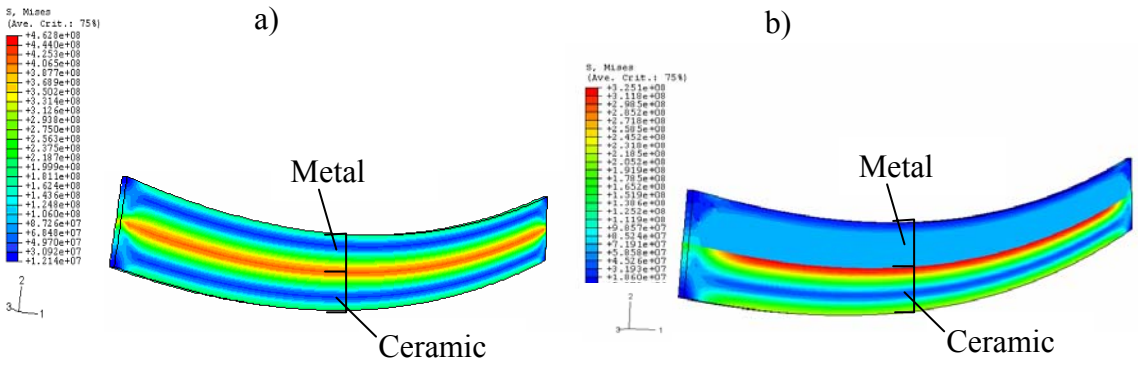

Figure III.1: Stress due to CTE mismatch in a laminate of YSZ and $Fe_{39}Ni_8Cr$ after temperature is reduced from 1273K to RT modeled a) elastically and b) plasticallly. Each laminate component is 0.2 cm x 0.012 cm x 3 cm.

The laminate bends toward the side of the metal since the metal shrinks more. Note that the von Mises stress in the metal in Figure III.1 is well above the yield of 56 MPa for $Fe_{39}Ni_8Cr$. As a result, the stress in the metal and ceramic is reduced as the metal plastically deforms. The measured bending of laminate specimens has been used in the past to measure residual stress experimentally (Cai et al., 1997a). However, the hybrid SOFC is a symmetric laminate. A symmetric laminate does not bend in the y-direction because one material is equally constrained on both sides by the other. A bilaminate, shown in Figure III.2, more adequately describes the hybrid SOFC joint.

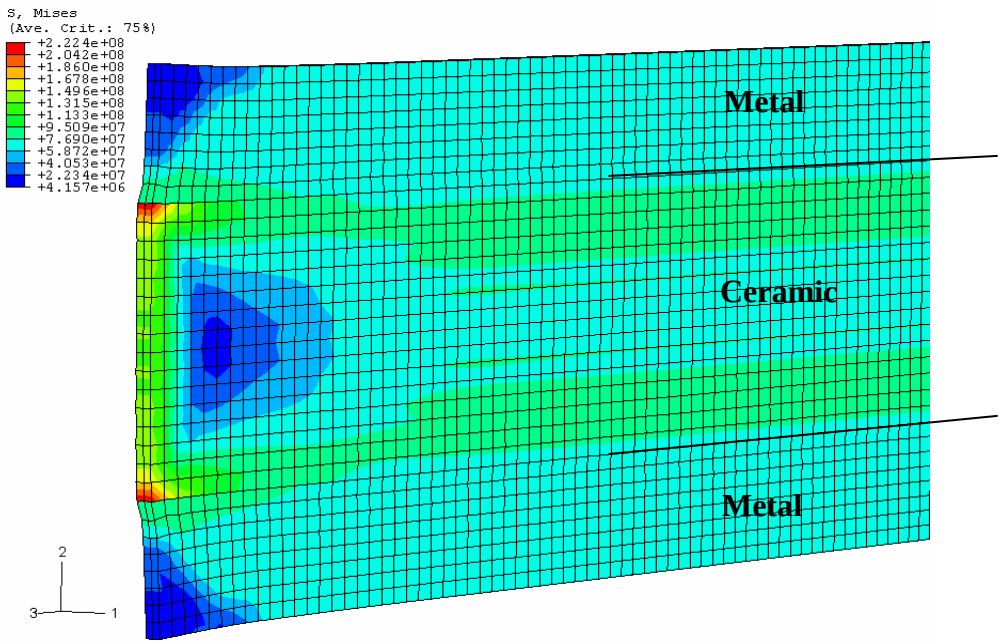

Figure III.2: Stress due to CTE mismatch in a bilaminate of YSZ and $Fe_{39}Ni_8Cr$ after temperature is reduced from 1273K to RT, modeled plasticallly. The ceramic component is 0.2 cm x 0.012 cm x .3 cm while the each metal component is half as tall (0.1 cm x 0.012 cm x .3 cm).

In the bilaminate, the two materials are no longer able to flex because the structure is symmetric. Bilaminates have pronounced edge effects, regions of large stress caused by the ability of the material to strain near the edge. The bilaminate was modeled for several different lengths ranging from 0.3 cm to 1.2 cm long. The stress remained the same for each length. The regions of high residual stress in the bilaminate are indicative of the stress in the full SOFC model but requiring only seconds to evaluate. In the future, more advanced fabrication material models may be optimized using a simple bilaminate structure.

More specifically, the thermally induced residual stress between flat elastic laminates can be characterized by two basic trends. First, the in-plane normal stress (σ_{zz}) at the joint is large it the center of the laminate and decays to zero approaching the free

edge. Secondly, the peeling stress (σ_{yy}) and shear stress (σ_{yz}) increase approaching the free edge (Chiu and Liou, 1994). These two trends are referred to collectively as edge effects. The stress near the interface is drastically reduced when the film is considered plastic-elastic with power-law strain hardening assumption (Lambropoulos and Wan, 1989). Several factors alter the stress concentration due to edge effects. In the elastic study, increasing coating stiffness by increasing elastic modulus or thickness results in a larger end effects zone (Chiu and Liou, 1994). For plastic laminates, large aspect ratios (corresponding to thicker coatings) increased the magnitude of the stress concentration (Lambropoulos and Wan, 1989). Considering the more applicable plastic results, the normalized values for peeling and shear stresses are referenced in Figure III.3.

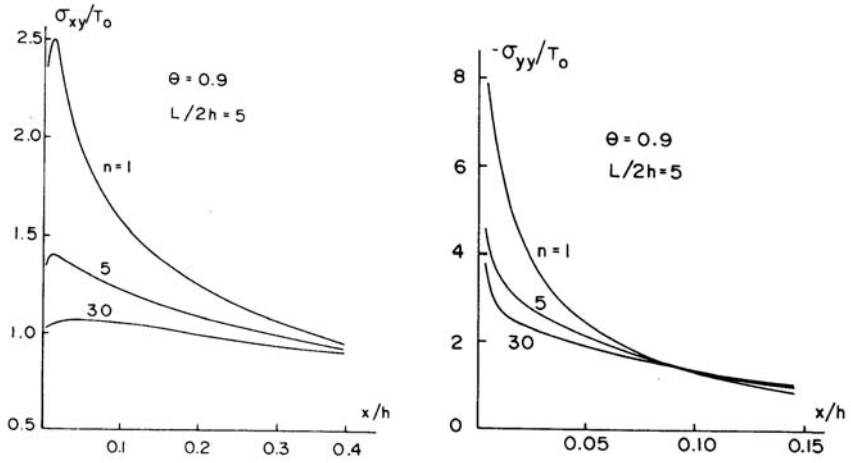

Figure III.3: Shear (left) and peeling (right) stresses for a metal/ceramic laminate, normalized to the yield stress of the plastic material (Lambropoulos and Wan, 1989).

The peeling and shear stresses correspond to the opening of crack tips or delamination of the two materials. These two elevated stresses will form a basis for analyzing the potential for failure in the hybrid SOFC.

III.1.3. Isothermal honeycomb model

III.1.3.1. Modeling using reduced-integration elements

The full model of residual stresses includes the bending effects caused by contracting and expanding horizontal members. The ABAQUS input file used in most analyses was generated by a custom FORTRAN program which created nodes and elements based off input parameters identical to the FD code inputs. The FORTRAN code is further developed in subsequent analysis to interact with the FD code for steady state and thermal stress analysis. Therefore, to verify the code that was used to write the input file, a model was also constructed using ABAQUS CAE. ABAQUS CAE is an interactive GUI for use with ABAQUS that allows the user to draw geometry, specify boundary conditions and process analyses in user-friendly graphical form. However, ABAQUS CAE is not easily integrated with the finite difference code. Typical results of the elastic and plastic analysis generated by the code are given in Figure III.3.

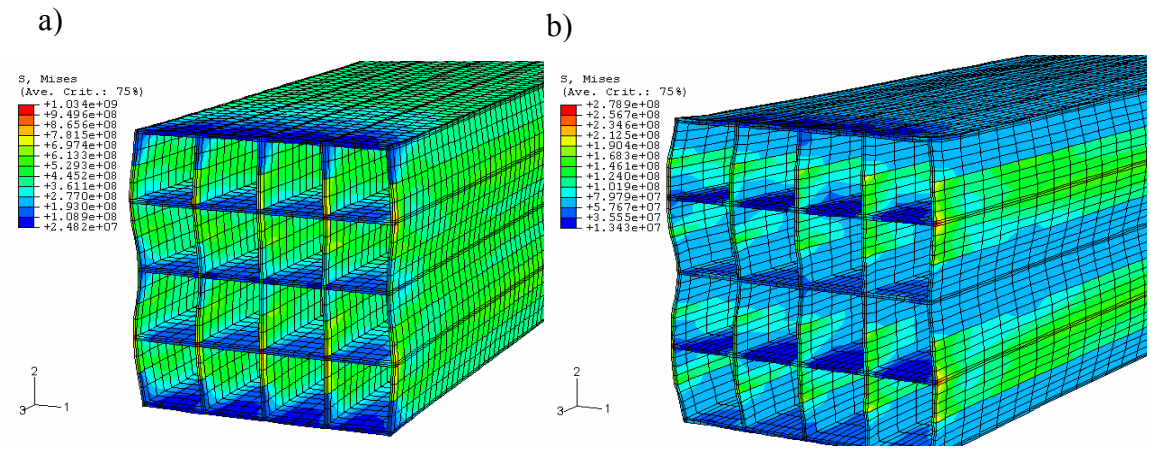

Figure III.4: a) Elastic and b) plastic models of von Mises stress for a 4x4 unit cell, YSZ-Inconel hybrid, isothermal cool-down from 1000°C to RT.

Figure III.4 shows the necessity of modeling the honeycomb as plastic. The stress in Figure III.4a) is almost three times what is necessary to yield the metal. The metal and

ceramic would fail at the stresses shown in the elastic model. The plastic numbers are much more reasonable. However, both the elastic and plastic models show higher stress at the bending point in the ceramic than in the joint. In manufacturing, extrusion of the hybrid honeycomb has resulted in cracking at or near the joint of the metal and ceramic, on the ceramic side (Eisele, 2004). The ABAQUS results, shown in Figure III.3, have two high stress regions, the joint and the bending point on the exterior of the ceramic. However, the mesh in Figure III.4 is fairly coarse. The bending is modeled with 8-node linear brick elements. Using more elements may better capture bending of the ceramic. The mesh was refined (Figure III.5) by changing the inputs of the FORTRAN program.

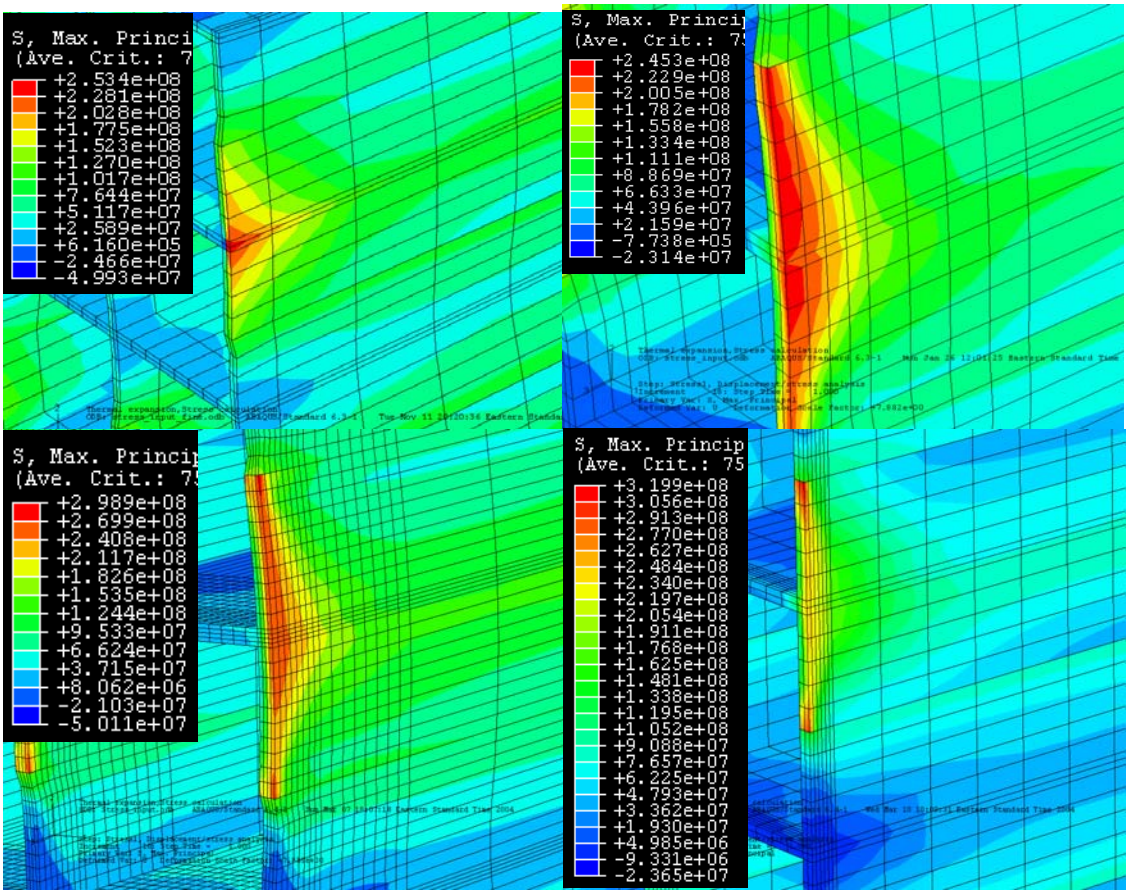

Figure III.5: Increasing mesh density of the input file resolves the stresses at the edge of the ceramic, altering the location and intensity of maximum principle stress (MPa).

After refinement of the mesh, the greatest stresses are clearly at the joint and along the edge of the ceramic. The linear stress elements probably contributed to the error. The definitions of element sets and geometry were confirmed by the visualization software ABAQUS VIEWER. Also, the proper function of the FORTRAN code was confirmed by inspecting all stresses and displaying each element set individually and by querying node and element values. None-the-less, a 2 x 2 CAE model was created taking advantage of the vertical (y-direction) and horizontal (x-direction) planes of symmetry meeting at the central axis. Since the mesh was not matched identically, the results will not be identical, but the CAE results are in very good agreement with the input file results, as seen in Figure III.6.

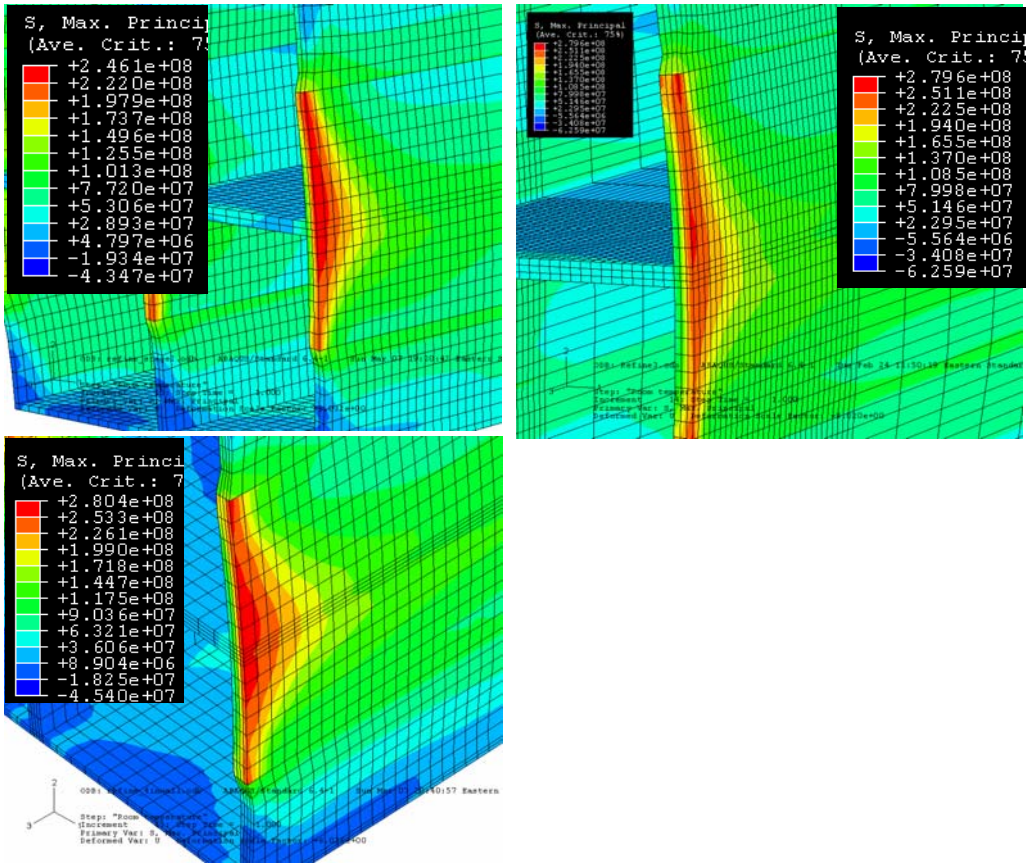

Figure III.6: Increasing mesh density in ABAQUS CAE resolves the stresses at the edge of the ceramic (MPa).

III.1.3.2. Modeling using full integration elements

Further investigation of the mesh reveals that the mesh size with reduced integration linear elements does not accurately converged upon the solution obtained with a refined quadratic element mesh. Reduced integration elements use fewer integration points for the stiffness matrix (in the case of linear, 1 integration point). In this case, the linear elements displayed poor accuracy for two likely reasons. A singularity is located at the corner edge of the joint. The singularity appears to approach infinity as the mesh is refined. Also, bending in the x-y plane is severe enough to require more than two elements across the thickness. The gradient in the x-direction across the thickness, as seen in the quadratic results, would require many elements through the thickness to accurately capture bending due to edge effects. Figure III.7 shows the quadratic mesh compared to the linear (reduced integration).

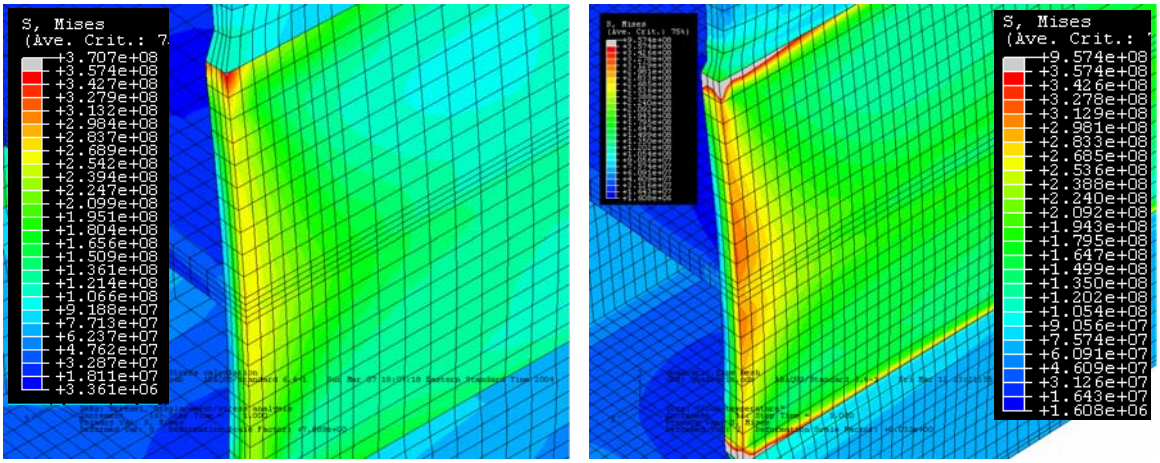

Figure III.7: Reduced integration linear mesh (left) when compared with reduced integration quadratic mesh (right) does not result in the same maximum von Mises stress on the surface or the appropriate peak stress at the edge of the joint.

The reduced integration quadratic mesh is verified by reducing the mesh size to prove convergence. Excellent convergence is achieved with the quadratic mesh everywhere except at the singularity (Figure III.8).

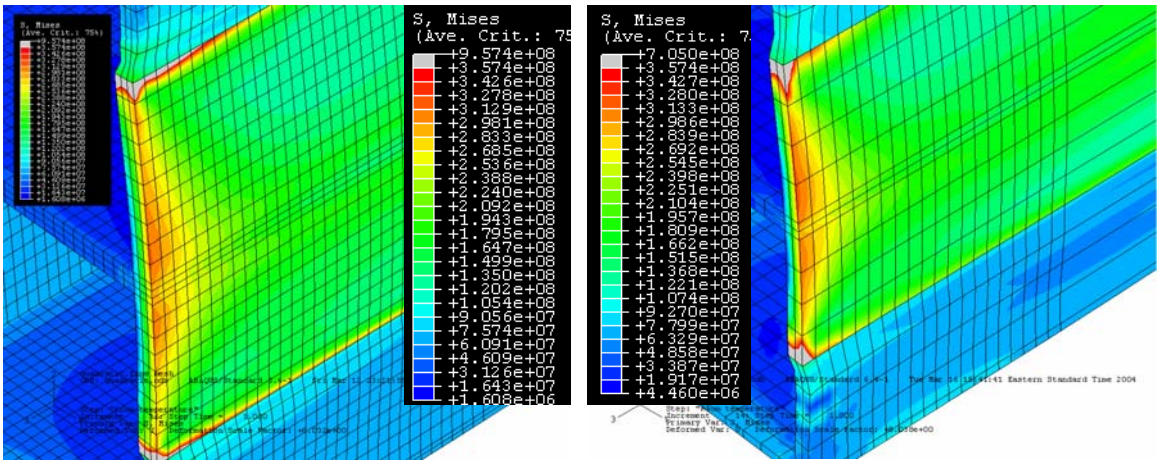

Figure III.8: The fine reduced integration quadratic mesh (left) has very similar stress results as the coarse mesh (right).

By comparison, the reduced integration linear elements do not match the quadratic solution well. Linear solutions should follow the quadratic without capturing the bending in between elements. The stress can be shown graphically by selecting paths and displaying the stress solution along the path. Figure III.9 shows the paths used to compare the results of different mesh sizes. In the case of reduced integration, the solution is shifted away from the quadratic solution, as shown in Figure III.10.

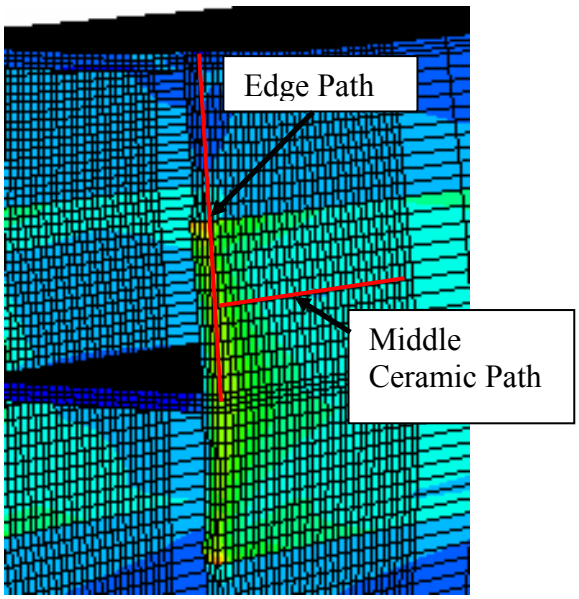

Figure III.9: Paths used to study mesh convergence in Figure III.10.

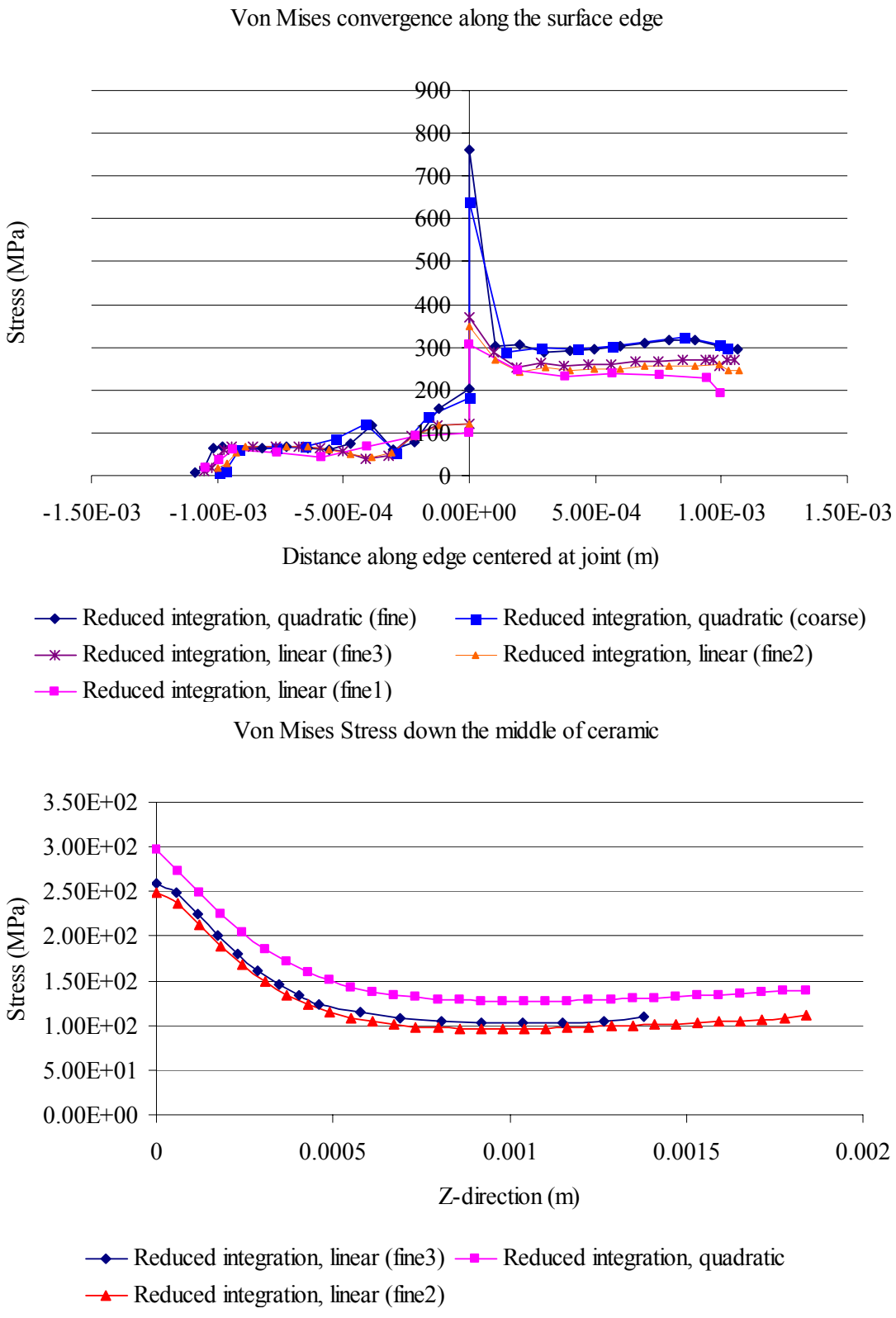

Figure III.10: Mesh convergence of linear and quadratic reduced order elements along two paths.

If full integration is used instead of reduced integration, the accuracy of the linear solution is greatly increased. Figure III.11 shows that the full integration linear as opposed to the full integration linear much more closely matches the reduced integration quadratic. Note that all models in Figure III.11 have the same mesh.

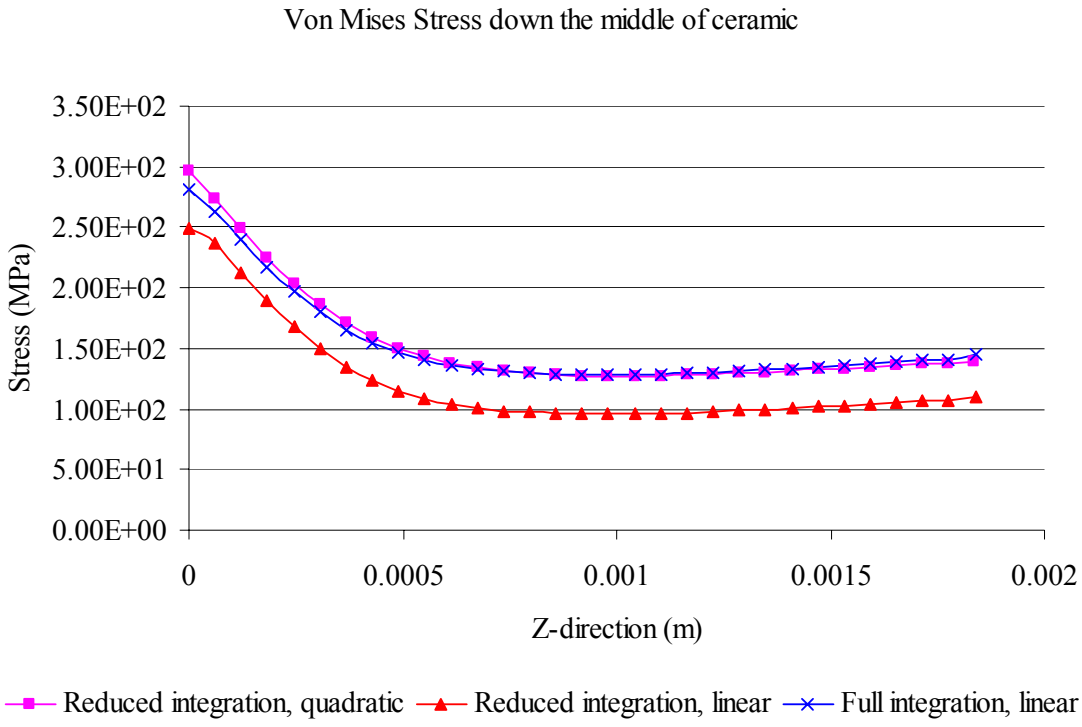

Figure III.11: Mesh convergence, comparing full integration to reduced integration elements.

The singularity at the joint near the edge, seen in Figure III.10, should get larger as the mesh becomes smaller because the integration point approaches the location of singularity. Figure III.12 compares the stress along the joint of the ceramic and metal for two different full integration meshes. Results for von Mises and maximum principal stresses are plotted integration points in the metal and ceramic elements at the joint.

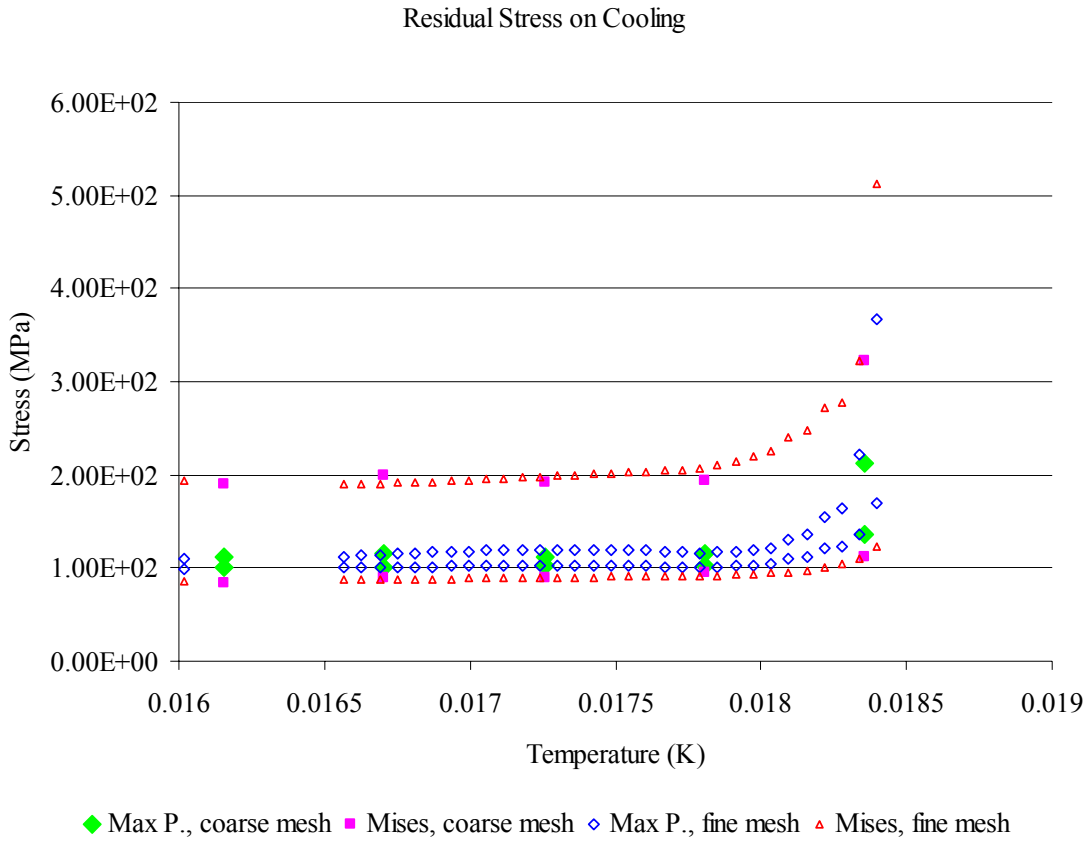

Figure III.12: The full integration linear elements produce roughly the same result at integration points regardless of mesh density.

Finally, a coarse mesh was solved using full integration quadratic elements in the quarter-symmetric ABAQUS CAE model. As expected, the results closely follow the reduced integration quadratic results. The full integration quadratic elements take much longer to run than the reduced integration without significant improvements in accuracy. Figure III.13 illustrates the stress distribution for two different full-integration, quadratic mesh densities.

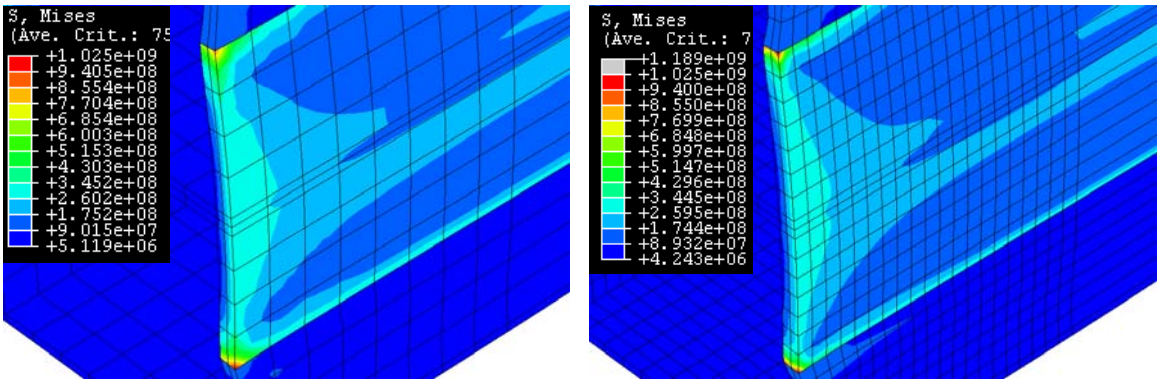

Figure III.13: Quadratic full integration elements give similar results to the reduced integration elements of Figure III.8.

As expected, the stress concentration is more resolved by the full integration quadratic elements. Also, the elements in the metal section bordering the stress concentration are not distorted as they are in the reduced integration mesh. The distortion may have been a result of the reduced integration.

The material failure due to residual stresses must be analyzed separately for metal and ceramic. Material failure was first analyzed using the reduced integration mesh shown in quadrant IV of Figure III.5. The von Mises stress determines failure in the metal, and the maximum principle stress determines failure in the ceramic. The stress values of each are plotted in Figure III.14 along a path down the joint. Several different length models showed that the maximum stress did not depend on the length of the structure. The magnitude of the maximum stress is dependent on the x-y dimensions and material properties. Wider cells result in larger stresses in the ceramic side of the joint. The same model was evaluated using full integration as well. The full integration results are also plotted against the reduced integration in Figure III.14.

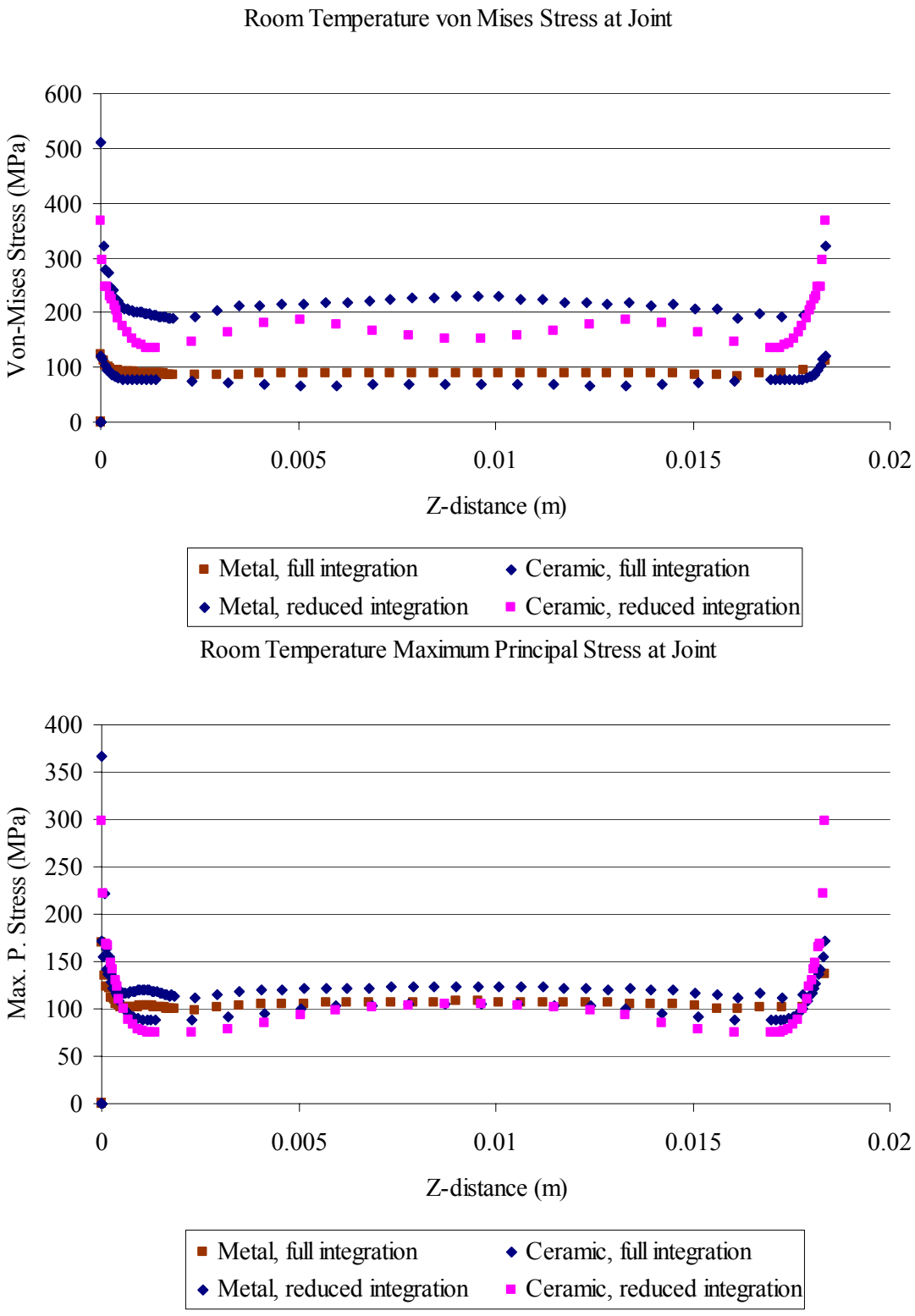

Figure III.14: The maximum principal (bottom) and von Mises stress (top) of a 4 x 4 square celled honeycomb hybrid structure cooled from relaxation temperature (1000K) to RT (293K) is greatest at the joint of the ceramic and metal (0.86 x 0.86 x 3cm, 120µm thick walls). Both the reduced and full integration results are plotted.

The maximum stress in the contour plot is at the front corner. Throughout the cool-down from the relaxation temperature, ABAQUS shows that this point is the maximum. Plotting the von Mises and maximum principle stresses against the decay of temperature over time, a steady increase in stress can be shown (Figure III.15).

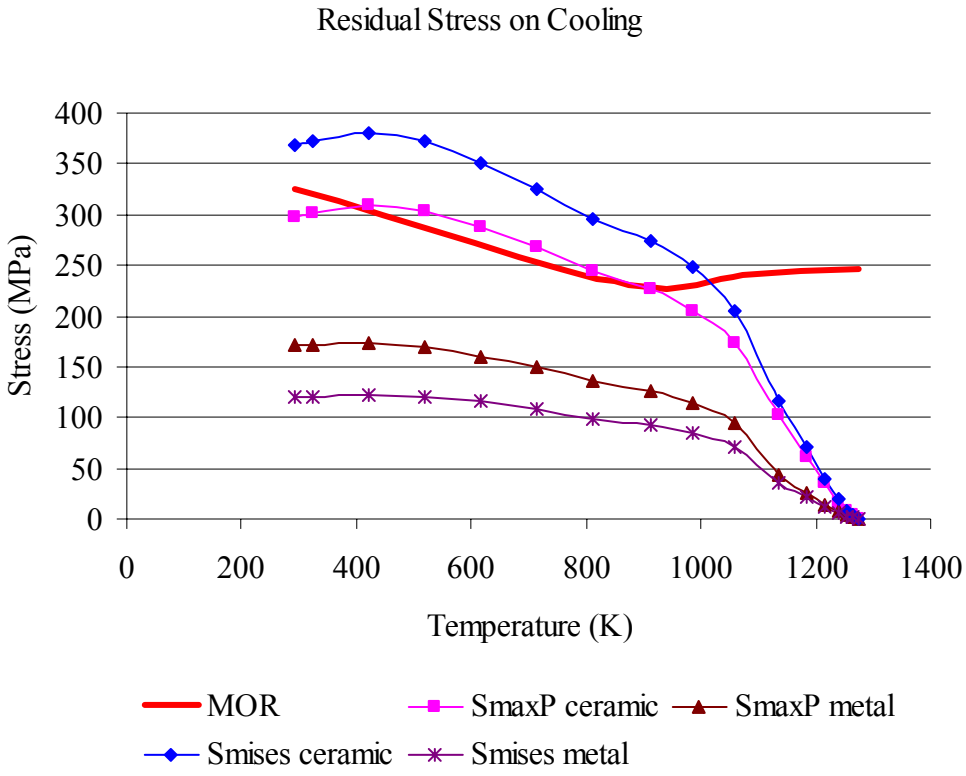

Figure III.15: Residual stress increases as the structure is cooled. Only, the corner node at the joint is plotted for the finest linear reduced integration mesh. MOR data for fully dense YSZ is also plotted.

Even compared to the ideal failure criterion of dense YSZ, the maximum principle stress in the ceramic exceeds critical at 911K. However, actual co-extruded honeycombs will not have the ideally sharp corner; therefore, the stress concentration at the edge will be different in magnitude. Also, the stress concentration will be mitigated by the fracture toughness of YSZ. The material itself at the joint may also be a mixed phase of the two

constitutive materials, as is inherent in the intimate bonding of the two co-fired pastes. A mixed phase may have different properties affecting expansion and strength of the joint. In addition, for an even more precise estimate of failure, the porosity of the ceramic should be determined experimentally and used to knock down the MOR data. Even so, the predicted failure of the joint and the location of failure in the model concur with experimental results shown in Figure III.16.

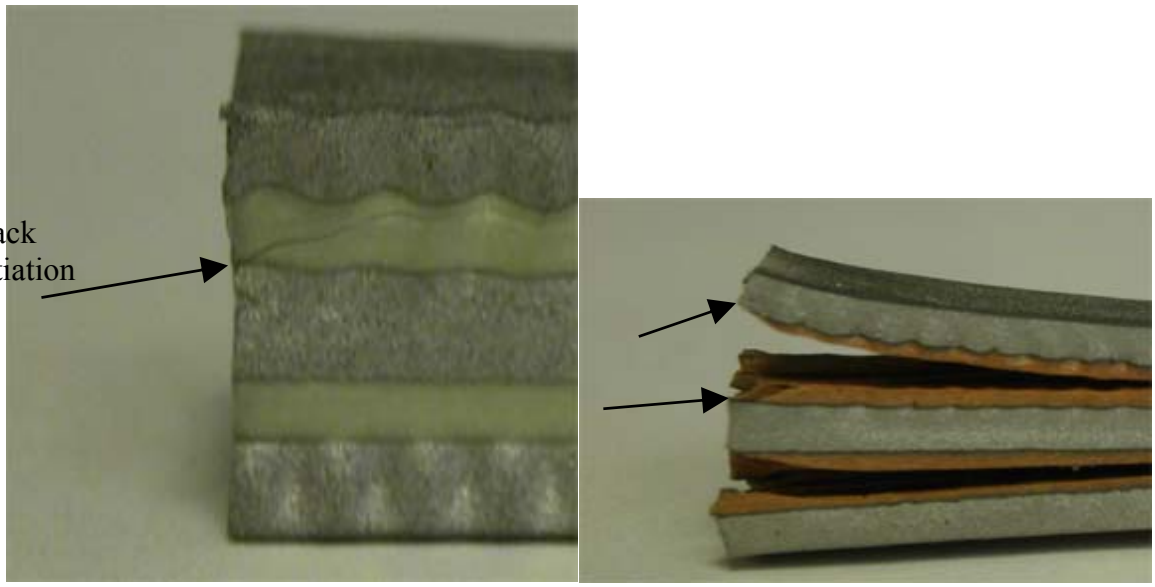

Figure III.16: Failure observed after manufacturing of hybrid structure (Eisele, 2004). Cracks formed and grew as the structure was cooled from sintering temperature to room temperature.

The failure of manufactured samples shown in Figure III.16 occurred using the same material as modeled in Figure III.15. The cracking initiated at elevated temperatures (Eisele, 2004). Of course, current modeling does not account for manufacturing anomalies. The exact material composition of the joint is not actually known. Diffusion of the two materials at the joint may lead to a localized change in material properties.

Furthermore, the model is ideally shaped; thus, the quality and homogeneity of the extrusion is not considered.

III.2. Stress analysis during operation

The relieved state of stress occurs at a temperature above that reached during operation. Even though cooling after manufacturing is considered isothermal, stress builds as the structure is cooled because of the CTE mismatch of the materials. As a result, during operation, instead of increasing the CTE mismatch, high temperatures actually relieve the accrued residual stresses. Two other stress risers may exist. First, the counter-flow conditions will create a temperature gradient down the length of the components. This type of static gradient stress has been calculated for planar SOFC's over a temperature difference of 200-300K (Yakabe, 2001). Yakabe determined stresses were up to 70 MPa for a temperature gradient of 200K across a YSZ electrolyte. Similar stresses may be present in the hybrid SOFC depending on the operating conditions. Also, since the metal and ceramic are joined in the hybrid SOFC, a stress would develop if the ceramic was at a higher temperature than the metal. The fuel cell will be analyzed with the finite difference code and ABAQUS to determine the magnitude of stresses occurring during operation.

III.2.1. Using ABAQUS to distribute FD solution

As with the isothermal case, ABAQUS was used to solve for the thermal stresses due to elastic and plastic deformation in the SOFC. Instead of integrating the finite difference code into ABAQUS as a UMAT, the code is executed independent of ABAQUS. An ABAQUS input file is then written by FORTRAN with the nodal

temperature field included as a boundary condition. By this method, ABAQUS CAE is bypassed with all geometry constructed according to the finite difference code inputs. If the geometry were created independently of the FD code, any model parameterization, be it cell width, cell stacking, etc, would require the construction of a new model. Secondly, the mesh created in FORTRAN has the distinct advantage of consistent nodal and element numbering. The nodes from the finite difference code must be matched with ABAQUS to correctly transfer the nodal temperature data. However, as illustrated in Figure III.17, the mesh in ABAQUS is much denser than in the FD code.

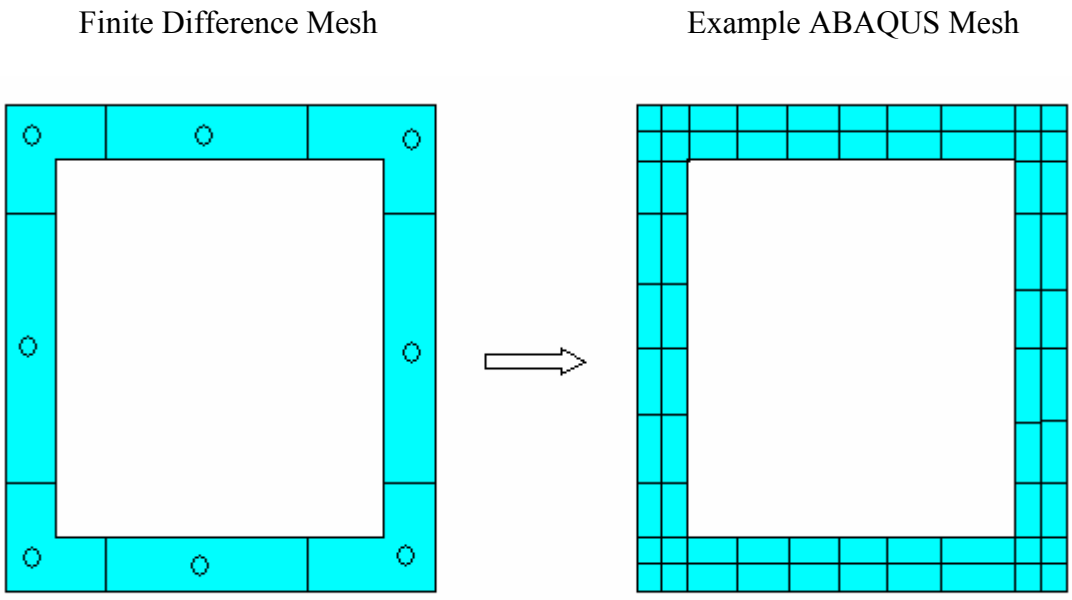

Figure III.17: The finite difference mesh (left) is much coarser than the ABAQUS mesh (right).

The node and element numbering in the FORTRAN input file is known; so, the temperature data from the finite difference code is easily transferable to the ABAQUS input file. The mesh in the input file is built around five variables which become the user

inputs. One variable is the number of elements in the z-direction. In addition, the number of elements in four other segments of the geometry must be specified. They are shown in Figure III.18.

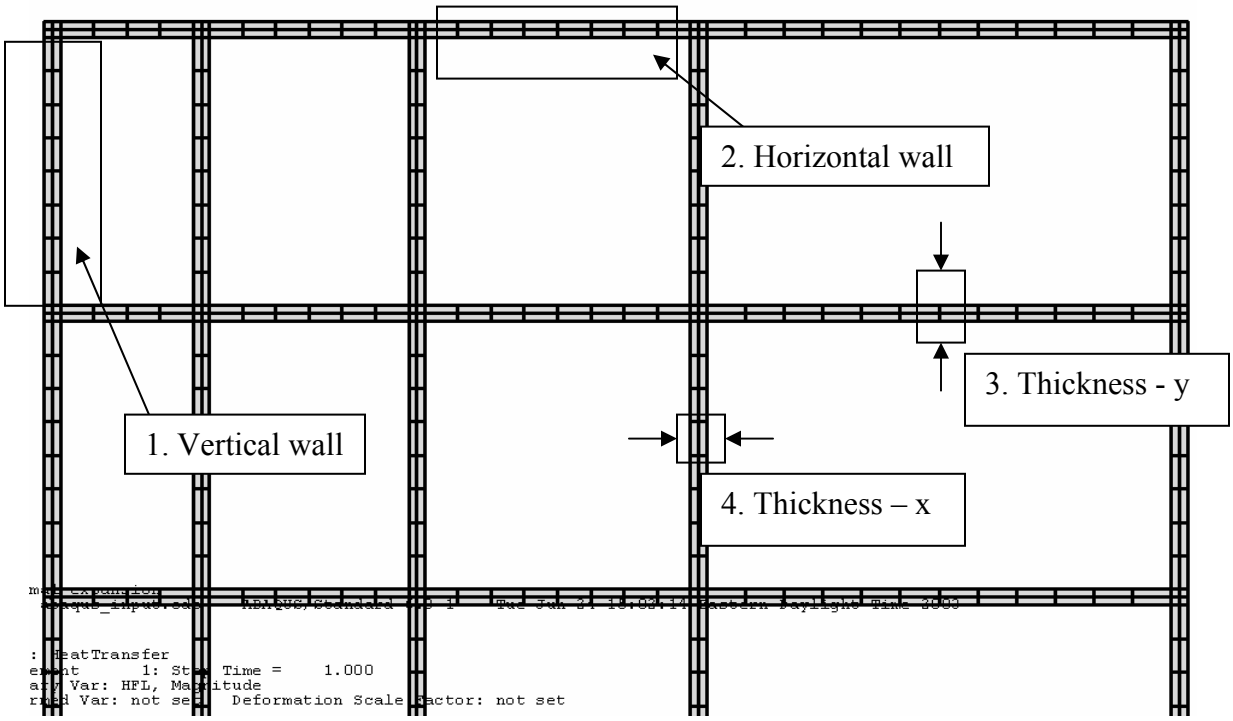

Figure III.18: The number of elements in a vertical wall, horizontal wall, thickness in the y direction and thickness in the x-direction must be specified to create the input file.

To keep the element size consistent, more elements should be used in the larger horizontal walls if the cell structure is graded in the x-direction and more in the larger vertical walls if graded in the y-direction. To achieve the varying number of elements, the variables for 1 and 2 are stored in matrices, allowing the user to input multiple values. To achieve the graded meshing in Figure III.18, the horizontal wall had inputs (4,6,8,10).

Another possible user input would simply be the global element size. Specifying a size would make the mesh uniform. However, for the ABAQUS mesh to match the FD mesh, a node must fall in the middle of each rectangular segment. Matching the meshes is more easily achieved by requiring the number of elements in a rectangular segment to be even.

The temperature field from the FD code must be processed one step further before performing the stress analysis. Since the ABAQUS mesh is much denser than the mesh of the FD code, the temperature of nodes not in the FD code must be interpolated by ABAQUS. A thermal model is used with linear 8-node linear thermal brick elements to distribute the temperature to all the ABAQUS integration points. The run time of the thermal model varies widely depending on the size of the model. For the 4x4 unit cell, 3cm long model, the thermal field was calculated in 2 minutes. However, the computational time has been as high as half an hour with increased mesh evaluated over many time steps.

After solving for the temperature distribution at each time step, the FD code writes an ABAQUS input file with the steady state temperature solutions imbedded in the input file. The code also has the ability to write an ABAQUS input file for vertically stacked fuel cell designs as well as graded cell sizes (Figures III.19 and III.20).

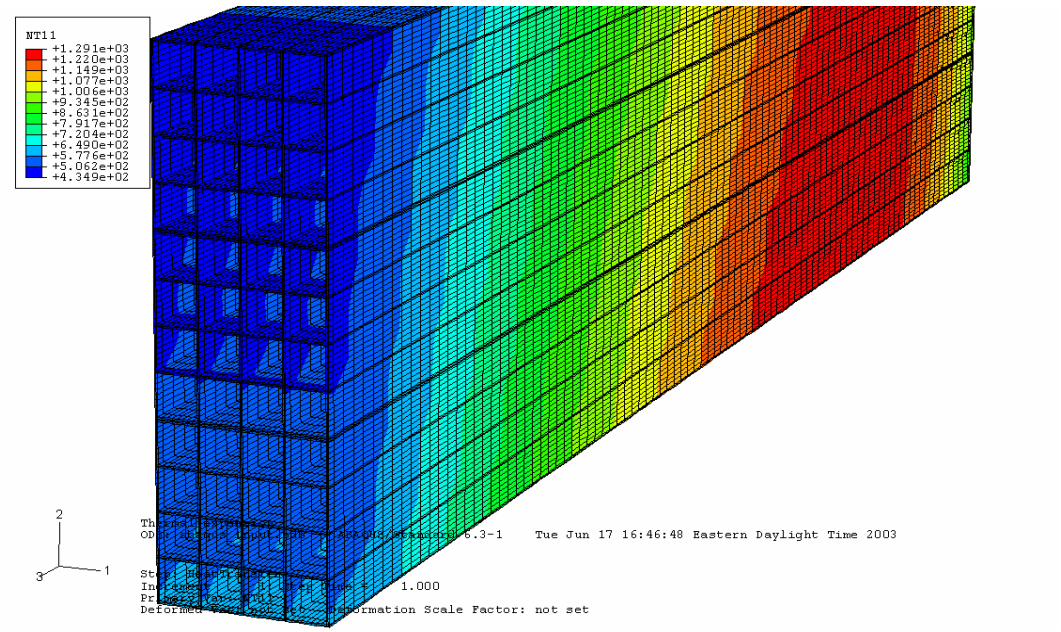

Figure III.19: Sample ABAQUS solution at steady state for a fuel cell stack of 3, 4x4 units has symmetry only in the x-direction since the cells generally get hotter proceeding down the stack.

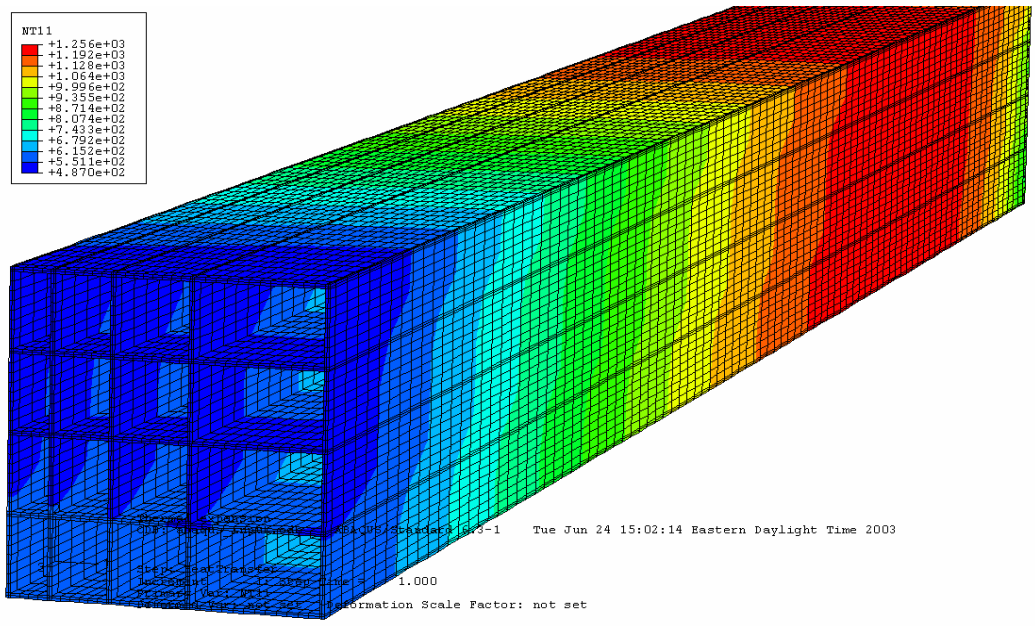

Figure III.20: General ABAQUS thermal solution for a graded fuel cell design has no plane of symmetry.

Asymmetry of the temperature in the x-direction is a result of the evenly distributed volumetric fluid flow in Figure III.20 (i.e. while the mass flow is equal in each channel, the velocity of the fluid in the larger channels is less).

III.2.2. Stress analysis according to results of ABAQUS thermal analysis

With respect to node definitions, element definitions and node/element sets, the input code for the stress analysis is the same as the thermal input file. An 8-node linear brick element was used for stress analysis, as with analysis of similar structures (Yakabe et al., 2001; Keegan et al., 2002). Much of the boundary conditions and analysis techniques are identical to the isothermal analysis, but they will be listed in detail here.

III.2.2.1. Boundary conditions

Constraining the hybrid is often difficult due to the asymmetry in the temperature field and the structural shape. A cantilever-like approach is used to secure the SOFC. In this manner, the rotation and translation of the entire structure can be prevented without preventing the shrinking of either constituent or restricting the arching of the fuel cell down the length (Figure III.21). Arching has occurred in examples due to a hot region on the bottom half of the fuel cell near the middle. This would cause expansion of the bottom half relative to the top, resulting in bending.

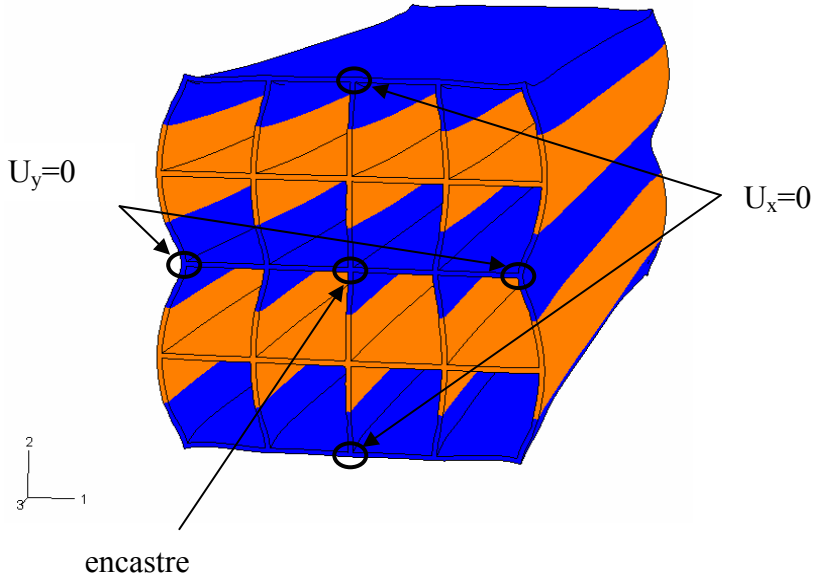

Figure III.21: Physical constraints are placed at specified nodes to anchor the structure.

Both ends may be constrained by manifolds in a more advanced design. For now, the results are checked to make sure the boundary conditions at the five nodes do not cause significant stress concentrations.

The relaxation temperature was also defined as a boundary condition. The entire set of nodes was specified an initial temperature condition of 1273K. Subsequent temperatures were read from the results file of the thermal analysis.

III.2.2.2. Material properties

The material properties (Table II.1 and Table II.2) are, for the most part, simple to declare using ABAQUS standard. However, the CTE and plastic properties must be altered to be read correctly by ABAQUS. The stress-strain plastic property data is specified using the *PLASTIC line. The strain data as read by ABAQUS is the plastic

strain. The elastic strain corresponding to Table II.2 must be subtracted from the total strain numbers. The data as entered into ABAQUS is listed in Table III.1.

Table III.1: Stress-plastic strain data for $Fe_{39}Ni_8Cr$ does not include elastic strain.

Stress (MPa)	Plastic Strain
57.682	0.0
66.469	0.002
81.526	0.00721
92.386	0.01210
101.96	0.01711
110.14	0.02221
117.56	0.02691
132.52	0.03691
143.58	0.04691
153.84	0.05711
189.46	0.09691
219.89	0.14691

CTE in ABAQUS is defined relative to a reference or ZERO temperature. The strain due to thermal expansion is then calculated as the strain at the current temperature minus the strain at the reference temperature. If the ZERO value is not specified, ABAQUS assumes the reference temperature is 0°(not unit specific). The ZERO value was set to 293K in analyses.

III.2.2.3. Step definitions in transient analysis

Stress was assumed to come to equilibrium within each time step. Strain rate was not considered because the actual strain displacement between each step is small. Increments within each time step have a definition from 0 to 1, where 0 is the initial and 1 is the final increment. The time increments were allowed to self-adjust in ABAQUS according to built in convergence criterion. For the isothermal cool down, the initial user

input increment was 0.1, corresponding to a 100K per increment. The increment size was frequently reduced automatically to allow convergence under plastic deformation. For each transient time step, only 1 increment was evaluated per time step. ABAQUS rarely needed to reduce the time step for convergence during transient analysis.

III.3. Using the thermal-stress analysis tools to analyze performance and integrity

III.3.1. Model Setup

A transient thermal-stress analysis was performed on a 4x4 unit celled hybrid SOFC, composed of a YSZ electrolyte and an $Fe_{39}Ni_8Cr$ interconnect. The overall dimensions were 0.86 x 0.86 x 3cm. According to the performance model of Dempsey (Dempsey, pers. com., 2004), the temperature necessary to initiate the electro-chemical reaction is about 910K. Therefore, the inlet air temperature was pre-heated to 980K for this example (at 6.24e-5 kg/s total flow). The fuel inlet temperature remained at 300K at a mass flow rate of 2.784e-8 kg/s (total flow). The resulting power output was 1.16W at a power density of 0.52W/cc.

III.3.2. Finite difference transient temperature field

To analyze the finite difference results, the average electrolyte element temperature at the fuel inlet is plotted over a range of time. The side of the electrolyte nearest the cold fuel inlet should take more time to heat-up compared to the front of the electrolyte. Figure III.22 maps the various transient heating trends solved by the finite difference code in a 3cm SOFC.

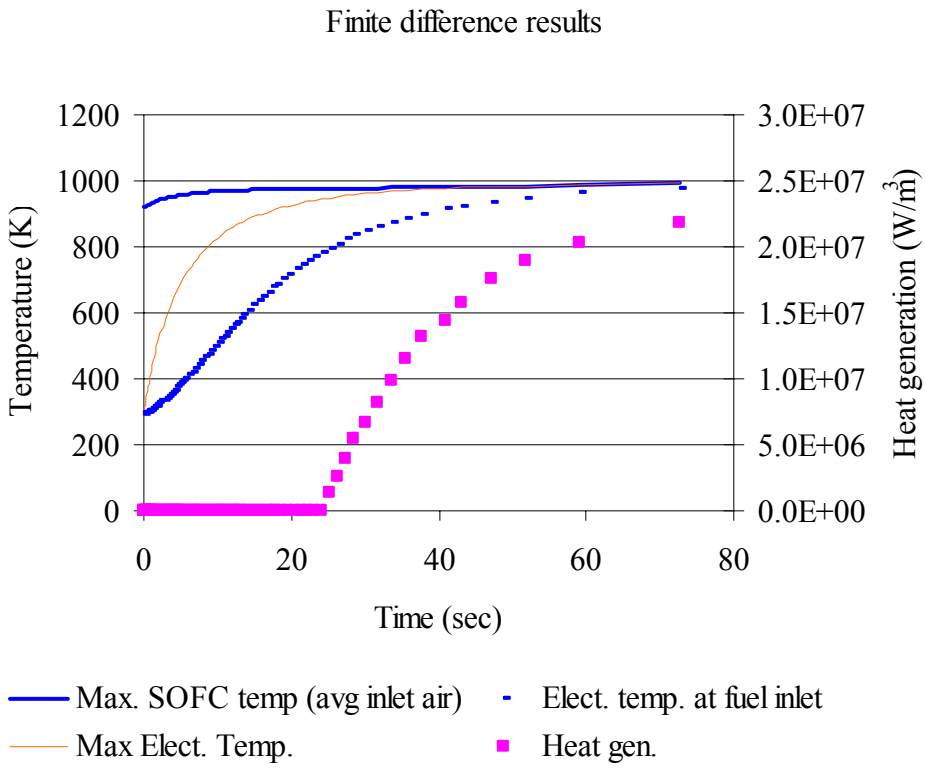

Figure III.22: The temperature of the bottom electrolyte, near the fuel inlet, represents heating in the electrolyte during startup.

The finite difference results are interpolated by ABAQUS. Figure III.23 shows contour plots of the ABAQUS thermal solution. Thermal contour plots more easily display the finite difference thermal solution in Figure III.22 in three dimensions. Note that air is flowing in the front face as shown. Also, to capture the subtle temperature contour, the maximum and minimum spectrum values in each slide are recalculated.

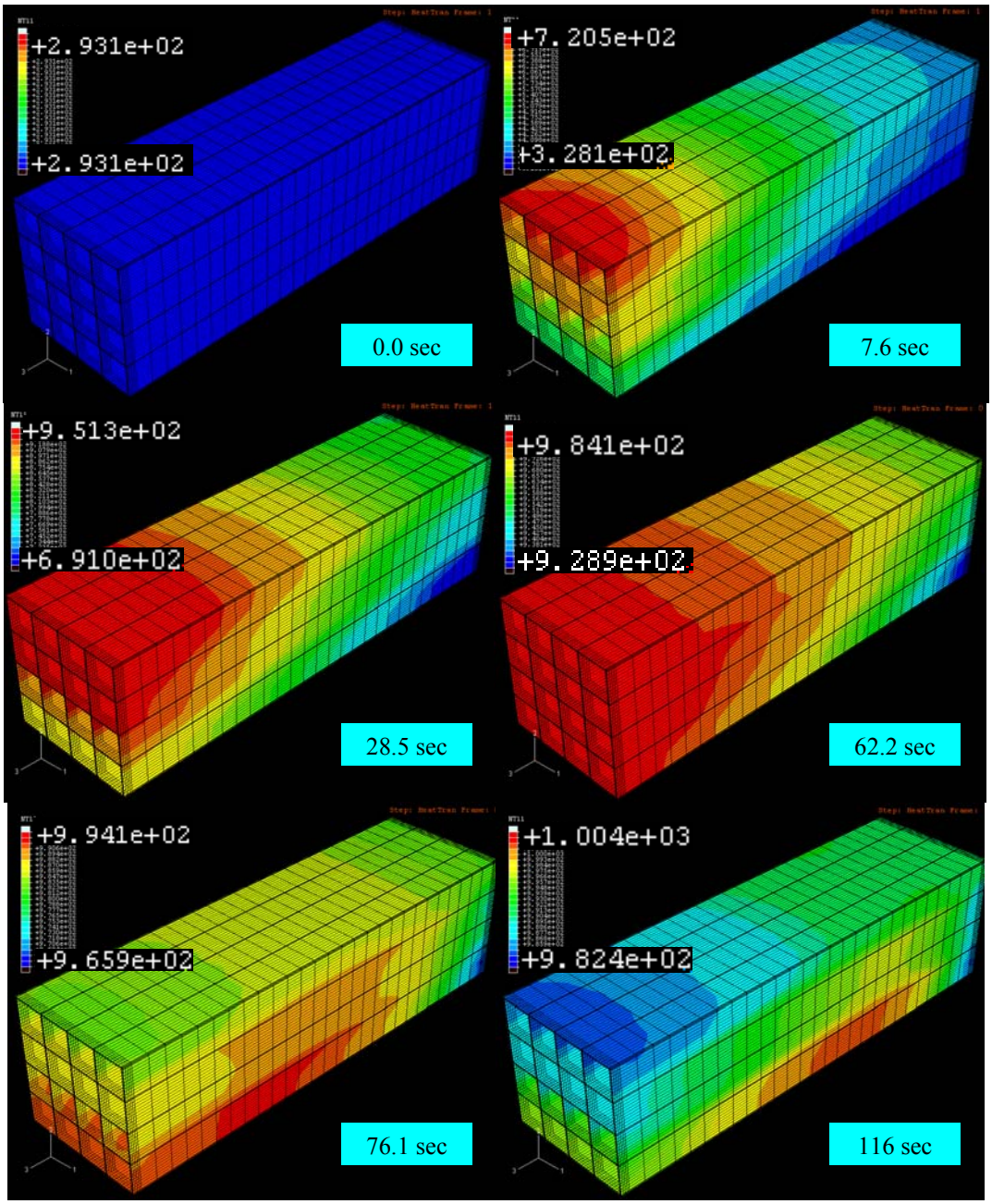

Figure III.23: The temperature distribution at start-up is interpolated from the results of the finite difference code. Moving left to right and top to bottom: 1) The fuel cell begins at RT. 2-3) Hot inlet air heats the structure. 4) The chemical reaction begins to heat the electrolyte. 5-6) The air temperature is now below the operating temperature, resulting in convective cooling.

III.3.3. Contour plots of stresses

For simplicity, the edge of the ceramic will be focused on since the critical stresses rely on the edge effects in the honeycomb. Stress in the y-direction is most important because in general, at the edge, the peeling stress (σ_{yy}) is the largest component of stress and it is the most important for cracking in the ceramic. The maximum stress during cool down occurs slightly above room temperature because at lower temperatures, the CTE of the metal is lower than the ceramic, thus relieving stress upon further cooling. Figure III.24 shows the time of greatest stress at the joint, just before the end of the cooling period. Figure III.25 shows the compressive stress at the front face in the ceramic at high temperatures after heat-up of the fuel cell.

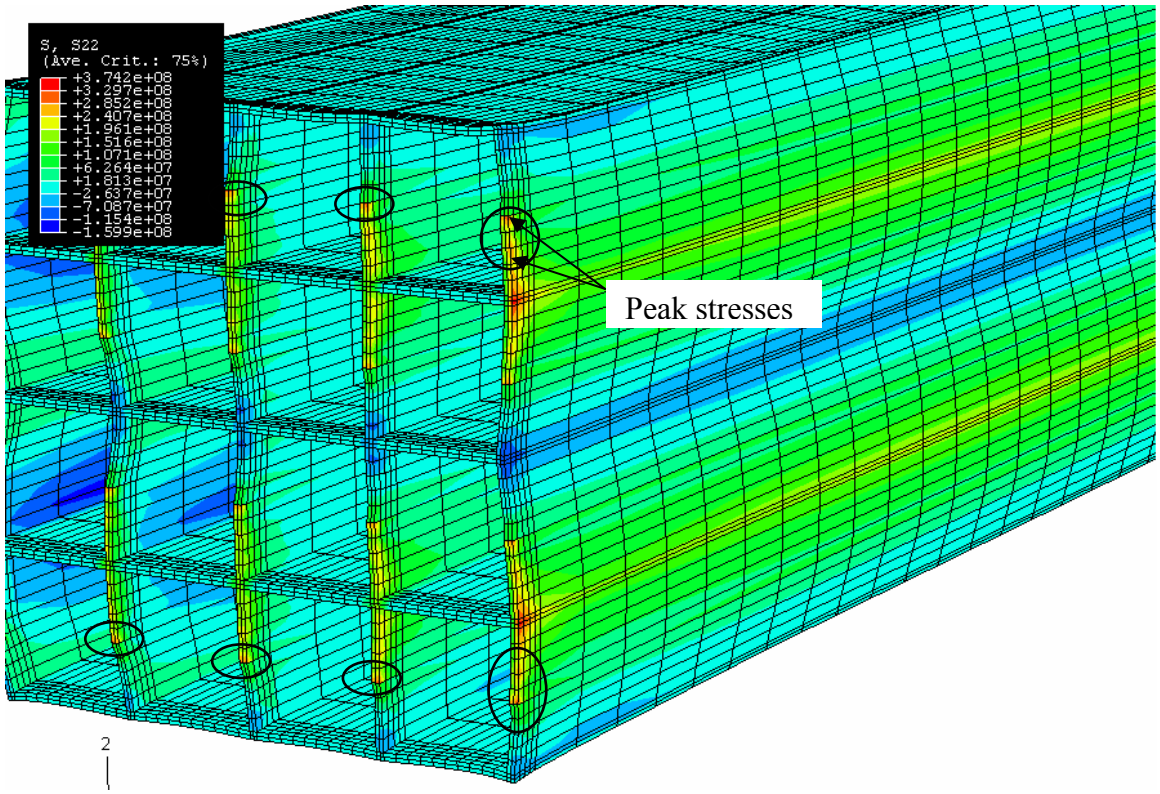

Figure III.24: During cool down, the maximum stress component is the peeling stress (tensile), and it occurs at two spots in the ceramic at around 400K.

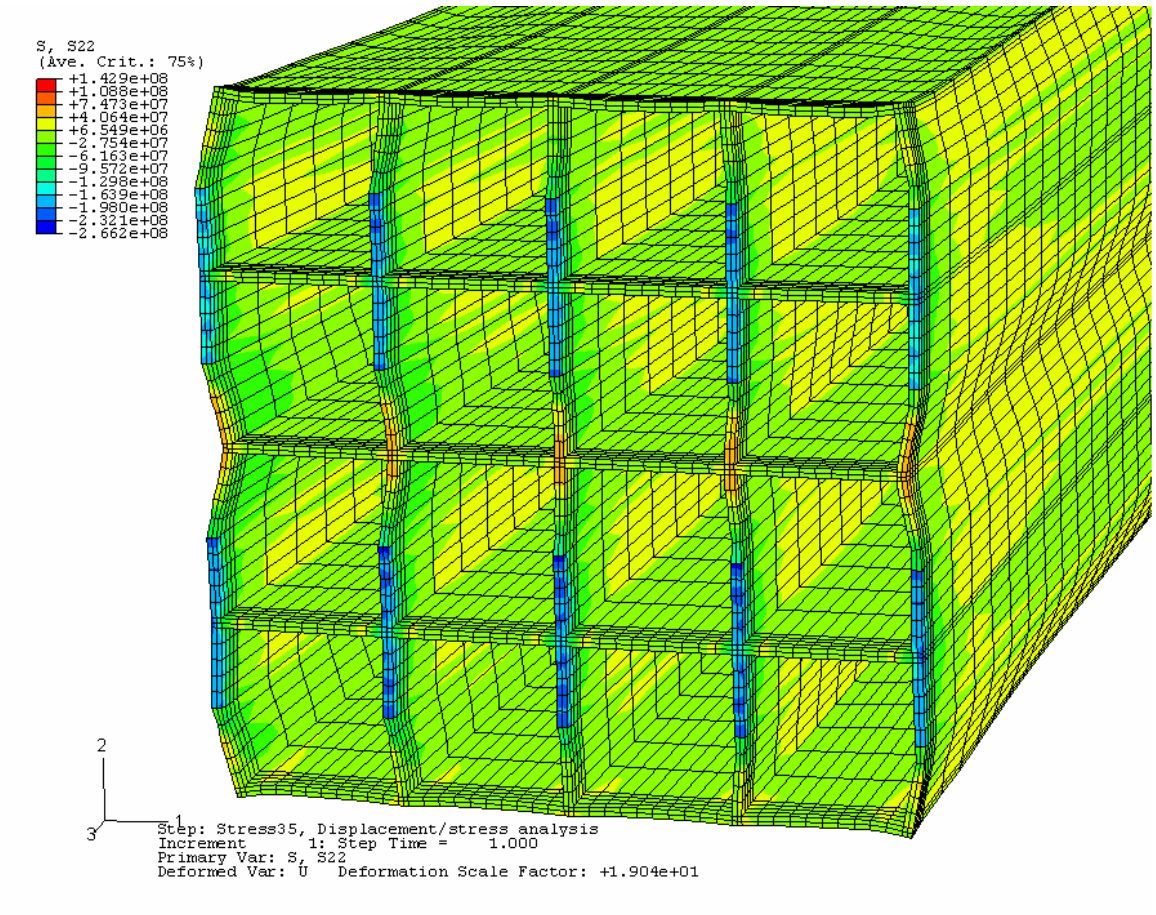

Figure III.25: At steady state operating temperature, the ceramic is put in compression due to the plastic deformation of the metal.

III.3.4. Line graphs of stresses

A line graph shows the path of stress including cool down and transient start-up. Again, one particular node is evaluated for simplicity. The node chosen is on the joint of the ceramic and metal as shown in Figure III.26.

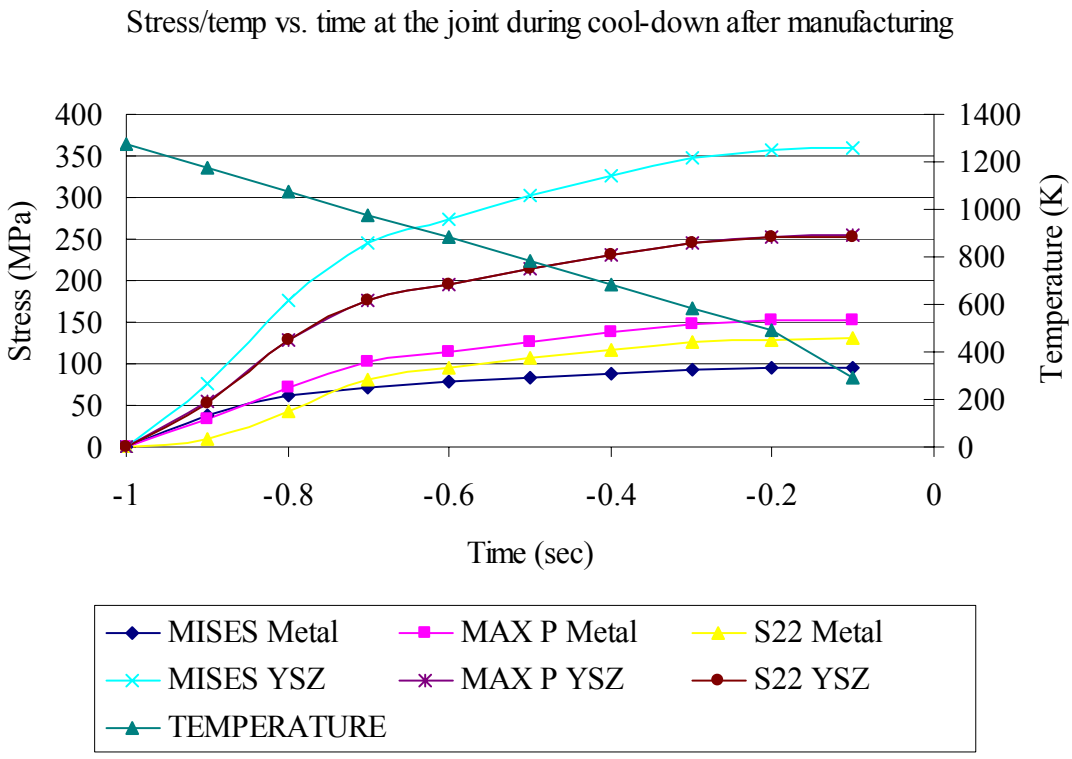

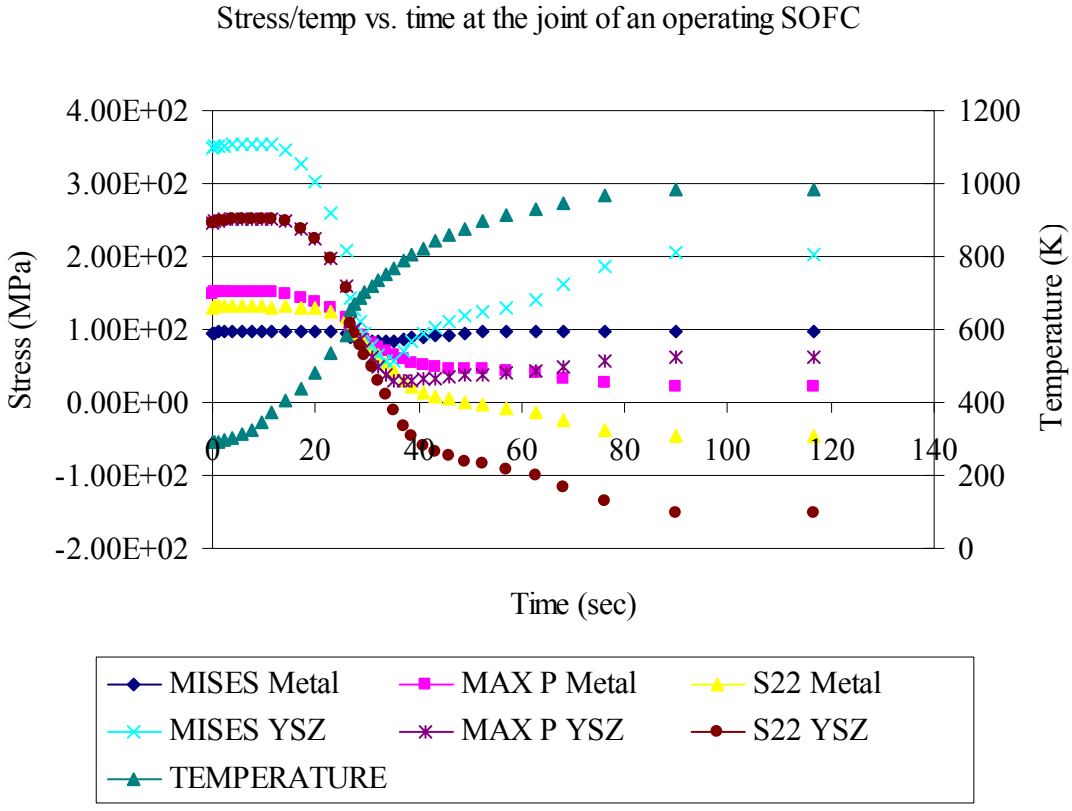

Figure III.26: Stress results during operation of hybrid SOFC at the joint of the ceramic and metal, evaluated at the integration point (0.0577mm from joint).

III.4. Example with no CTE mismatch

One of the focuses of manufacturing is to eliminate CTE mismatch by customizing the metal expansion. However, even under these ideal conditions, the temperature gradients during start-up cause a build up of stresses. The same conditions were used from earlier analysis with the exception that the metal CTE was set equal to the ceramic. The results at the joint edge are shown in Figure III.27.

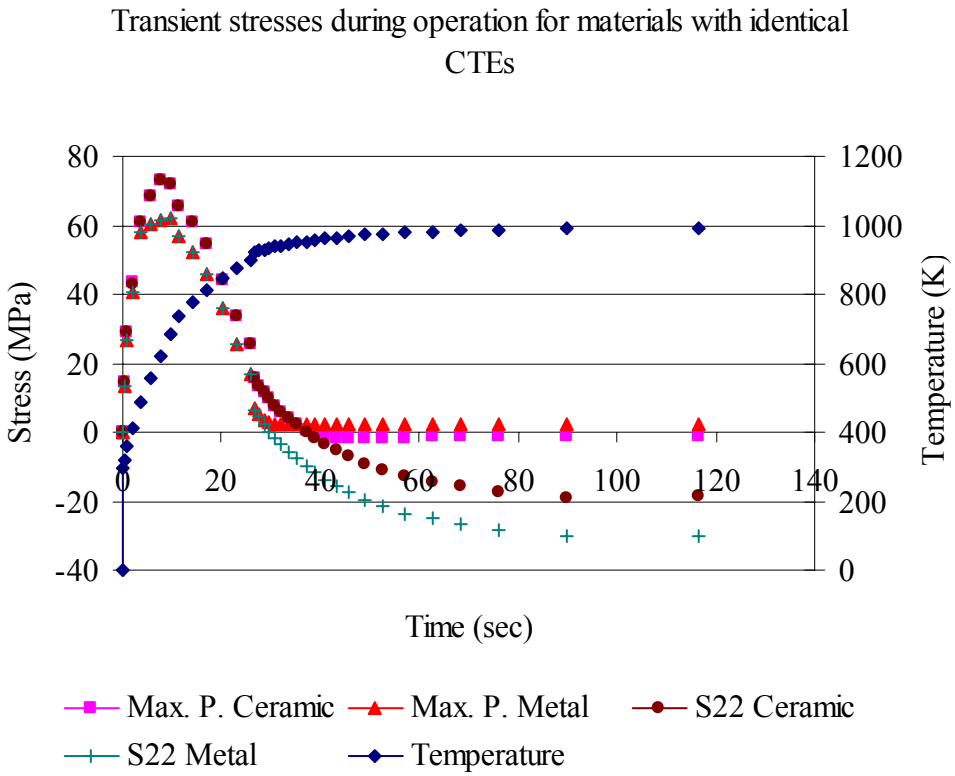

Figure III.27: Stress in the joint at the air inlet occur even if the metal and ceramic have the same CTE (using reduced integration elements).

The most severe stresses occur during the rapid heating by the inlet air. Gradual heating may be used to mitigate these stresses, instead of an instantaneous injection of 980K air.

III.5. Thermal shock considerations

During the operation of the fuel cell, rapid start-up and shut-down may be necessary. Rapid temperature change leads to a large temperature difference between the surface of a material and the mean body temperature. If the surface is much cooler than the body, the surface is in a state of tension. For rapid heating, the surface is in a state of compression. Since tension leads to crack growth, and heating to crack closure, rapid cooling is more severe than heating (Du et al., 2003). Thermal shock is most important in the ceramic for three reasons. First, the ceramic is brittle, and, therefore, more likely to undergo catastrophic failure as cracks on the surface expand. Secondly, the exothermic chemical reaction, providing the majority of the heating in the structure, originates within the ceramic. The largest temperature gradients on rapid start up will be found in the electrolyte. Finally, YSZ has a low resistance to thermal shock. The low resistance to thermal shock is a direct result of the relatively large CTE of YSZ. The thermal stress resistance parameter of a brittle solid is given by Hasselman as (Hasselman, 1970):

$$R = \frac{\sigma_t (1-\nu)}{\alpha E} \tag{III.1}$$

Where σ_t is the tensile strength, υ is Poisson's ratio, E is Young's modulus, and is the α coefficient of thermal expansion. Equation (III.1) was formulated for triaxially strained boundary conditions, the worst possible condition. The R value measures the maximum difference between the surface temperature and the core temperature before the initiation of small cracks. However, the relative strength of different materials may be judged by the resistance parameter. Table III.2 shows the resistance parameters calculated for a

range of ceramics (Lee and Rainforth, 1994). YSZ was calculated and added to compare with reported values for common ceramics.

Table III.2: The resistance to thermal shock was calculated by Equation 8 for YSZ and compared to reported formula results for a number of ceramics in Lee and Rainforth (1994).

Ceramic	YSZ	Al_2O_3	SiC	RBSN	HPSN	LAS
Strength (MPa)	146	344.5	413.4	310	689	137.8
Poisson's ratio	0.313	0.22	0.17	0.24	0.27	0.27
CTE ($x10^{-6}$ °C^{-1})	11.5	7.4	3.8	2.4	2.5	-0.3
E (GPa)	157	379	400	172	310	69
R (°C)	56	96	226	571	649	4860

YSZ is lower than all of the ceramics listed in Table III.2. YSZ has an R value of about 56°C. Hasselman also sites a formula for the maximum rate of change of surface temperature until fracture for a flat plate (1970)

$$\left(\dot{T}\right)_{\max} = \frac{3\sigma_t(1-\nu)d}{\alpha E b^2} \tag{III.2}$$

Where all the variables are the same as in Equation (III.1), with the addition of b, the thickness of the plate and d, the thermal diffusivity of the ceramic. Since the thickness of the wall is 120μm, the resulting allowable rate of surface cooling is in excess of 6000°C/s. Over a similar operating range, Du suggests designing for a 250-500°C/min thermal shock (Du et al., 2003). The resistance of the hybrid SOFC electrolyte structure is well within this limit. However, the result does have a large range of error because of the large dependence of material properties on manufacturing conditions and the likely possibility of large surface defects with the current processing technique. Equations

(III.1) and (III.2) are for stable or quasi-stable fracture. Together, they determine the resistance of a brittle ceramic to crack initiation. In the presence of a defect or great porosity, the resistance to crack growth is the critical factor (Lee and Rainforth, 1994).

Simple experimentation has also been performed to determine the potential for failure under thermal shock (Du et al., 2003). Du heated rods (2mm dia. and 25mm length) and tubes (3mm OD, 25mm length and .3 mm thickness) to 800°C and then cooled them to room temperature by quenching in water and by quenching in air. No sample failed after 20 air cooling cycles. All of the tubes failed after one water quench cycle. The rods, with a single exception, failed after 10 cycles. The testing confirmed the excellent thermal shock resistance of YSZ. The report only mentioned "visible" inspection for crack initiation. Therefore, the initiation of small cracks and crack growth may not be differentiated in the data presented. With the specimen dimensions and average values of YSZ property data from the literature, Equation (III.2) predicts about an 850°C/s temperature change before the initiation of cracks. The quenching temperature of 800°C would most likely cause a lower cooling rate than 850°C/s, but fracture would still be a concern based on the results of Equation (III.2).

CHAPTER IV

CONCLUSIONS

IV.1. Summary of model

This work developed a finite difference code able to perform preliminary design calculations for the thermal-stress analysis of rectangular-celled hybrid solid oxide fuel cells. The ultimate goal of this preliminary design technique is to optimize the cell structure in terms of operating efficiency and structural integrity by running many approximate simulations to narrow the design space. When analyzing a final set of designs, more computationally expensive commercial CFD and FEM codes may be used to analyze the structure in more detail. The finite difference code was originally developed for steady-state thermal analysis of rectangular-celled LCA Copper heat sinks (Dempsey, 2002). For use with LCA-based hybrid SOFC's, the code was significantly modeled to include material changes (hybrid structure), new heat sources (fuel cell electro-chemistry), counter flow conditions, and different fluid properties (air at high temperature and hydrogen). Finally, a transient analysis technique was developed using a time marching scheme to analyze the temperature field during start-up. The finite difference solution was verified by LU decomposition and convergence analyses with respect to time steps and mesh density. Numerically, with the error terms set sufficiently low, the results were found to be very accurate. However, numerical validation does not indicate if the formulation and assumptions of the finite difference code are valid. In the absence of a functioning hybrid SOFC, FLUENT was used as a standard for comparison. The finite difference code compared well with FLUENT.

The thermal analysis results and input geometry are used to write a custom ABAQUS input file for a sequentially coupled stress analysis. Results from a variety of element types and mesh sizes show a full integration 8-node, linear, brick element is adequate for modeling the honeycomb structure. Significant error was found when using the time-saving reduced integration elements. The effects of plastic-strain hardening were included in the metal. An example case, 3cm long, 4x4, hybrid SOFC operating around 1000K composed of a YSZ electrolyte and an $Fe_{39}Ni_8Cr$ interconnect was analyzed in this work. The representative 3cm SOFC was used to characterize the general stress field for the constrained hybrid honeycomb structure as well as to determine regions of elevated stress during startup. Further analysis with variations in input parameters will be similar to this case.

After manufacturing, as the structure is cooled from relaxation temperature, residual stress builds due to the CTE mismatch between the metal and ceramic components. The 3 cm hybrid SOFC had significant edge effects, stress concentrations at the edge of the honeycomb, caused by the elevated peeling stress at the free ends. A stress singularity was measured at the sharp corner where the ceramic component is bound to the metal. The location of the stress singularity corresponds to crack initiation sites in experimental specimens. During start-up, the structure is heated, leading to a measurable increase in stress due to the high temperature gradient but eventually relieving stress as the relaxation temperature is approached. Most of the structure remains below the failure stress of YSZ, but the edge effects are substantial enough to lead to failure in the model. In particular, the stress singularity at the edge of the joint is a possible site of failure in the brittle ceramic.

IV.2. Related research

A considerable amount of research is ongoing at Georgia Tech with implications for thermal-stress analysis of hybrid SOFC's. The electro-chemical performance model by Dempsey (Dempsey, pers. com., 2004) may be refined in the future to reflect different electrolyte materials or more complex heat generation, dependent on a non-constant concentration of reactants. Any changes in the performance model can be easily changed in the electro-chemical subroutine in the finite difference code. Eisele (Eisele, 2004) has developed a model to characterize the stresses arising from the constrained densification of the components of the hybrid SOFC. The analysis in the present work assumed a relaxation temperature related to the initiation of creep in the ceramic and viscous behavior in the metal. Eisele considers plastic and elastic strain through the entire densification process. The relaxation temperature and, in turn, the residual stress would be a natural condition of the sintering and reduction model. In the future, the sintering and reduction model could be coupled with the thermal-stress model developed in this work for a more accurate determination of stresses during operation.

IV.3. Future consideration of heat transfer by radiation

At elevated temperatures, radiation may influence the temperature distribution in the hybrid SOFC. Even in a vacuum, two materials with different initial temperatures will eventually reach equilibrium due to the radiation emitted from the surfaces of the materials. Since large thermal gradients are detrimental to the SOFC structural integrity, radiation may mitigate steady state operating stresses by reducing temperature gradients. Thermal radiation is proportional to the temperature difference between the emitting and

absorbing surfaces, the emissivity of the surfaces, distance between the surfaces, radiation direction, and the surface area. These factors can all be accounted for by variables in the finite difference scheme. Radiation was successfully implemented in the finite difference scheme of Yakabe (2001). For similar operating conditions and materials, Yakabe (2001) assumes the channel walls are gray surfaces, greatly simplifying the radiation problem. Since the outer surfaces are insulated, only the inside channel walls radiate. Each small area, dA_i, has an infinite number of radiation vectors emitted in all possible directions, eventually being absorbed by an opposing wall. One such vector is shown in Figure IV.1.

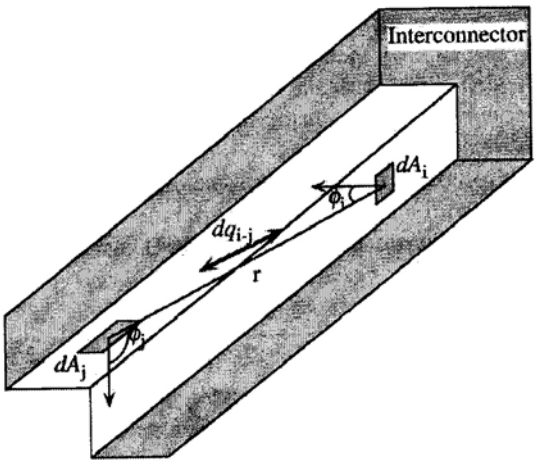

Figure IV.1: Radiation emitted from one wall continues on a random vector until it is intercepted by an opposing wall (Yakabe et al., 2001).

Considering gray surface radiation, the radiation transfer, dq_{i-j}, is related as (Yakabe et al., 2001)

$$dq_{i-j} = \cos\phi_i \cos\phi_j \frac{dA_i dA_j}{\pi r^2} \varepsilon_i \varepsilon_j \left(E_i - E_j\right) \qquad \text{(IV.1)}$$

where r is the distance between surfaces, ε_i and ε_j are the emissivity of the surfaces, E_i and E_j are the radiation energies, dA_i and dA_j are the surface areas and ϕ_i and ϕ_j are the angles between the ray and the normal surface vector. Radiation energy is found by the Stefan-Boltzmann law (Yakabe et al., 2001),

$$E = \sigma T^4 \tag{IV.2}$$

where σ is the Stefan-Boltzmann constant.

To implement Equation (IV.1), small, finite surface regions on the interior of the channel must be defined. Also, an array of radiation directions must be determined sufficient to approximate the effects of an infinite number of radiation directions. Radiation has been implemented by Dempsey (pers. com., 2004) using FLUENT. If implemented in the finite difference code, the radiation results can be compared to FLUENT. However, the solution time will increase with the addition of radiation. Yakabe (2001) recorded a ten fold increase in computational time when radiation was included. For this reason, only one small simulation was modeled with radiation by Yakabe to indicate the effect at temperatures of 900-1000°C. Further significant modifications should be made to the formulation of Yakabe (2001) to account for optically thin cell walls. With optically thin walls, radiation from one wall will penetrate surrounding walls to affect non-neighboring cells. Optically thin materials have an optical thickness of less than 1. The optical thickness, proportional to the wall thickness and absorption coefficient (Modest, 2003) is less than one for the hybrid SOFC. A finite difference radiation model may be implemented as part of future work pertaining to hybrid SOFC thermal stress analysis.

IV.4. Parametric modeling of the hybrid SOFC

The finite difference code is a preliminary design tool. Optimization routines could be used to narrow the large range of SOFC designs to provide the maximum power output or minimum stress, etc… However, the design is restricted by two main requirements. First, the structure must produce power. To produce power, according to the formulation of Dempsey (pers. com., 2004), a minimum temperature must be maintained. The minimum temperature for the reaction to occur, 910K, places restrictions on how low the inlet temperature of the fluids can be. If the fast-flowing air is too cold, the reaction ceases. On the other hand, the design requirements of the hybrid SOFC call for low operating temperatures. Sustained temperatures too far above 1000K are not desired. Unless the electrical properties measured by Dempsey (pers. com., 2004) are improved, the operating range is extremely restrictive on design. A second restriction occurs because of the solution time required for transient stress analysis in ABAQUS. The finite difference code usually runs in less than 10 minutes. By contrast, ABAQUS may take between one to ten hours to run a transient simulation. The performance is contingent on the number of time steps and the size of the model. Running a large number of ABAQUS models as part of an optimization routine may be computationally expensive.

REFERENCES

Atkinson, A. and A. Selcuk (2000). "Mechanical Behavior of Ceramic Oxygen Ion-Conducting Membranes." Solid State Ionics **134**: 59-66.

Cai, P. Z., D. J. Green, et al. (1997a). "Constrained Densification of Alumina/Zirconia Hybrid Laminates, I: Experimental Observations of Processing Defects." Journal of the American Ceramic Society **80**(8): 1920-1939.

Cai, P. Z., D. J. Green, et al. (1997b). "Constrained Densification of Alumina/Zirconia Hybrid Laminates, II: Viscoelastic Stress Computation." Journal of the American Ceramic Society **80**(8): 1940-1948.

Chapra, S. C. and R. P. Canale (1998). Numerical Methods for Engineers, 3rd ed., Boston, McGraw-Hill.

Chiu, C.-C. and Y. Liou (1994). "Residual stresses and stress-induced cracks in coated components." Thin Solid Films(268): 91-97.

Croft, D. R. and D. G. Lilley (1977). Heat Transfer Calculations Using Finite Difference Equations, London, Applied Science Publishers.

Dempsey, B. (2002). Thermal Properties of Linear Cellular Alloys. Master's thesis, Department of Mechanical Engineering, Georgia Institute of Technology, Atlanta.

Dempsey, B. (2004). Unpublished report on the development of an electrochemical model for the Georgia Tech hybrid SOFC to J. LeMasters. Atlanta.

Du, Y., N. M. Sammes, et al. (2003). "Extruded Tubular Strontium and Magnesium-Doped Lanthanum Gallate, Gadolinium-Doped Ceria, and Yttria-Stabilized Zironia Electrolytes: Mechanical and Thermal Properties." Journal of the Electrochemical Society **150**(1): A74-A78.

Eisele, S. (2004). Characterization of Material Behavior During the Manufacturing Process of a Co-Extruded Solid Oxide Fuel Cell. Master's thesis, Department of Mechanical Engineering, Georgia Institute of Technology, Atlanta.

Faires, J. D. and R. L. Burden (1998). Numerical methods, 2nd ed., Pacific Grove, CA, Brooks/Cole Pub. Co.

Hagos, S. T. and R. P. Travis (2003). Issues Affecting the Mechanical Integrity of SOFCs. Paper presented at the Eighth International Symposium on Solid Oxide Fuel Cells, Electrochemical Society.

Hasselman, D. P. H. (1970). "Thermal stress resistance paramters for brittle refractory ceramics: a compendium." Ceramic Bulletin **49**(12): 1033-1037.

Hodge, B. K. and R. P. Taylor (1999). Analysis and Design of Energy Systems, 3rd ed., Upper Saddle River, N.J., Prentice Hall.

Incropera, F. P. and D. P. Dewitt (1996). Fundamentals of Heat and Mass Transfer, 4th ed., New York, Wiley.

Keegan, K., M. Khaleel, et al. (2002). Analysis of a Planar Solid Oxide Fuel Cell Based Automotive Auxiliary Power Unit. SAE 2002 World Congress, Detroit, Michigan.

Lambropoulos, J. C. and S. M. Wan (1989). "Stress Concentration Along Interfaces of Elastic-Plastic Thin Films." Materials Science and Engineering(A107): 169-175.

Lee, W. E. and W. M. Rainforth (1994). Ceramic Microstructures, 1st ed., London, Chapman & Hall.

Meurant, G. (1999). Computer Solutions of Large Linear Systems, 1st ed., Amsterdam, Elsevier Science.

Minh, N. Q. and T. Takahashi (1995). Science and Technology of Ceramic Fuel Cells, Netherlands, Elsevier Science.

Modest, M. F. (2003). Radiative Heat Transfer, 2nd ed., Amsterdam, Academic Press.

Selcuk, A., G. Merere, et al. (2001). "The influence of electrodes on the strength of planar zirconia solid oxide fuel cells." Journal of Material Science(36): 1173-1182.

Singhal, S. C. (2000). "Science and Technology of Solid-Oxide Fuel Cells." MRS Bulletin **25(**3): 16-21.

Sudaprasert, K., R. P. Travis, et al. (2003). A Computational Fluid Dynamics Model of a SOFC. Paper presented at the Eighth International Symposium on Solid Oxide Fuel Cells, Electrochemical Society.

Tojo, T., T. Atake, et al. (1999). "Excess Heat Capacity in Yttria Stabilized Zirconia." Journal of Thermal Calorimetry **57**: 447-458.

Yakabe, H., T. Ogiwara, et al. (2001). "3-D model calculation for planar SOFC." Journal of Power Sources **102**: 144-154.